

# Ultrafast Dynamics of ZnO Films Using Femtosecond Pump Probe Spectroscopy

## Dissertation

zur Erlangung des akademischen Grades  
doktor rerum naturalium (Dr. rer. nat.)

vorgelegt der

Naturwissenschaftlichen Fakultät II  
der Martin-Luther-Universität Halle-Wittenberg



von

Sumedha Chouthé

geb. am 24. September 1982 in Bhopal, Indien

**Gutachter:** 1. Prof. Dr. Heinrich Graener

2. Prof. Dr. Marius Grundmann

3. Prof. Dr. Jürgen Christen

**Verteidigt am: 12<sup>th</sup> April 2010**



*To my parents and sister ...*



# Table of contents

<b>CHAPTER 1. INTRODUCTION AND AIM</b> .....	<b>1</b>
1.1 ORGANISATION OF THESIS.....	2
<b>CHAPTER 2. EXPERIMENTAL TECHNIQUES</b> .....	<b>5</b>
2.1 TIME RESOLVED PUMP-PROBE SPECTROSCOPY .....	5
2.1.1 Principle of pump-probe spectroscopy.....	5
2.2 FEMTOSECOND WHITE LIGHT TRANSMISSION SPECTROSCOPY .....	6
2.2.1 Femtosecond pulsed versus continuous excitation .....	7
2.2.1.1 Ultrashort pulses .....	7
2.2.2 Single wavelength versus white light probe.....	8
2.2.2.1 Supercontinuum generation of white light.....	9
2.3 EXPERIMENTAL DETAILS .....	10
2.3.1 Experimental set up .....	11
2.3.2 Data acquisition.....	14
2.3.3 Accuracy of pump-probe experiments .....	16
2.3.4 Processing of time resolved data .....	17
2.3.4.1 Zero-time and chirp correction .....	17
2.3.4.2 Correction for scattering .....	18
2.3.5 Example of time resolved data.....	18
2.4 DETERMINATION OF OPTICAL PROPERTIES OF ZNO FILMS .....	19
<b>CHAPTER 3. SAMPLE ANALYSIS</b> .....	<b>21</b>
3.1 BASICS OF SEMICONDUCTORS .....	21
3.1.1 Bandstructure and optical properties of semiconductors.....	21
3.1.2 Doping and defects in semiconductors .....	24
3.2 PHYSICAL PROPERTIES OF ZINC OXIDE.....	24
3.2.1 Bandstructure of ZnO .....	24
3.2.2 Doping and defects in ZnO .....	25
3.3 ZNO SAMPLES UNDER INVESTIGATION .....	26
3.3.1 Sample preparation by pulsed laser deposition.....	26
3.3.2 Thermal admittance spectroscopy measurements .....	27
3.4 OPTICAL PROPERTIES OF ZNO SAMPLES .....	27
3.4.1 Ellipsometric analysis of ZnO films.....	27
3.4.1.1 Dielectric functions for different ZnO samples .....	30
3.4.2 Transmission measurements of ZnO films.....	31
3.4.2.1 Transmission spectra of ZnO films.....	31
3.4.2.2 Simulation of transmission spectrum of ZnO .....	32
3.4.3 Microscope images of ZnO films .....	34
3.4.4 Atomic force microscopy on ZnO films.....	35
<b>CHAPTER 4. DISENTANGLEMENT OF CONTRIBUTIONS IN THE TIME RESOLVED SPECTRA OF ZNO FILMS</b> .....	<b>37</b>
4.1 MODEL.....	37
4.1.1 Implementation of Levenberg Marquardt optimization routine .....	39
4.2 IMPLICATIONS OF DIFFERENT DIELECTRIC COMPONENTS ON SIMULATED DIFFERENCE OPTICAL DENSITY SPECTRUM .....	40
4.2.1 Exciton bleaching .....	40

4.2.2 Modulations.....	41
4.2.3 Bandgap variation.....	43
4.3 CONFIDENCE TESTS OF THE OPTIMIZATION ROUTINE .....	43
4.4 SIMULATION OF TIME RESOLVED SPECTRA: ILLUSTRATIONS.....	44
<b>CHAPTER 5. TIME RESOLVED DYNAMICS IN ZNO FILMS.....</b>	<b>47</b>
5.1 INTRODUCTION .....	47
5.2 TIME RESOLVED RESULTS OF ZNO FILMS.....	49
5.2.1 <i>Experimental results</i> .....	49
5.2.1.1 Spectral variation.....	49
5.2.1.2 Temporal evolution .....	50
5.2.2 <i>Results of modelling: Ultrafast carrier dynamics in ZnO films</i> .....	50
5.2.2.1 Interpretation of the modelled time resolved data.....	52
5.2.2.2 Carrier excitation.....	54
5.2.2.3 Bleaching of discrete exciton .....	55
5.2.2.4 Stimulated emission .....	57
5.2.2.5 Interference contribution .....	59
5.2.2.6 Transmission increase at 400nm .....	61
5.2.3 <i>Effect of temperature</i> .....	62
5.3 CARRIER DYNAMICS IN ZNO FOR DIFFERENT PUMP WAVELENGTHS.....	65
5.3.1 <i>Experimental results</i> .....	65
5.3.2 <i>Carrier excitation for different excitation wavelengths</i> .....	66
5.3.3 <i>Indirect and direct formation of excitons</i> .....	67
5.3.4 <i>Bleaching at different excitation wavelengths</i> .....	69
5.4 INTENSITY DEPENDENCE OF TIME RESOLVED DYNAMICS IN ZNO.....	71
5.4.1 <i>Linear nature of carrier excitation</i> .....	71
5.4.2 <i>Excitation energy dependence of exciton bleaching</i> .....	72
5.4.3 <i>Non-linear nature of stimulated emission</i> .....	73
5.4.4 <i>Excitation energy dependence of interference contributions</i> .....	75
5.4.5 <i>Bleaching at fundamental wavelength for different pump energies</i> .....	75
5.4.6 <i>Pump energy dependence of other ZnO films</i> .....	76
5.5 COMPARISON OF CARRIER DYNAMICS IN DIFFERENT ZNO FILMS .....	78
5.5.1 <i>Thickness dependence of interferometric modulations</i> .....	79
5.5.2 <i>Thickness dependence of stimulated emission</i> .....	80
5.5.3 <i>Differences in other contributions for different ZnO films</i> .....	81
5.5.3.1 Carrier excitation.....	81
5.5.3.2 Transmission increase at 400nm .....	82
5.5.3.3 Exciton bleaching in different ZnO samples.....	83
5.5.3.4 Absorption increase at 380nm.....	84
<b>SUMMARY AND OUTLOOK .....</b>	<b>87</b>
<b>APPENDIX A .....</b>	<b>91</b>
<b>ACKNOWLEDGEMENTS.....</b>	<b>93</b>
<b>ERKLÄRUNG .....</b>	<b>95</b>
<b>CURRICULUM VITAE.....</b>	<b>97</b>
<b>REFERENCES.....</b>	<b>99</b>

## Chapter 1. Introduction and aim

Zinc oxide (ZnO) is an important wide bandgap semiconductor with a wide variety of applications in piezoelectric transducers, varistors, phosphors and transparent conducting films [1,2]. It is a group II-VI direct bandgap n-type semiconductor with a large energy gap of  $\sim 3.4\text{eV}$  at room temperature. It has wurtzite crystal structure, is transparent in the visible region and electrically conductive. These outstanding properties make it a promising semiconductor for potential technological applications such as ultraviolet light emitting devices and semiconductor electronics [3]. Among the several advantages over other competitive materials such as GaN regarding this application, ZnO has a large free exciton binding energy of around  $60\text{meV}$  compared to  $24\text{meV}$  in GaN, hence the excitonic emission processes can efficiently persist at room temperature and higher. Stimulated emission and lasing properties of highly excited ZnO have been reported in the literature [4,5,3]. The keen interest in ZnO for the realization of ZnO based optoelectronic devices has also been fuelled by the significant development of growth technologies for the fabrication of single crystalline bulk material, polycrystalline ZnO to epitaxial layers and nanowires. Doping ZnO to produce n-type semiconductor is relatively easy to achieve with elements such as Al and Ga. On the other hand, there have been fewer reports about the p-type doping of ZnO using Li and Na [6,7]. Reliable p-type doping is still an area of intense research. Other salient properties of ZnO include its broad chemistry leading to many possibilities for wet chemical etching, low power threshold for optical pumping, radiation hardness and biocompatibility. Together all these properties of ZnO make it an ideal candidate for a variety of devices ranging from sensors to ultraviolet laser diodes and nanotechnology-based devices such as displays [8].

This investigation is a part of the joint project SFB 762 “Functionality of oxidic interfaces” devoted to the preparation and characterization of multifunctional oxidic heterostructures consisting of components with ferroelectric, magnetic, semiconducting, and insulating properties to pave the way for technologically better performing materials. Zinc oxide with its aforementioned properties is an ideal candidate for use as interface with ferroelectric materials such as barium titanate in the multifunctional oxidic heterostructures and to study their properties. However, prior to its application as an interface, first it is critical to gain fundamental understanding of the electronic properties of ZnO alone without any interface, since it is the properties of a material that eventually determine its usefulness in an application. This laid the foundation for pursuing the reported work.

Considerable research has been carried out on the optical properties of ZnO using pump probe transient absorption spectroscopy, luminescence spectroscopy, up-conversion technique, transient grating spectroscopy and optical Kerr gate luminescence spectroscopy [9,10,11,12,13]. Reported studies on its ultrafast dynamics are explained in terms of free charge carrier trapping into localised states which occur on a time scale of  $\sim 1$ ps. Initially delocalised charge carriers can get trapped into shallow or deep trapped states within the bandgap [14,15,16]. However, little has been reported about the complete ultrafast dynamics of undoped ZnO films over the entire visible spectrum. There is still a lack of general consensus regarding the mechanisms underlying photoexcitation and relaxation in ZnO. The exact role of intrinsic and extrinsic defects in the optical properties of this material is still a matter of speculation. Determination of these aspects is of utmost significance to gain a better fundamental understanding of the charge carrier dynamics of the ZnO films.

This thesis is aimed at investigating the relaxation processes of charge carriers in ZnO films and to utilize this knowledge to eventually refine the dielectric function of ZnO. It also aims to study surface effects on the carrier dynamics in ZnO. The ultrafast dynamics of pure ZnO films is intensively investigated by femtosecond time resolved pump probe spectroscopy. The intention is to improve the dielectric function of ZnO by employing time resolved pump probe spectroscopy in conjunction with ellipsometry. This project is collaborated with the semiconductor physics group in the University of Leipzig, who has provided the ZnO films used in this investigation and have performed ellipsometry and thermal admittance spectroscopy (TAS) on them. The system being studied is nominally undoped ZnO film on sapphire as substrate. The thickness of ZnO layer in different samples ranged between 98nm to 476nm and the thickness of sapphire substrate was  $\sim 200\mu\text{m}$ . Upon excitation with an intense femtosecond laser pulse at 400nm, the change in optical density induced by the excitation pulse is probed across the entire visible region by using supercontinuum femtosecond pulse as probe at variable time delays between the pump and probe pulses.

The time resolved spectroscopy employed to investigate the electronic properties of transient states in ZnO is associated with incoherent processes. Optical properties of the materials depend on the occupancy of the electronic states since the electrons are able to absorb photons only if empty upper states are available. By exciting electrons with a laser pulse, the occupancy of the electronic states is changed and hence its optical properties. The excited electrons may relax or get further excited, thereby altering the transmission from the sample. This change in transmission was measured in the ultrafast pump-supercontinuum probe spectroscopy on ZnO films. Since ZnO is transparent over the entire visible range, transmission is the most fitting choice of property for this investigation.

## 1.1 Organisation of thesis

The thesis is organized as follows: Chapter 2 “Experimental techniques” is devoted to the description of experimental details related to pump probe spectroscopy employed in the presented work. It begins with a description of the fundamental principle of time resolved spectroscopy. Next, the basic theory of ultrashort pulses is introduced, with an emphasis on their outstanding features for use in time resolved spectroscopy. The supercontinuum generation of white light used as the probe pulse in the time resolved measurements is described as well, highlighting the salient features of



utilizing white light as probe instead of a single wavelength. Next, the experimental set up employed in the current investigation is discussed in detailed. Particular attention is laid on the various intricate aspects of the experiment such as characterization of pump and probe pulses, their triggering scheme in the measurement, processing and acquisition of time resolved data, accuracy of the measurements etc. The chapter ends with a brief description of the principle of ellipsometry, specifications of transmission spectrometer, AFM, microscope and TAS set-up that were employed to characterize the ZnO films.

Chapter 3 “Sample analysis” is devoted to the description of properties of ZnO semiconductor films and their characterization. Basics of semiconductors including its bandstructure, relevant physical and optical properties are briefly revised at the beginning of the chapter. The next section brings into focus all the known relevant properties of ZnO, doping, sample preparation of the ZnO films under investigation as well as results from the TAS measurements performed on them. The dielectric function of ZnO obtained from ellipsometry is extensively discussed in the following section. The experimental transmission spectra of the ZnO films along with their simulated results obtained using the dielectric function from ellipsometric measurements are discussed in detail. The chapter concludes with the presentation of microscope and AFM images of the surfaces of the investigated ZnO films.

Chapter 4 “Disentanglement of contributions in the time resolved spectra of ZnO films” deals with the simulation of the experimental time resolved spectra. In order to extricate various contributions in the time resolved spectrum of ZnO films, a model has been developed based on its dielectric function. The developed model used in conjunction with Levenberg Marquardt optimization routine is explained in detail. The following section explores various aspects of the simulated pump probe spectra to understand the many facets of the highly complex time resolved data. The correctness and accuracy of the simulations are addressed through various confidence tests. A number of illustrations of the simulated fit to the measured time resolved spectra are presented at the end of the chapter.

Chapter 5 “Time resolved dynamics in ZnO films” documents the results of time resolved spectroscopy performed on the ZnO films. Different processes in its carrier dynamics are identified and interpreted. In an attempt to understand the relaxation mechanisms in ZnO upon ultrafast photoexcitation, the sequence of events in the carrier dynamics is proposed in the band picture of ZnO. The nature of relaxation processes was further investigated by performing pump probe spectroscopy at different excitation wavelengths. The results and the ensuing discussion of these findings are presented as well. Thereafter, the effect of the excitation intensity on the carrier dynamics is extensively studied. In the last section of this chapter, the pump probe results for different ZnO samples are discussed and the film thickness dependence of certain contributions is studied.

A summary of the key results from the femtosecond time resolved spectroscopy presenting a convergent picture of the ultrafast dynamics in ZnO films is presented. The open questions and scope of the future work is briefly discussed as well. References, appendix and acknowledgements are appended at the end of the thesis.



## Chapter 2. Experimental techniques

### 2.1 Time resolved pump-probe spectroscopy

Time resolved spectroscopy encompasses a powerful set of techniques for probing and characterizing electronic and structural properties of transient excited states of materials. By employing flexible and tunable light sources for wide spectral selectivity as well as covering all temporal orders of magnitude, it can be utilized to generate a complete photophysical profile of the material under investigation. The dynamical information of electronic processes, traced by the temporal progression of the excited states, typically ranges from the microsecond to sub-picosecond regime. To investigate the dynamics, the technique can be assembled in various optical configurations spanning a wide range of time-resolutions from millisecond through to femtosecond regime.

Transient spectroscopy, as discussed below, is a pump-probe technique that involves two laser pulses. One pulse causes photo-induced perturbation in the sample and the second investigates the subsequent induced optical changes respectively. There are other techniques that employ more than two pulses, such as photon echoes and four-wave mixing (involving three laser pulses). The interpretation of experimental data from such techniques is usually much more complex than in two pulse ones. Nuclear magnetic resonance and electron spin resonance are often implemented with multiple-pulse techniques, where radio waves and micro waves are used instead of visible light.

#### 2.1.1 Principle of pump-probe spectroscopy

In pump probe spectroscopy, a physical process or a series of processes in the material are stimulated by an intense laser pulse labelled as the pump pulse. It interacts with the sample and excites it into a non-equilibrium state. For efficient initiation of the dynamical processes, a high intensity pump pulse is used. Thenceforth, the system relaxes towards a new equilibrium state. The relaxation processes that consequently follow after the photo-induced excitation in the sample are measured by another laser pulse known as the probe. A low intensity pulse is chosen as the probe so that it itself does not cause any perturbation in the sample. The exact time of arrival of the probe pulse is accurately known and can be suitably varied with respect to the pump.

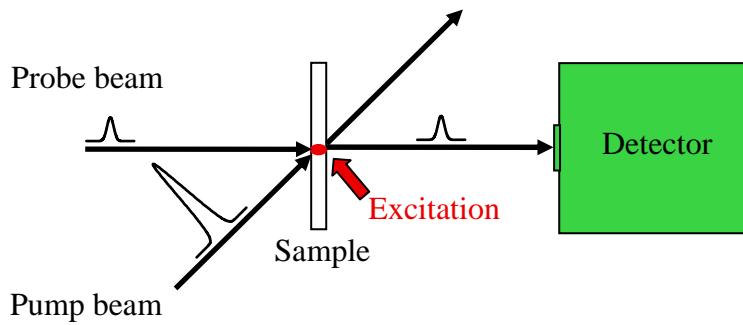


Figure 2.1 Schematic of pump-probe spectroscopy

An optical property related to the probe pulse (transmission, reflectivity, absorption, luminescence, Raman scattering) is monitored for a series of variable time delays between pump and probe pulses to investigate the temporal changes in that property induced by the excitation pulse. Thus, by monitoring the probe signal as a function of the time delay, one can obtain information on the relaxation of the generated excitation and hence the carrier dynamics initiated by the pump. In pump probe spectroscopy, depending of the material's characteristics and the information sought, transient changes of a variety of optical properties related to the probe pulse such as differential transmission, fluorescence, absorption or Raman scattering can be monitored. Each property provides a wide array of information on the sample properties in different spectral domains. Time resolved infrared spectroscopy involves the dynamical study of vibrational states. Time resolved UV-Visible/Absorption spectroscopy deals with dynamics of electronic states of the material. Time resolved fluorescence spectroscopy provides information about the emission of excited states whereas time resolved Raman spectroscopy deals with vibrational states.

## 2.2 Femtosecond white light transmission spectroscopy

In the presented work, femtosecond pump supercontinuum probe transmission spectroscopy is employed to investigate the charge carrier dynamics in ZnO films. Since ZnO is transparent over the entire visible region, transmission is the most fitting choice of property for this investigation. In transient transmission spectroscopy, after excitation by a pump pulse, the changes in the absorption coefficient and refractive index (both derived from the dielectric function) and hence the transmission changes of the sample at a particular wavelength or range of wavelengths of a sample is measured by a weak probe pulse as a function of time [1]. Delay time zero is defined as the time when the peaks of the pump and probe beams overlap in time at the sample surface. Both the pump and probe pulses for measuring the transmission changes are derived from a pulsed laser. For a system at resonance with a femtosecond pulse, at thermal equilibrium, the sample acts as a saturable absorber as all the carriers are in the ground state. After the excitation, the altered dielectric function decays with time according to the rate equation. This technique is valid only for time delays that are sufficiently large so as to avoid coherent effects. The following sub-sections highlight the salient features of femtosecond pulses and probing with broadband supercontinuum light justifying the choice of the technique applied.

## 2.2.1 Femtosecond pulsed versus continuous excitation

Continuous (CW) laser beam, where the excitation is relatively constant with respect to time, is suitable to investigate slow relaxation processes in materials. However, if the process under study is fast, then the desired time resolution can only be achieved by employing a pulsed laser. Pulses with pulse widths of nanoseconds and picoseconds can be utilized to study various electronic and lattice dynamics in systems [2]. However, there are significant basic processes, which are often the primary steps in the carrier dynamics in atoms and molecules that occur faster than what the nano- and picosecond pulses can resolve. In that case, femtosecond pulses can be employed to spectrally tune to the electronic transitions of the material to probe the dynamical processes. Ultrafast spectroscopy deals with the investigation of dynamics of the charge carriers at femtosecond time resolution (1fs= $10^{-15}$ s, about one optical cycle). The advantages of using the ultrashort pulses for time resolved spectroscopy are many fold. If some processes induced by the excitation light are faster than its own time duration, it will not be possible to observe them. Only those processes which are slower than the pulse duration will be observed directly. Some slower processes can be the consequence of faster ones. In this case, it will be difficult to understand and correctly interpret their origin. Femtosecond spectroscopy circumvents this limitation by making it possible to study processes which occur on time scales as short as femtoseconds. Also, fast excitation leads to temporally distinct and clear-cut start of the dynamics. It enables one to probe the dynamics of processes with shortest feasible response times so as to lose as little information as possible and therefore fastest time resolution can be achieved. Additionally, femtosecond pulses being ultrashort have large peak powers even for moderate pulse energies, which is ideal for studying the nonlinear processes while remaining below the damage threshold energy. The next section provides a brief introduction to the basic physics of ultrashort pulses.

### 2.2.1.1 Ultrashort pulses

An ultrashort pulse of light is an electromagnetic pulse whose pulse duration is less than  $10^{-9}$  s. The femtosecond pulses being very short have a broad spectral width. Owing to the concentration of energy in an extremely short time interval of upto  $10^{-15}$ s, they are characterized by high peak intensity that usually leads to nonlinear interactions in various medium. The peak pulse power is extremely large even at moderate pulse energies [3,4]. They are usually generated with mode-locked lasers, but sometimes also with optical parametric amplifiers (possibly using a supercontinuum as input) or with free electron lasers [5]. The mode-locked femtosecond pulse is made up of superposition of many electromagnetic waves, has a constant phase relation and is transform limited.

The electromagnetic waves are completely described by the space and time dependent electric field. The real part of the complex electric field of an ultrashort pulse oscillates at a mean angular frequency  $\omega_0$  corresponding to the central wavelength of the pulse [6,7]. The complex field is usually represented by the product of an amplitude  $I(t)$ , a phase term and a phase function  $\psi(t)$  as in equation (2.1).

$$E(t) = \sqrt{I(t)}e^{i\omega_0 t} e^{i\psi(t)} \quad (2.1)$$

$$E(\omega) = F(E(t)) = \sqrt{S(\omega)}e^{i\phi(\omega)} \quad (2.2)$$

The expression of the complex electric field in the frequency domain can be obtained from the Fourier transform of  $E(t)$ . Figure 2.2 depicts the temporal profile of an ultrashort pulse. Like in the time domain, the pulse can be characterized by intensity and a phase function in the frequency domain as well, as shown in expression (2.2). Because of the presence of the term,  $E(\omega)$  is centered around  $\omega_0$ ,  $E(\omega - \omega_0)$  is generally

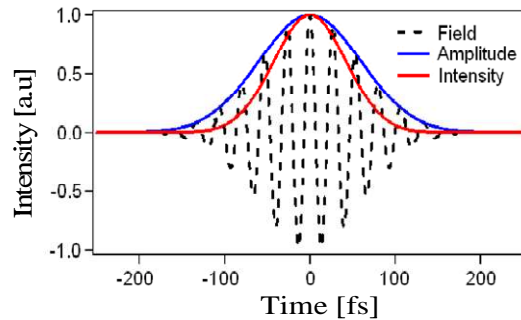


Figure 2.2 Temporal profile of an ultrashort pulse

approximated by  $E(\omega)$ . The spectral density of the pulse is given by  $S(\omega)$  and  $\phi(\omega)$  is the spectral phase. The intensity functions  $I(t)$  and  $S(\omega)$  determine the time duration and spectral bandwidth of the pulse. Since the temporal and spatial characteristics of the field are related to each other through Fourier transform, the bandwidth and pulse duration cannot vary independently of each other. Their product, known as the time-bandwidth product, has a lower bound. The minimum value depends on the definition used for defining the duration and on the shape of the pulse. For a given spectrum, the minimum time-bandwidth product, and therefore the shortest pulse, is obtained by a transform-limited pulse, i.e., for a constant spectral phase  $\phi(\omega)$ . For a Gaussian pulse, the bandwidth product  $\Delta\nu \cdot \Delta t \geq 0.441$ . High values of the time-bandwidth product, on the other hand, indicate a more complex pulse.

The inherent wide spectral bandwidth of an ultrashort pulse has a significant consequence when it propagates through a material medium. The medium experiences higher refractive index for shorter wavelengths and vice-versa. This is known as group velocity dispersion. The speed of a wavelength in the material is equal to  $v = c/n$ , where  $n$  is the index of refraction for that wavelength. Therefore during propagation, the higher wavelengths of the femtosecond pulse travels faster than the shorter ones. As a result, the original short pulse becomes longer in time with the higher wavelength part arriving first to the sample. This is known as chirp. It results in temporal broadening of the pulse. It is discussed in detail in the following section.

### 2.2.2 Single wavelength versus white light probe

When employing a single wavelength as the probe, the wavelength must be selected in the spectral domain where it is known or expected that some transitions induced by the pump pulse would be present. At this point, it should be mentioned that the terminology “single” wavelength should not be taken in a strict sense since the ultrashort pulse inherently has a spectral width around the single central wavelength. Monochromatic probe pulses or pulses with narrow spectral width limit the observation window for transitions and hence the information about the optical processes too. In

time resolved optical spectroscopy, it is desirable to have smoothly tunable frequencies for the probe pulses. Such tunable probe pulses can be generated by conventional sources such as optical parametric amplifiers (OPA), tunable solid-state lasers and quantum cascaded lasers. Femtosecond OPAs, however, introduce complexity to the laser system, are expensive and difficult to align. In comparison to these sources, an alternative supercontinuum source has the advantage of covering a wider range of spectral frequencies without experiencing the time delay caused by the wavelength tuning of conventional sources. A supercontinuum white pulse can simultaneously probe all states spanning a broad energy range, rendering detailed information on the time dependent variation of optical parameters across the entire spectral range. The next section provides a brief overview of the physical background of supercontinuum generation.

### ***2.2.2.1 Supercontinuum generation of white light***

In a process known as supercontinuum (SC) generation, extreme broadening of narrow spectral laser pulses can be realized as a result of the nonlinear interactions of the intense laser pulses with the nonlinear medium in which they propagate [8,9,10,4]. Supercontinuum can be generated in materials of different nature and structure, including solid state materials, organic and inorganic liquids and gas media. The essential processes contributing to the continuum generation are common to all. The supercontinuum pulse, designed to serve as the probe pulse in time resolved pump-probe experiments, is often generated by focusing an amplified femtosecond pulse onto a silica or sapphire plate. Another source for SC generation is optical fibers which allow strong nonlinear interactions over a significant length of the fiber for the laser pulses with sufficiently high intensity, relaxing the requirements of high input laser power necessary for efficient supercontinuum generation. The supercontinuum generated in optical fibers spans the entire visible and a considerable part of the near-infrared spectral region even with input peak powers as low as 1kW [11]. However, the intensity of the supercontinuum generated in optical fibers is typically lower than that of white light produced by high-power focused laser pulses in solid state and gas media.

The supercontinuum, which derives its name from its extremely broad and continuous spectrum, can stretch over the entire visible and part of the near-infrared regions. It has unique spectral properties, a controlled pulse width and high spectral brightness. Supercontinuum generation is a complex phenomenon which involves changes in the temporal and spatial beam characteristics through nonlinear processes and requires extremely high pulse energy and extremely short pulse duration. It does not cover a specific phenomena but a number of nonlinear effects leads to considerable spectral broadening of pulses [8,12]. The processes of SC generation can be different, depending particularly on the dispersion, the pulse duration and the peak powers of the input laser pulses. When femtosecond pulses are used, the dominant physical process and the starting mechanism leading to the spectral broadening is self phase modulation (SPM) due to an intensity dependent refractive index. In addition to self phase modulation, however, a number of other nonlinear effects such as parametric four wave mixing and Raman scattering may play a role as well. For pumping with picosecond or nanosecond pulses, Raman scattering and four-wave mixing can be more important. In general, these nonlinear processes have to be considered in combination with group velocity dispersion. Thin samples tend to reduce the effect of group velocity dispersion as well as the influence of nonlinearities other than SPM.

As mentioned above, the physical mechanisms behind the laser generation of white light involve self-phase modulation. Self phase modulation is a phenomenon in which a laser pulse propagating in a medium interacts with the medium and imposes a phase modulation on itself. The strong field of a laser beam induces an appreciable intensity dependent change in the refractive index of the medium as:

$$n = n_0 + n_2 I(t) \quad (2.3)$$

where  $n_0$  is the field-free unperturbed refractive index of the medium,  $n_2$  is the nonlinear refractive index which varies with the intensity  $I(t)$  of the laser beam. In response to the intensity dependent refractive index, the medium then reacts back and inflicts a phase change on the incoming wave resulting in self phase modulation. The nonlinear phase incursion acquired by a laser pulse over a distance  $L$  in a medium with Kerr nonlinearity is written as in expression (2.4).

$$\phi(t) = \frac{\omega}{c} n_2 I(t) L \quad (2.4)$$

For pulsed laser beam as input, the temporal variation of the laser intensity leads to a self phase modulation in time. It can be inferred from expression (2.4) that the intensity dependence of the refractive index of the medium maps the temporal profile of the field intensity in a laser pulse on the time dependence of the nonlinear phase shift. Since the time derivative of the phase of the wave is the angular frequency, the time dependent phase shift gives rise to a time-dependent frequency deviation across the laser pulse and hence SPM also appears as a frequency modulation as shown by expression (2.5). This is known as chirp.

$$\Delta\omega(t) = \frac{\omega}{c} n_2 L \frac{\partial I}{\partial t} \quad (2.5)$$

$$\Delta\omega = \frac{\omega}{c} n_2 L \frac{I_0}{\tau} \quad (2.6)$$

Thus, the output beam appears with a self phase-induced spectral broadening with the maximum spectral broadening of the laser pulse estimated by equation (2.6). It is evident that it is strongly influenced by the peak intensity  $I_0$  of the laser pulse and the pulse width  $\tau$ . Since SC is a very weak effect, very high intensities are needed. Typical values are: 100fs pulses with 1 nJ energy – peak power of 10 kW. In SPM, the temporal self-action induces a symmetric spectral broadening of the laser pulses. However, the spectral broadening of the laser pulse may become asymmetric because of a number of physical factors, the three most significant include spatial self-action, shock waves and the retarded part of the nonlinear optical response of the medium.

## 2.3 Experimental details

The following sub-sections provide a detailed description of the technical aspects of the experiment employed in the presented work to perform time resolved supercontinuum transmission spectroscopic measurements on ZnO films.



### 2.3.1 Experimental set up

Titanium doped sapphire is a solid state laser medium capable of tunable operation over a broad range of near infrared wavelengths from around 720-1050nm [7,13,14]. The maximum gain and efficiency is obtained at 800nm. The Ti:Al<sub>2</sub>O<sub>3</sub> laser gain medium has Ti<sup>3+</sup> as the active ion in an aluminium oxide host lattice. Because of its wide absorption band in the blue-green region, energy for the lasing is supplied by a standard CW Nd:YVO<sub>4</sub> laser operating at 532nm. The emission band of Ti:sapphire is shifted towards lower energy side and extends from 600nm to wavelengths greater than 1000nm. However, the lasing action is possible only at wavelengths longer than 670nm because the long wavelength side of the absorption band overlaps the short wavelength end of emission spectrum. Figure 2.3 depicts the schematic arrangement of the first half of the experimental set-up.

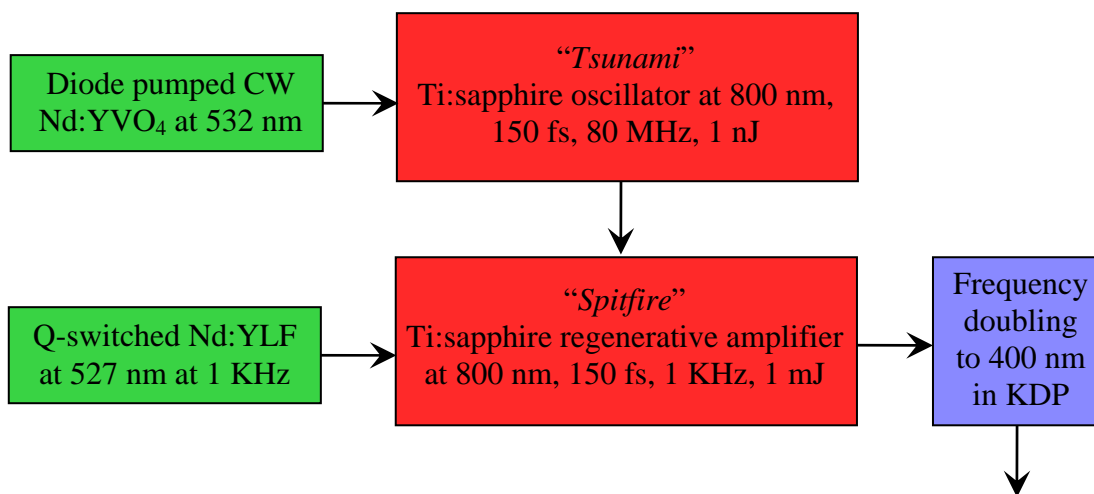


Figure 2.3 Schematic of the first half of experimental arrangement depicting the generation of 150fs pulses at 800nm by Ti:sapphire oscillator and then amplification by regenerative amplifier. The pulses are frequency doubled to 400nm in KDP crystal

The *Tsunami* mode-locked oscillator generates ultrashort pulses with a typical duration of 150fs and average output power of 1μJ per pulse at a repetition frequency of 80MHz [15,16,2,17]. Ti:sapphire laser output pulses at 800nm are directed into *Spitfire* Ti:sapphire regenerative amplifier for amplification. The Ti:sapphire provides the seed for the amplifier system. A Nd:YLF laser operating at 527nm running at 1kHz repetition rate is used as the driver for amplification. The regenerative amplifier consists of a resonator in which the injected seed pulse makes several round trips achieving very high gains. This principle is coupled with chirped pulse amplification since the peak power in the amplifier becomes too high. Pulses with high peak power undergo self-focussing destructively because of the nonlinearity in the index of refraction making it a limiting factor. The *Spitfire* finds its way around by using a series of gratings as the dispersive element to stretch the duration of pulses before they actually enter the amplifier and thus reducing its self-focusing induced damage significantly. The amplifier amplifies the original seed pulses by a million times converting the low-power output of the seed-laser at 80 MHz repetition rate to high-power 1mJ per pulse output at 1 kHz. After amplification, the pulse is then temporally recompressed to its original duration by a grating pair with essentially the opposite dispersion. Next, the amplified 800nm output is fed into KDP crystal for second harmonic generation [18,19]. The

output is frequency doubled 400nm beam. For pump wavelength dependent measurements, the *Tsunami* oscillator was also tuned to yield output at 782nm and 818nm. Then the output of 391nm and 409nm wavelengths respectively could be achieved after the second harmonic.

**Pump part:** The frequency doubled 400nm beam is split into two by a beam splitter (80:20). Figure 2.4 depicts the schematic arrangement of the latter part of the experimental set-up. The larger fraction (80%) is transmitted as pump pulse so that a broader selection of higher excited states can be accessed. The pump pulse travels to the sample via a fixed path. There is a fixed delay line in this part required to make the optical path difference same initially for both the pump and probe beams, right on the sample. An optical chopper is placed to have the desired repetition rate of the pump pulses, by repetitively switching light beam on and off. An arrangement of half wave plate and a polarizer is also placed to vary the energy of the pump beam, should this be necessary. The light beam directed with the help of mirrors is focused onto the sample using a lens.

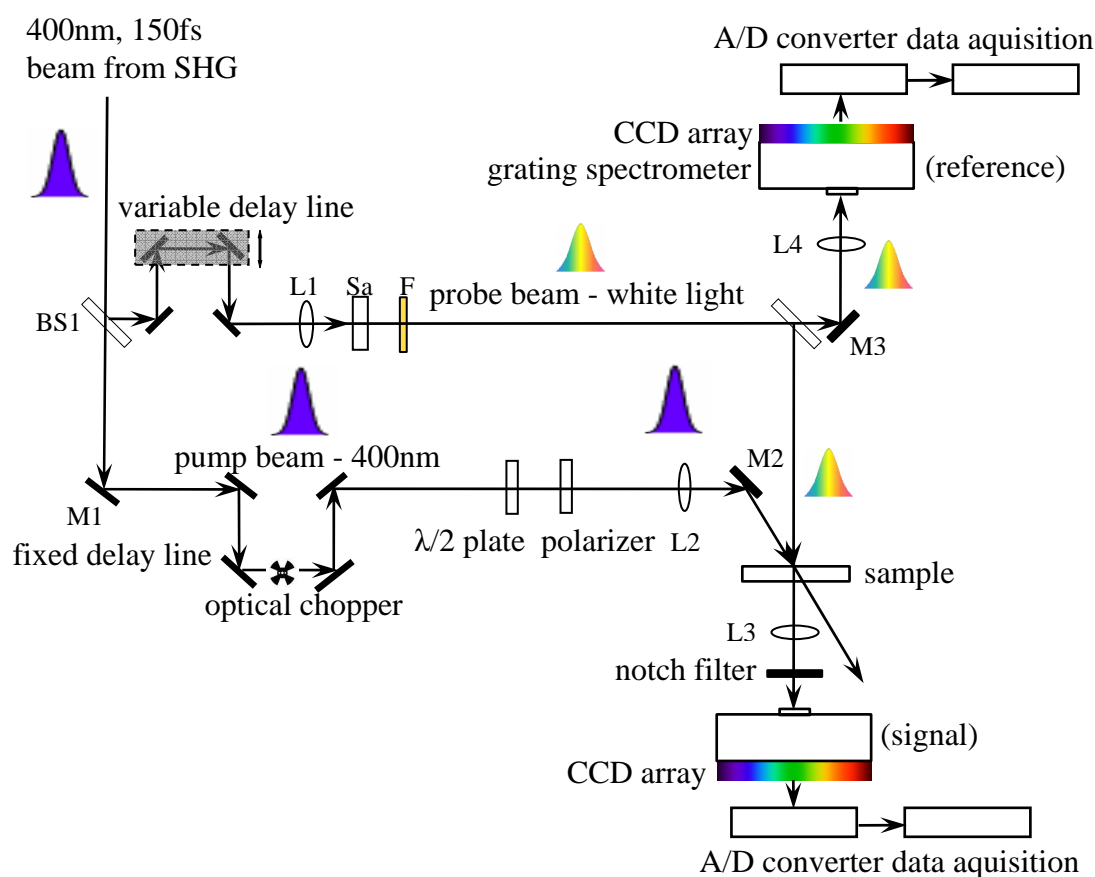


Figure 2.4 Schematic of the latter half of the experimental set up

Since only the transmission of the probe beam ought to be measured by the detector, the pump pulse is configured to photoexcite the sample at an angle with respect to the probe beam, as shown in figure 2.4. In order to prevent the pump light from interfering with the detection of the probe signal, it is further shielded from the detector by placing a pinhole in front of it. The spectrum of the frequency doubled laser pulse at  $\lambda=400\text{nm}$  used as the excitation pump pulse is shown in figure 2.5. The full width at half maximum (FWHM) for the pump pulse is 2.2 nm. The spot size of the beam is  $\sim 110\mu\text{m}$ .

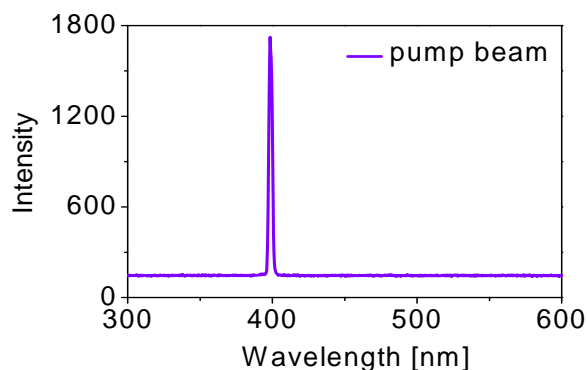


Figure 2.5 Spectrum of 400nm pump beam

**Probe part:** The smaller fraction of the beam after getting reflected from beam splitter passes through a variable delay line. Delay line is a device that lengthens the path the probe light has to travel relative to the pump beam. Varying the path length will in effect vary the time delay between the pump and probe pulses. It consists of a retro-reflector on a rail system. The retroreflector can be positioned along a precise motorized translational stage by computer control of a stepper motor. For instance, if the retroreflector moves backwards and lengthens the path, it takes that much longer for the probe light to reach the sample than the pump beam. The 400nm pulse after passing through the optical delay is focused on a sapphire plate to generate supercontinuum white light. The generated continuum is sent through a filter filled with yellow coumarine dye solution diluted in methanol in order to suppress the contribution of the 400nm fundamental wavelength from the white light spectrum. For efficient absorption of the 400nm from the white light spectrum, the dye solution is constantly replaced by the solution in a connected bottle and circulated through the cuvette. It is crucial to ensure that the energy of the probe pulse is sufficiently low to ascertain that it itself does not induce any significant pumping of the sample volume into the excited state. Following different optical paths, the pump and probe beams are finally focussed onto the sample and aligned to have maximum spatial overlap between them at the sample surface. A 400nm notch filter placed before the detector suppresses all the scattering from the sample occurring at the pump wavelength. The output beam is then directed to the “signal” grating spectrometer which serves as the detector. Owing to the lack of reproducibility of white light from pulse to pulse, direct measurement of the ratio of probe before and after pump pulse is not sufficient. The fluctuations of white light are normalised and accounted for by introducing a reference spectrometer. A part of the unchanged probe beam is also directed to a “reference” grating spectrometer. For every measurement, the probe pulse bearing the effect of change caused due to the pump pulse, is always monitored and compared with respect to the unchanged reference spectrum. It is discussed in more detail in section 2.3.2. The grating spectrometers which detect the differential transmission spectrum work by spreading out the incoming light according to the wavelength of the photon. The signal is then sent to data acquisition system. The measured spectra can be viewed in a software designed specially for the pump-probe set-up. Different parameters such as delay line and number of laser shorts etc. can be controlled in it.

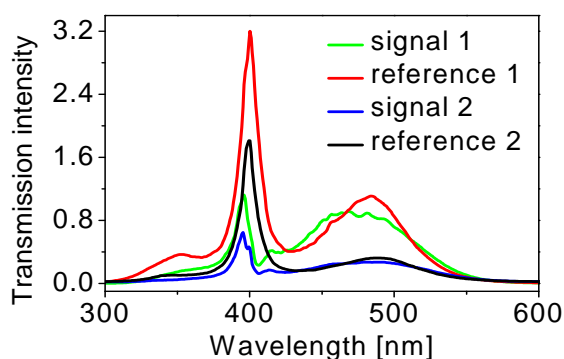


Figure 2.6 Spectra of supercontinuum probe beam

Figure 2.6 shows the spectrum of the broad white light used as the probe pulse to investigate the dynamics of the excited system with continuous spectral components ranging from 320 to 560nm. It can be seen from the figure that even after suppression of the fundamental wavelength by the coumarine dye filter, the spectrum of the supercontinuum generated by high energy pulses at 400nm features a well-pronounced peak at the fundamental wavelength. The spectral density decreases rapidly in the wings since the pulse energy of the input pulse is spread over the whole bandwidth, leading to smaller intensities in wavelength ranges far from the fundamental wavelength. The properties of the spectrally broadened white light vary substantially from pulse to pulse. Figure 2.6 illustrates the two sets of supercontinuum spectra for the signal and reference spectrometers, labelled as 1 and 2. The spectral profile and the corresponding intensity of the two white light pulses is not exactly the same. A lot of rapid fluctuations occur in different spectral components of the white light continuum.

**Determination of approximate “zero-time”:** The delay line can be precisely controlled by the software which includes a provision to change the time steps as well as the “zero-time”. Delay time zero is defined as the time when the peaks of the pump and probe beams overlap in time at the sample surface. Initially, the displayed zero-time in the software may not be the actual one for an unadjusted delay line. In order to find the position in the delay line which corresponds to actual zero-time, it is calibrated using coumarine dye solution diluted in methanol. At negative delay times (when the probe arrives earlier than the pump), there is no signal due to the pump pulse. The signal appears only when the probe arrives later than the pump. The dye gives a large and long lived signal lasting over several picoseconds, thus making it easier to detect the signal. This signal from the dye is monitored by changing the delay time between the pump and probe. The time (and the corresponding delay position) for which the signal just seems to start is set as the zero-time.

### 2.3.2 Data acquisition

For normalization of the measurement, a probe pulse is measured before the excitation of the sample. The pump pulse excites the sample at  $t_d=0$ . Thereafter, a second probe pulse records the transmission changes caused by the preceding pump pulse at a variable delay time. Apart from measuring the probe beams before and after the pump pulse, reference beams as well as ambient light is recorded in the transient spectra in order to remove any undesired stray light contribution. The exact method of

measurement of the change in optical density spectrum is as follows: The ambient light and electronic noise are recorded by the spectrometers in the absence of both pump and probe beams as the dark current signals. They are denoted as  $I_D^{sig}(\lambda)$  and  $I_D^{ref}(\lambda)$  for signal and reference spectrometers respectively. The spectrometers then record the spectral distribution of the probe beam superimposed to the dark noise only, in the absence of pump pulse as  $I_0^{sig}(\lambda)$  and  $I_0^{ref}(\lambda)$ .

$$T_0(\lambda) = \frac{I_0^{sig}(\lambda) - I_D^{sig}(\lambda)}{I_0^{ref}(\lambda) - I_D^{ref}(\lambda)} \quad (2.7)$$

$$T(\lambda) = \frac{I^{sig}(\lambda) - I_D^{sig}(\lambda)}{I^{ref}(\lambda) - I_D^{ref}(\lambda)} \quad (2.8)$$

$$\Delta OD(\lambda) = \log\left(\frac{T_0(\lambda)}{T(\lambda)}\right) \quad (2.9)$$

The transmission before the pump excitation,  $T_0(\lambda)$ , normalized with respect to the reference signal is calculated using equation (2.7). Equation (2.8) calculates the normalized transmission  $T(\lambda)$  after the pump excitation from the corresponding spectra  $I^{sig}(\lambda)$  and  $I^{ref}(\lambda)$ . For a given delay time  $t_d$ , the change in optical density,  $\Delta OD(\lambda)$ , corrected for all the undesired noise and fluctuations due to white light instability, is calculated by taking the logarithm of the differential transmission spectrum according to equation (2.9). It should be noted that positive  $\Delta OD(\lambda)$  corresponds to increase in absorption while negative  $\Delta OD(\lambda)$  is increase in transmission or bleaching. The need for such a complex triggering and measurement arises due to the instability of the probe white light.

**Triggering scheme of pulses:** Figure 2.7 shows the triggering scheme of the pump and probe pulses. At first the probe pulse is measured before excitation of the sample. Then the pump pulse excites the sample at  $t_d=0$ . Thereafter, a second probe pulse is measured at a delay time  $t_d > 0$  after the excitation. This pulse bears the effect of the optical changes in the sample caused by the preceding pump pulse. The designed sequences of pump and probe pulses, shown in a single grey block in the schematic, corresponds to one measurement at one delay position. This measurement is done at variable delay

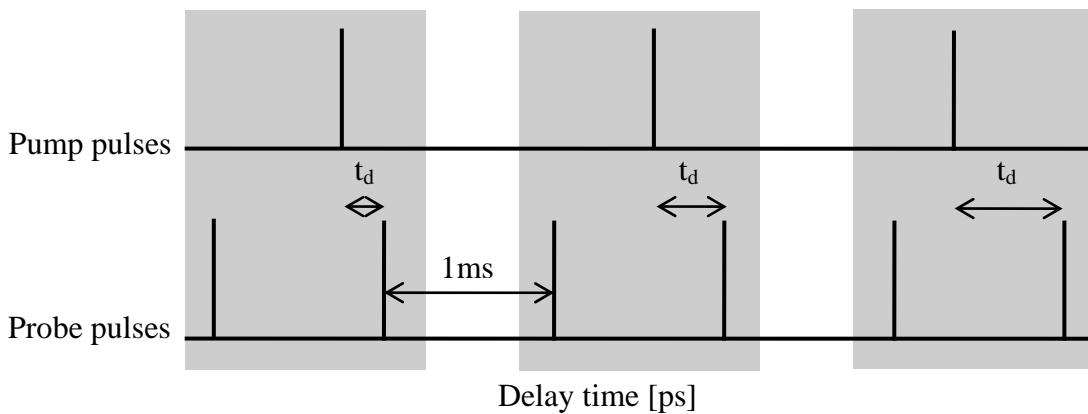


Figure 2.7 Schematic depicting the triggering scheme of pump and probe pulses

times to construct the temporal evolution of the change in optical density spectrum. The repetition rate of probe pulses is 1KHz and that of the pump pulses is 500Hz. For each delay time, the sample volume is repeatedly excited by a succession of laser shots and the accumulated signal collected by the detection system is then averaged. The number of laser shots is controlled by the software. Averaging over a large number of laser shots (typically 1000) abridges the random noise signals, improves the signal to noise ratio and hence enhances the stability and accuracy of the collected spectral data. However, care must be taken about the photo-destruction of the sample from overexposure to high energy pulses. Moreover, very large number of laser shots introduces additional acquisition time.

### 2.3.3 Accuracy of pump-probe experiments

**Temporal resolution:** The temporal resolution in pump-probe experiments is limited by the duration of the pump and probe pulses which, in the presented work, is 150fs. Convoluting it with that of the probe pulse (~100fs), the cross correlation turns out to be approximately ~200fs. For time delays shorter than the pulse duration, the probe coherently interacts with the pump pulse and these coherent processes may be superposing on incoherent ones. Coherent effects can be avoided by probing at sufficiently large delay times such that the excitation of the pump experiences phase loss due to dephasing processes before the arrival of the leading edge of the probe. Any process occurring faster than pulse width must be studied with care. The temporal overlap between pump and probe pulses ultimately defines the time-resolution of the system. In addition, the duration of the pump and probe pulses must be shorter than the relaxation times of the dynamical processes under study. It is also important to pump the sample at regular intervals that are longer than the response time of the sample to ensure that there is no overlap of excitation events from the current pump and the previous one. Additionally, the time between successive probe pulses, as defined by the pulse repetition rate, must not exceed the time taken for the carriers under study to decay back to the ground state.

**Data acquisition rate and signal to noise ratio:** The key desirable features for the detector are sensitivity and response time as given by repetition rate. With the aforementioned triggering scheme, the frequency of probe pulse is 1kHz and that of the pump pulse is 500Hz. A high sensitivity is required to measure the weak signals. With a long pulse, a detector with a short time resolution can distinguish the difference between the excitation pulse and the emission decay. The data read out rate is 1MHz. The detection electronics makes it possible to measure transient transmission changes as small as  $10^{-4}$ .

**Spectral resolution:** The spectral resolution of the diode lines in the grating spectrometer is 0.8nm. As mentioned earlier, the femtosecond pulses being ultrashort have broad spectral width. The 150fs pump pulse has a width of ~2.2nm at FWHM. As a consequence, upon perturbation by the pump pulse, transitions occur between a narrow range of states instead of one sharp level.

Spatial pump-probe overlap is another very critical factor for efficient utilization of the pump energy. The pump converts a relatively small percentage of the sample volume into the excited state manifold. Having maximum pump-probe overlap ensures that the probe beam will measure the transient changes in the entire volume excited by the pump.

## 2.3.4 Processing of time resolved data

### 2.3.4.1 Zero-time and chirp correction

The supercontinuum is chirped due to self-phase modulation and group velocity dispersion as they propagate. Since the required broad spectrum is obtained by nonlinear broadening, there is often substantial chirp on the pulse. So, different spectral components of the probe enter the sample at different times for any specific setting of the pump-probe delay. The blue wavelengths arrive at the sample later than the red wavelengths. Therefore, if the delay between pump and probe beams is changed, the shape of the recorded spectrum may also change. Suppose that the pump beam arrives at the sample later than the probe. In this case, the probe beam will not be perturbed. If this delay is changed a little, the red wavelengths could still arrive before the pump beam and not be affected. But now the blue wavelengths could be in phase with the pump beam and would thus be perturbed. Only the blue part of the spectrum would reflect the perturbation. Changing this delay more and more would shift the interaction into the red part of the spectrum. This frequency chirping effect limits the time resolution of the measurement.

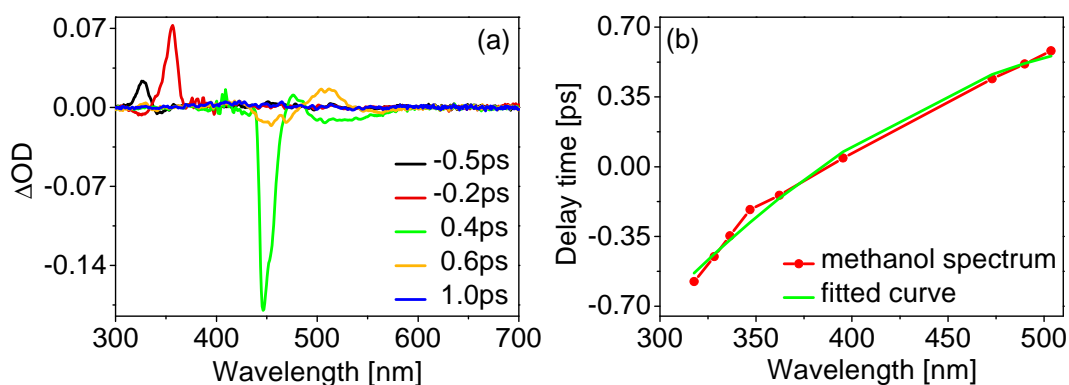


Figure 2.8 (a) Time resolved spectra of methanol used for chirp correction (b) Chirp spectrum obtained from methanol along with the fitted curve

For a good time resolution, the measured data ought to be compensated for chirp. This can be done only if the dispersion of the supercontinuum is well known. The chirp is compensated for by using methanol as its signal has a very fast response time of less than 1ps, shown in figure 2.8(a). The signal appears at various positions across a wide spectral range for different delay times ranging between -0.5 to 0.8ps. Changing the delay time between the pump and probe makes it possible to determine at what time the maximum signal is reached, i.e. the time at which the pump and probe pulses coincide perfectly for a given wavelength. The recorded methanol spectra is analysed in the software and is fitted with a second order polynomial [20]. Figure 2.8(b) illustrates the chirp spectrum obtained from the experimental data of methanol and the corresponding fitted curve. In this way, one obtains the dispersion curve, which is then used for numerical correction of the measured data. Moreover, the correction also determines the actual zero time for each wavelength which is crucial for the correct interpretation of the ultrafast dynamics. All the time resolved data presented in the rest of the thesis has been corrected for chirp.

### 2.3.4.2 Correction for scattering

In the time resolved spectra for ZnO samples, a broad contribution appears at 400nm which is present at negative as well as positive delay times. This is due to scattering of the pump wavelength at the sample. Figure 2.9 shows time traces for 458nm thick ZnO film for selected negative and positive delay times.

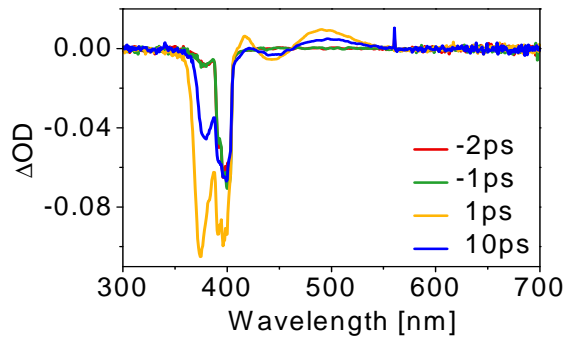


Figure 2.9 Scattering at 400nm in the time resolved spectra of 458nm thick ZnO film

It is evident from the figure that the scattering contribution is large in spite of suppression from 400nm notch filter. Assuming that apart from scattering no real signal would be present at negative delay times, the spectrum from negative delay time is subtracted from the spectra of all other delay times to get rid of the scattering (noise) from the time resolved data. The scattering spectrum to be subtracted is obtained by averaging the spectra of 6 negative delay times, thus increasing the accuracy. All the transient data presented in the rest of the thesis has been corrected in this way.

### 2.3.5 Example of time resolved data

The measured time resolved pump-probe data is three dimensional; the three axes being wavelength, delay time and change in optical density. The optical density changes are measured for continuous spectral positions (~500 points between 300-700nm) and several delay times (~364 points between 0-900ps). The data can be carefully studied and analyzed in detail in specially designed software. As an

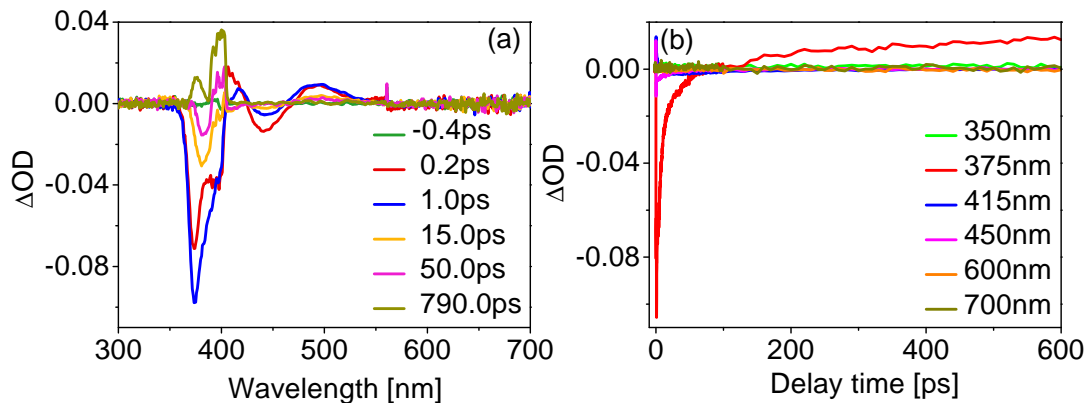


Figure 2.10 Corrected time resolved spectra for 458nm thick ZnO film (a) Change in optical density as function of wavelength (b) Optical density change as function of time



illustration, figures 2.10(a) and (b) show typical scattering as well as chirp corrected spectra for the spectral changes in the optical density for different delay times obtained from the pump probe experiments done on 458nm thick ZnO film. The optical density changes are measured as a function of wavelength for a series of delay time.

## 2.4 Determination of optical properties of ZnO films

**Dielectric function measurements of ZnO films:** Dielectric function which is a fundamental property of the material can be obtained from ellipsometry. Ellipsometry is a versatile and sensitive optical technique for determining dielectric properties of thin films. It measures the change in the polarization state of light when it is reflected from a sample. The exact nature of polarization change is governed by the sample's fundamental properties namely the dielectric function and the thickness. Therefore, through analysis of the modified state of polarization of the reflected light, these fundamental parameters can be accurately determined. Knowledge of these fundamental parameters enables one to study a range of other sample properties such as crystal quality, uniformity, chemical composition and anisotropy. Ellipsometry is also commonly used to characterize film thickness ranging from a few angstroms to several micrometers with an excellent accuracy. Although optical techniques are inherently diffraction limited, spectroscopic ellipsometry can achieve angstrom resolution and is non-destructive and contactless [21,22,23,24].

Linearly polarized light with its polarization state decomposed into an  $s$  and a  $p$  component (the  $s$ -component is oscillating parallel to the sample surface, and the  $p$  component is oscillating parallel to the plane of incidence), is reflected at oblique incidence from the sample surface. The reflected light is elliptically polarized with the  $s$  and  $p$  components experiencing different attenuation and phase shift according to the Fresnel's equations. The shape and orientation of the ellipse depend on the angle of incidence, the direction of the polarization of the incident light, and the reflection properties of the surface. Ellipsometry measures the complex ratio  $\rho$  between Fresnel's reflection coefficients of the  $s$  and  $p$  components, denoted by  $r_s$  and  $r_p$ , respectively. The relative phase change of the  $s$  and  $p$  components of the electric field vector  $\Delta$  and the relative amplitude change  $\Psi$ , upon reflection from the surface are given by the equation (2.10).

$$\rho = \frac{r_p}{r_s} = \tan\Psi \cdot e^{i\Delta} \quad (2.10)$$

Since ellipsometry measures the ratio of the reflected intensities, rather than the absolute value of either, it is not as susceptible to scattering and fluctuations. Additionally, it requires no reference sample or calibration. These salient features make it a very accurate and reproducible technique. The measured  $\Psi$  and  $\Delta$  cannot be directly converted into the optical constants of the sample. Therefore, a layer model is formulated which considers the optical constants (dielectric function) and thickness parameters of all individual layers of the sample and the model analysis is performed. By implementing an iterative regression analysis procedure, theoretical data are generated by varying unknown optical constants as well as thickness and  $\Psi$  and  $\Delta$  are calculated using the Fresnel equations. The calculated values of  $\Psi$  and  $\Delta$ , which match the experimental data, provide the dielectric function and thickness of the sample.

The ellipsometric measurements were performed on a commercial VASE ellipsometer from the J. A. Woollam Company. These measurements and the data evaluation were done in the semiconductor group of the University of Leipzig.

**Transmission measurements of ZnO films:** Transmission measurements on the ZnO films were performed on Shimadzu UV-Visible 3100 spectrophotometer between 300-700nm.

**Atomic force microscopy on ZnO films:** Atomic force microscope images of the ZnO films were measured with WITec Scanning near-field optical microscope (AlphaSNOM).

**Microscopic images of ZnO films:** Microscopic images of ZnO films were taken with Zeiss axioplan 2 imaging and axiophot 2 microscope.

**Thermal admittance spectroscopy of ZnO films:** The TAS measurements done to electrically characterize the ZnO films were performed on 4294A Precision impedance analyser by Agilent company. These measurements were done in the semiconductor group in the University of Leipzig.

## Chapter 3. Sample analysis

### 3.1 Basics of semiconductors

#### 3.1.1 Bandstructure and optical properties of semiconductors

A semiconductor is a material which has a conductivity intermediate between that of a conductor and an insulator. The conductivity of a semiconductor can be varied by varying the temperature, by doping the material with impurity atoms, or by illuminating it with light of the appropriate wavelength. The electrical conduction in a semiconductor is caused by the motion of the electrons in the conduction band and also by that of the holes in the valence band. The valence band is completely filled and the conduction band is empty but the forbidden gap between the conduction band and the valence band is smaller compared to that of an insulator. It is the forbidden energy region between the maximum of the valence band and the minimum of the conduction band. Both the bands near their maxima and minima have parabolic dispersion.

The energy bands are characterized by a certain value of k-vector in the Brillouin zone. Semiconductors can be classified as direct and indirect bandgap semiconductors [1]. In a direct bandgap semiconductor, the maximum of valence band and the minimum of conduction band correspond to the same value of the wave vector k. In contrast, a semiconductor in which the bottom of the conduction band and the top of valence band have different k-values is the indirect semiconductor. These direct and indirect transitions are schematically shown in figure 3.1. This has significant implications on light absorption and radiative recombination of electrons with holes. Interactions among electrons, holes, phonons, photons, and other particles are required to satisfy conservation of energy and conservation of crystal momentum. A photon with energy near a semiconductor bandgap has almost zero momentum. In direct semiconductor, transfer of carriers during absorption or emission of photons occurs at the same wave vector at  $\Gamma$  point ( $k=0$ ) in the momentum space. Vertical optical transitions are allowed, therefore phonons do not take part in direct transitions. In an indirect semiconductor, direct transition across the bandgap does not conserve momentum and hence is forbidden. Since the wave vector k of the phonons is much larger than that of the photons, phonon transitions accompany the indirect transitions to satisfy the momentum conservation law. Typically this process is achieved in several steps. The electron will first move to a trap site in the forbidden band before moving into the valence band. A change in potential energy will result in the release of a

photon, while change in momentum will produce a phonon. Since a third particle phonon is required, the probability of photon emission is comparatively much lower for indirect semiconductor and the resulting phonon-mediated light emission through radiative recombination is much slower, inefficient and weak. For this reason, the direct semiconductors are superior to indirect ones for optoelectronic applications.

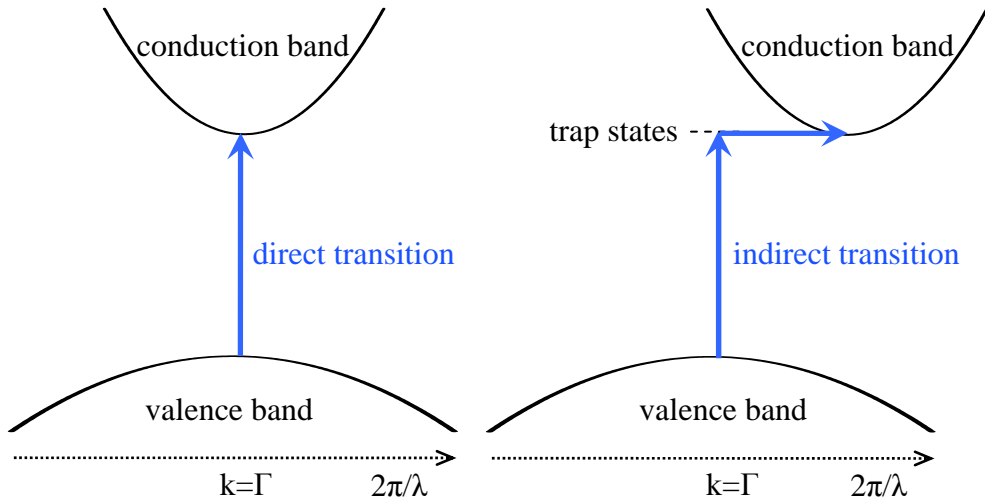


Figure 3.1 Schematic of transitions in direct and indirect semiconductors

All of the optical properties of a semiconductor are determined by its electronic bandstructure and the bandgap [2,3]. If excited by thermal energy, light, or electron beams, the electrons absorb the energy and transit to high energy states consequently creating holes in the valence band. These transitions of electrons from lower to higher states are called *excitations*. Photo-excitation can occur only when the frequency of the incident photon is resonant with that equivalent to the bandgap, unless donor or defect states are present within the bandgap, then that frequency is absorbed and the electrons are excited to the conduction band. Usually the excited electron and hole in the valence band move independent of each other. However in some cases, they are bound together by Coulomb attraction. This neutral bound electron-hole pair is known as exciton [4,5,6]. Since an exciton results from the binding of an electron and a hole, it has slightly less energy than an unbound electron and hole and is therefore located just below the band gap. As they have no charge; they do not contribute to electrical conduction. They play a significant role in the dynamics of semiconductors [7,8].

Excited states are unstable since every system tries to acquire the lowest energy state. As a consequence, the electrons in high energy states transit to lower ones in a certain lifetimes and the process is known as *relaxations*. During the relaxation, electrons neutralize the corresponding holes and these transitions are designated as *recombinations*. Recombinations can either be *radiative* or *nonradiative*. Radiative recombinations emit photons with energy that corresponds to the difference between the two involved states. On the other hand, in nonradiative recombinations, the phonons are emitted to crystal lattices or the electrons are trapped in the defects and the transition energy is emitted in forms other than light. Efficient light emitting devices call for minimum nonradiative recombinations in semiconductors.

Light emission due to radiative recombinations is called *luminescence*. Light emission process can be classified according to lifetime, excitation methods and energy states involved. According to the lifetime, light emission is classified into *fluorescence* which lasts for a short time of  $10^{-9}$ - $10^{-3}$ s or they are classified into *phosphorescence* with a long lifetime of  $10^{-3}$ s to a day. According to the excitation, the photoinduced luminescence is known as *Stokes* and *anti-Stokes luminescence* depending on whether the photon energy of pumping light is higher or lower than that of the luminescence respectively. According to the transitions states involved, the light emission processes can be classified into *impurity recombinations* between either electrons in the conduction band with the holes in the acceptor levels or the electrons in the donor levels with the holes in the valence band, or they can be classified as *interband recombinations* between carriers of the conduction and valence bands or they can be *exciton recombinations* taking place due to eventual decay of excitons.

There are two types of radiations: *spontaneous emission* and *stimulated emission*. Spontaneous emission is a radiative process in which an excited electron decays in a certain lifetime by emitting a photon. It occurs irrespective of the incident light. In contrast, in stimulated emission, the incident light induces a radiative transition of an excited electron and the resulting emitted photon has the same wavelength, phase and directionality as the incident one. Therefore, the emitted light is highly monochromatic, coherent and directional. In stimulated emission, the light is amplified since the incident photon generates two output photons. In thermal equilibrium, there are more electrons in the lower state than in the higher one. Therefore, only the absorption is observed when light is incident on a material. In order to achieve a net optical gain, the number of electrons in the higher state must be larger than that in the lower one. This condition is known as population inversion. Population inversion occurs only in the vicinity of the bandedges by excitation of electrons through optical pumping or electric current injection.

**Dielectric function related optical constants:** The propagation of the beam through a transparent medium is described by wavelength dependent refractive index  $n(\lambda)$ . The dependence of refractive index on the wavelength is known as dispersion. Transmission or transmissivity  $T(\lambda)$  is defined as ratio of the incident power to the transmitted power. In the absence of absorption and scattering losses, the transmission and reflection  $R(\lambda)$  equals unity by the conservation of energy, as shown in equation (3.1).

$$R(\lambda) + T(\lambda) = 1 \quad (3.1)$$

The absorption of light by an optical medium is quantified by the wavelength dependent absorption coefficient  $\alpha(\lambda)$  which is defined as the fraction of the intensity absorbed in a unit length of the medium. Equation (3.2) describes the intensity of light  $I(\lambda)$  at depth  $z$  of the absorbing medium where  $I_0$  is the incident intensity.

$$I(\lambda, z) = I_0 e^{-\alpha(\lambda)z} \quad (3.2)$$

$$\varepsilon(\lambda) = \varepsilon_1(\lambda) + i \cdot \varepsilon_2(\lambda) \quad (3.3)$$

$$\kappa(\lambda) = \sqrt{\frac{\sqrt{\varepsilon_1(\lambda)^2 + \varepsilon_2(\lambda)^2} - \varepsilon_1(\lambda)}{2}}, n(\lambda) = \sqrt{\frac{\sqrt{\varepsilon_1(\lambda)^2 + \varepsilon_2(\lambda)^2} + \varepsilon_1(\lambda)}{2}} \quad (3.4)$$

The absorption coefficient and the refractive index, which governs most of the optical properties of a material is described by a single complex quantity known as the dielectric function  $\varepsilon(\lambda)$  (written as equation (3.3)). It can be deduced from equation (3.4) that the extinction coefficient (absorption) is primarily given by the imaginary part of the dielectric function whereas the refractive index is mainly determined by its real part. The absorption coefficient of the medium can be calculated as given by equation (3.5). The reflectivity  $R(\lambda)$ , also shown in the adjacent expression, is dependent on both  $n(\lambda)$  and  $\alpha(\lambda)$ .

$$\alpha(\lambda) = \frac{4\pi\kappa(\lambda)}{\lambda}, R(\lambda) = \frac{(n(\lambda)-1)^2 + \kappa(\lambda)^2}{(n(\lambda)+1)^2 + \kappa(\lambda)^2} \quad (3.5)$$

### 3.1.2 Doping and defects in semiconductors

An ideal, pure semiconductor is free of every impurity and is perfectly crystallized. The electrical conductivity of a pure semiconductor, also known as intrinsic semiconductor, is strongly governed by the bandgap. The only available carriers for conduction are the electrons excited from the valence band to the conduction band. From Fermi-Dirac statistics, the probability of occurrence of these excitations is proportional to  $\exp(-E_g/kT)$  where  $E_g$  is the band gap energy,  $k$  is Boltzmann's constant and  $T$  is the temperature. In contrast, the optical and electronic properties can be significantly modified by temperature and deliberate addition of a desirable impurity into the crystal lattice of a pure semiconductor in a controlled manner by a process known as doping. The suitable dopants are classified as either acceptors or donors, depending on the atomic properties of both the dopant and the material to be doped. Semiconductors in which donor atoms provide free electrons are referred to as n-type semiconductor. A donor atom provides free electrons to the material, creating excess negative charge carriers. These weakly-bound electrons can move about in the crystal lattice relatively freely and can facilitate conduction in the presence of an electric field. Conversely, an activated acceptor produces a hole and the corresponding semiconductor is classified as p-type. Doping a semiconductor crystal introduces allowed energy states within the band gap but very close to the energy band that corresponds with the dopant type. Donor impurities create states near the conduction band while acceptors create states near the valence band. The energy difference between these energy states and the nearest energy band, referred to as dopant-site bonding energy, is relatively small. Since it is so small, the thermal energy available at room temperature is sufficient to ionize most of the dopant and create free carriers in the conduction or valence bands. In addition to intentional doping, inherent defects in the crystal can also significantly contribute to the conduction in semiconductors. Defects and impurities are found to play a significant role in controlling the semiconductor optical and electronic properties [9]. Optical transitions between donor levels and conduction band states are traced deep in the infrared region, as a consequence of the low value of donor ionization energies.

## 3.2 Physical properties of zinc oxide

### 3.2.1 Bandstructure of ZnO

Zinc oxide crystallizes in hexagonal wurtzite crystal structure with lattice parameters  $a=0.325nm$  and  $c=0.512nm$  [10]. Belonging to the space group  $P_{63}mc$ , this

hexagonal lattice is characterized by two interconnecting sublattices of  $\text{Zn}^{2+}$  and  $\text{O}^{2-}$ , such that each Zn ion is surrounded by a tetrahedral of O ions and vice-versa. Figure 3.2(a) depicts the crystallographic indices and orientations of  $a$ ,  $r$ , and  $c$  planes exemplarily within the hexagonal unit cell. Zinc oxide is a II-VI direct bandgap semiconductor with a large bandgap energy of  $\sim 3.37$  eV at room temperature.

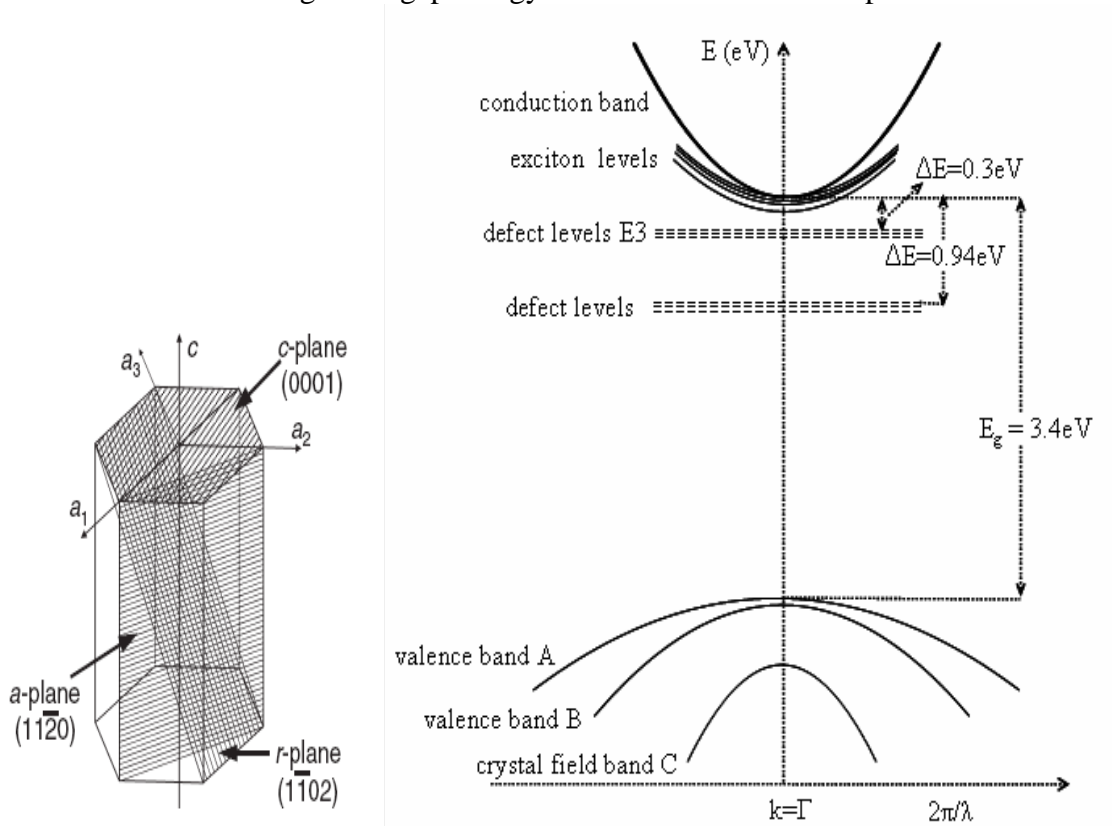


Figure 3.2 (a) Schematic of the hexagonal lattice unit cell of ZnO (b) Energy bandstructure of ZnO

The valence band corresponding to O 2p bonding states is split into three double degenerate bands due to spin orbit and crystal-field splitting. These three valence bands, denoted as A, B and C, possess quantum numbers  $J_z=1/2$  ( $\Gamma_7$ ),  $3/2$  ( $\Gamma_9$ ) and  $1/2$  ( $\Gamma_7$ ) respectively. A schematic of the energy bandstructure of ZnO in its simplest form is shown in figure 3.2(b). The first conduction band, which is strongly Zn localized, corresponds to empty Zn 3s levels and possesses  $\Gamma_7$  symmetry [11,10,12]. The excitons in ZnO are quite stable at room temperature and have a large binding energy of  $\sim 60$  meV [13].

### 3.2.2 Doping and defects in ZnO

The ZnO films under investigation were nominally undoped. ZnO possess n-type character due to the presence native point defects such as oxygen vacancies ( $\text{V}_\text{O}$ ) or zinc interstitials ( $\text{Zn}_\text{I}$ ). Optically detected magnetic resonance experiments have revealed that  $\text{V}_\text{O}$  is the cause of green luminescence band peaking at 2.45 eV ( $\sim 506$  nm) with a halfwidth of 450 meV at 4 K in ZnO. It originates from a spin triplet state ( $S=1$ ) of the neutral vacancy  $\text{V}_\text{O}^0$ . Electrically active defects in ZnO labelled as E3 and E4 detected through deep level transient spectroscopy (DLTS) measurements have been attributed to intrinsic defects namely oxygen vacancies and zinc interstitials [14,9].

They are reported to be  $\sim 290\text{meV}$  and  $\sim 530\text{meV}$  below the conduction band minimum respectively [22]. Optical DLTS measurements have shown that E3 is not optically active. On the other hand, E4 defects are optically active. Photoluminescence and DLTS measurements performed by Hofmann et al showed that there is a correlation between a broad unstructured emission at  $2.45\text{eV}$  green luminescence band and a donor level  $530\text{meV}$  below the conduction band minimum (E4) [21]. Recent breakthroughs have challenged the traditionally accepted knowledge about intrinsic defects as being the cause of n-type character in ZnO. Kohan et al and Janotti et al have theoretically proven that both  $V_{\text{O}}$  and  $Zn_{\text{I}}$  are deep donors and have high formation energies [15,16,17]. An alternative explanation has been proposed that unintentional substitutional hydrogen impurities is always a donor since it has low formation energy to produce free electrons and is easily ionized [18]. Hydrogen would be a dominant donor in ZnO materials that were exposed to it during their growth process. In addition to these native defects, there may be other kinds of defects present such as surface defects or line defects.

### 3.3 ZnO samples under investigation

#### 3.3.1 Sample preparation by pulsed laser deposition

ZnO thin films were deposited by the pulsed laser deposition (PLD) film growth technique. In PLD, the target material is vaporised using a high power pulsed laser beam inside a vacuum chamber followed by the condensation of the ablated material onto the substrate as a thin film. The detailed mechanisms of PLD are complex which includes the laser ablation process of the target material, the development of a highly forward directed plume of gas phase material followed by condensation of the ablated material on the heated substrate and nucleation of growth of the thin film [19]. The adjustable experimental parameters are the laser fluence, substrate to target distance, background oxygen pressure and the substrate temperature. Film quality is determined by the selected laser wavelength, target composition, its structure and density and the identity of the substrate (amorphous or single crystal and the lattice matching). Each of these steps is crucial for the crystallinity and uniformity of the resulting film [20].

The films were deposited in oxygen atmosphere with a background pressure of  $0.016\text{mbar}$  and  $0.002\text{mbar}$  for two sets of films deposited on *a*-plane and *c*-plane sapphire substrates respectively. The deposition temperature was  $650^{\circ}\text{C}$ . The target to substrate distance was  $10\text{cm}$  and the laser energy was  $600\text{mJ}$  with a repetition rate of  $15\text{Hz}$ . There was no intentional doping during the PLD. The undoped, naturally n-type ZnO in the synthesised thin films is *c*-axis oriented and crystalline in nature [10]. A set of five ZnO films with thicknesses of  $264\text{nm}\pm 3\text{nm}$  (E857),  $458\text{nm}\pm 3\text{nm}$  (E859) thick ZnO films on *c*-plane sapphire and  $98\text{nm}\pm 3\text{nm}$  (E1964),  $227\text{nm}\pm 3\text{nm}$  (E1963),  $476\text{nm}\pm 3\text{nm}$  (E1962) thick ZnO films on *a*-plane sapphire were chosen for the study. These thicknesses were determined by ellipsometry. From here onwards, E19xx and E8xx nomenclature for the two sets of ZnO samples will be followed in the rest of the presented work. The difference between the two series of ZnO films is that in ZnO deposited on *c*-plane sapphire, in-plane oriented domains can exist. For ZnO deposited on *a*-plane sapphire substrate, the in-plane orientation of the ZnO is fixed by the substrate and therefore these domains should not exist. Another difference between these two series can be the ratio of *a/c* lattice constants. The *c* lattice constant is larger for ZnO films deposited at a smaller oxygen partial pressure than for those deposited at higher oxygen partial pressure.



### 3.3.2 Thermal admittance spectroscopy measurements

Thermal admittance spectroscopy (TAS) was done on the ZnO samples for investigation of electrically active defects present in the films. Figure 3.3 shows the dependence of the diode capacitance on the temperature for different frequencies of the HF test signal for E1964. TAS measurements revealed a donor-like defect signature for E1964, commonly observed for ZnO. This is indicated in the figure by the red arrow. The defect commonly labelled as E3 defect has thermal activation energy of about 300meV (It is located 300meV below the conduction band minimum) [21,22]. It is an intrinsic defect in origin arising from oxygen vacancies and 2<sup>nd</sup> ionization level of Zn interstitials. However, similar comprehensive studies couldn't be done for other samples since the high series resistance of the rectifying Schottky diodes hindered the experimental observation of electrically active defects in the samples. But since it is a rather well common defect level and was always present in other ZnO films tested from the same series, it is believed to be present in other investigated samples too. Optical DLTS measurements conducted on ZnO films (not the ones that were under investigation in the presented work) by the semiconductor physics group in the University of Leipzig have revealed that the electrically active defect E3 is not optically active.

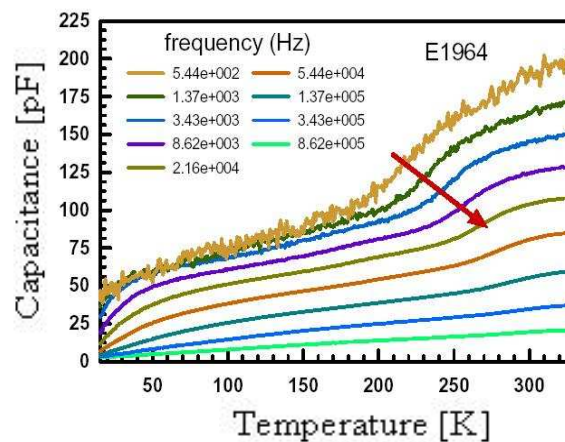


Figure 3.3 Temperature dependence of the diode capacitance for different frequencies of the HF test signal for E1964

## 3.4 Optical properties of ZnO samples

### 3.4.1 Ellipsometric analysis of ZnO films

Spectroscopic ellipsometry was performed on the ZnO films at room temperature. The dielectric function thus obtained allowed detailed insight into the sample properties [23]. For the analysis of the ellipsometric data, a model dielectric function for ZnO suggested by Adachi et al has been used [11]. The anisotropy in ZnO results in uniaxial birefringence in which two different dielectric functions exist for the polarization of light parallel and perpendicular to the *c*-axis. For the current investigation, the dielectric function spectra (shown in the figure 3.4) for light polarized perpendicular to the *c*-axis are considered since only the perpendicular component is of significance in the experimental configuration of the time resolved pump-probe set up.

The model consists of the direct bandgap, lowest conduction band and three valence bands. The dielectric function of ZnO consists of three fundamental contributions from discrete excitons, continuum excitons and free electrons. They are depicted in the figure by the coloured lines. Thermal effects are incorporated in the calculation of the dielectric function through a temperature dependent bandgap and temperature dependent exciton broadening as shown in equation (3.6) [24].

$$E(T) = 3.53062 - 5.4 \times 10^{-4} T, \Gamma(T) = 0.078718831 \cdot \exp(-T / 258) \quad (3.6)$$

$$\epsilon_{2ZnO} = \text{Im} g(\epsilon_{\text{discrete-exciton}} + \epsilon_{\text{continuum-exciton}} + \epsilon_{\text{free-electron}}) \quad (3.7)$$

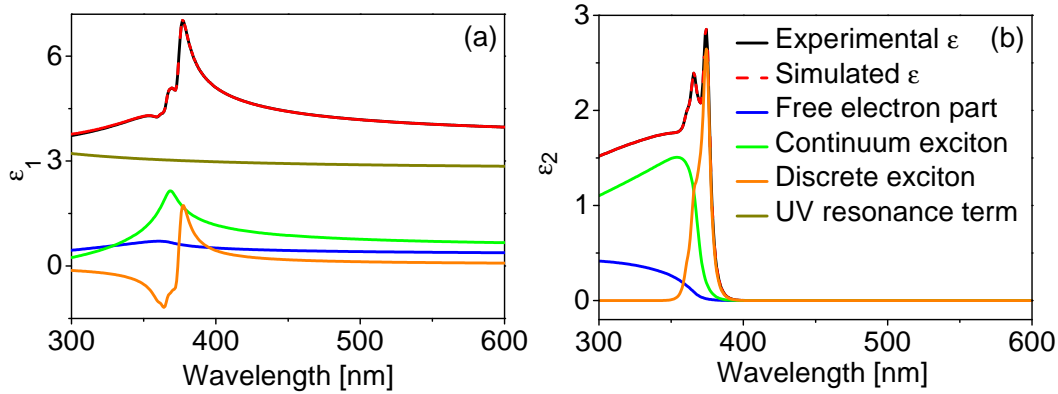


Figure 3.4 Overall and individual contributions to the (a) real ( $\epsilon_1$ ) and (b) imaginary ( $\epsilon_2$ ) parts of the dielectric function of ZnO

Taking the aforementioned three fundamental contributions into account, the overall modelled value of the real part of the dielectric function is found to be higher than the experimental one. In order to match the fit, Adachi et al have used a constant additional term which is assumed to arise from higher lying gaps and core exciton transitions. However, it was found during the analysis in the presented work that a constant term is not sufficient to describe the discrepancy in the fit and that an additional wavelength dependent factor is required.

$$\epsilon_{1ZnO} = \text{Re}(\epsilon_{\text{discrete-exciton}} + \epsilon_{\text{continuum-exciton}} + \epsilon_{\text{free-electron}}) + \epsilon_{1\text{off}} - \frac{A_{\text{pol}} E^2}{E^2 - E_{\text{pol}}^2} \quad (3.8)$$

This discrepancy is dealt by adding two additional terms to the real part of dielectric function; one constant and another having inverse quadratic dependence to the wavelength as shown in equation (3.8). These are the ultraviolet absorption contributions to the refractive index whose resonance is traced deep in the UV at around 167 nm. It should be mentioned that 167 nm is an optimized value yielded during the mathematical modelling of ellipsometric data.

**Discrete exciton contribution:** There are three discrete exciton absorptions at 375nm, 373nm, 366nm formed as a result of transitions from the three valence bands A, B and C respectively. They consist of a series of sharp discrete lines with rapidly decreasing oscillator strength proportional to  $n^{-3}$ . Figure 3.5 plots the individual contribution from all the three excitons. The excitonic absorptions are described by a discrete series of sharp Lorentzian line shapes expressed by equation (3.9) [25]. Here,  $E_{x_{n=1,2,3}}$  is the

$$\mathcal{E}_{discrete-exciton}(\lambda) = \sum_{x=A,B,C} \left[ \frac{1}{1^3} \cdot \frac{A_{nx}}{Ex_{n=1} - E(\lambda) - i\Gamma_{exciton_{n=1}}(\lambda)} + \frac{1}{2^3} \cdot \frac{A_{nx}}{Ex_{n=2} - E(\lambda) - i\Gamma_{exciton_{n=2}}(\lambda)} + \frac{2}{3^3} \cdot \frac{A_{nx}}{Ex_{n=3} - E(\lambda) - i\Gamma_{exciton_{n=2}}(\lambda)} \right] \quad (3.9)$$

discrete exciton energy which is related to the bandgap energy  $E_{ox}$  and the exciton Rydberg energy. Dielectric contributions from  $n=1$  and  $n=2$  exciton states, given by the 1<sup>st</sup> two terms in the expression (3.9), are explicitly introduced.

Figure 3.5(a) shows that the 1<sup>st</sup> and 2<sup>nd</sup> exciton states occur at 375nm and 370nm for exciton-A respectively. The 3<sup>rd</sup> term in equation (3.9) sums up the contribution from  $n \geq 3$  exciton levels and the factor of 2 in its numerator approximates this contribution from all the higher energy excitonic states and exciton-phonon coupling interactions. As an illustration, the spectral variation of  $n=3, 4, 5$  and  $6$  levels are plotted in figure 3.5(b). All of them occur at the same spectral position but only with subsequent diminished amplitudes. This also ascertains the correct summation of all the higher excitonic contributions into the 3<sup>rd</sup> term. Clearly, the transitions corresponding to  $n=2$  and higher states produces a bulge in the low wavelength wing of all the three excitons A, B and C. Among them, the slightly blue shifted discrete exciton-B depicted by the red curve in figure 3.5(a) has the strongest influence. It is evident that the excitonic absorption near the direct band edge of ZnO significantly modifies the optical spectra.

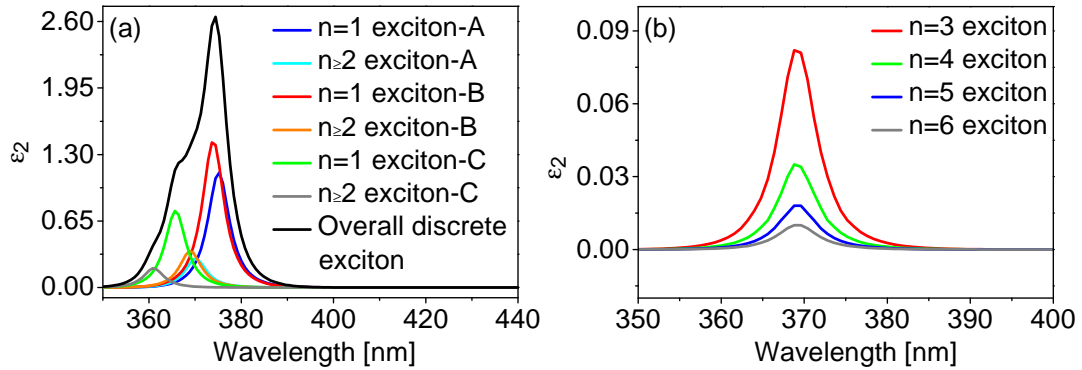


Figure 3.5 (a) Overall and separate contributions to discrete exciton absorption (b) Higher states of the exciton-A

**Continuum exciton and free electron contributions:** As distinct from a discrete exciton where a hole is bound to a single electron by coulomb attraction, a continuum exciton arises from the coupling of a hole in the valence band with a “continuum” of electrons in the conduction band [26,27]. The net charge of a continuum exciton is zero. The line shape of the continuum exciton absorption is given by equation (3.10) where  $\Gamma_x(\lambda)$  is the broadening energy of the bandgap gaps  $E_{ox}$  and  $G_x$  is the exciton Rydberg energy.

$$\mathcal{E}_{continuum-exciton}(\lambda) = \sum_{x=A,B,C} \left[ \frac{A_{cx} \cdot E_{ox}}{4 \cdot G_x \cdot (E(\lambda) + i\Gamma_x(\lambda))^2} \cdot \ln \frac{E_{ox}^2}{E_{ox}^2 - (E(\lambda) + i\Gamma_x(\lambda))^2} \right] \quad (3.10)$$

$$\varepsilon_{free-electron}(\lambda) = \sum_{x=A,B,C} \frac{A_{ox}}{E_{ox}^{3/2}} \cdot \frac{2 - \sqrt{1 + X_{ox}(\lambda)} - \sqrt{1 - X_{ox}(\lambda)}}{X_{ox}^2(\lambda)} \quad (3.11)$$

$$X_{ox}(\lambda) = \frac{E(\lambda) + i\Gamma x}{E_{ox}} \quad (3.12)$$

Figure 3.6(a) clearly shows that continuum exciton-A has the largest contribution followed by continuum exciton-B while continuum exciton C does not contribute to the dielectric function. The spectral evolution of continuum exciton and free electron parts are rather similar. All three free electron contributions along with the overall contribution is plotted in figure 3.6(b). The line shape of free electron part, written in equations (3.11) and (3.12), is characterized by continuous absorption proportional to  $E^{1/2}$ . Free electron-B has the highest contribution to the overall free electron contribution followed by free electron-A and -C.

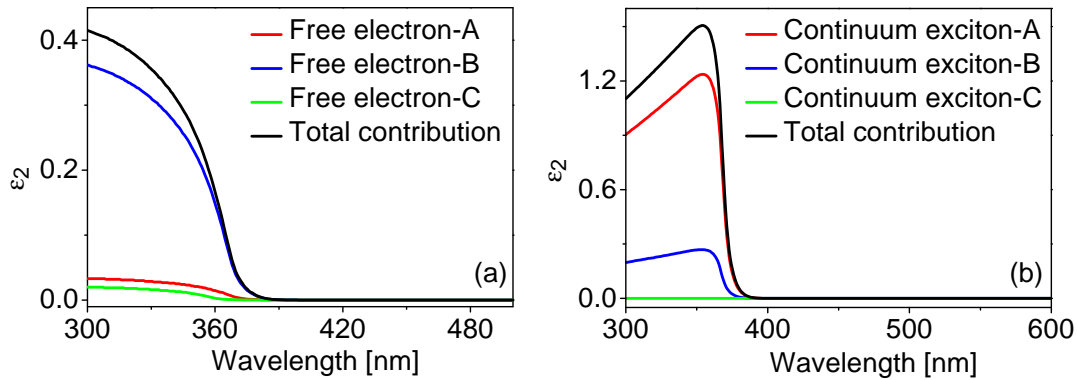


Figure 3.6 Overall and individual contributions to (a) free electron and (b) continuum exciton

### 3.4.1.1 Dielectric functions for different ZnO samples

The dielectric functions determined from ellipsometry for all the ZnO samples are shown in figure 3.7. In E857, the exciton broadening is large and the excitons-A and -B are energetically so close to each other that it is difficult to resolve them. Therefore, during the modelling of ellipsometric data, exciton-B is assigned value 0 in E857 while

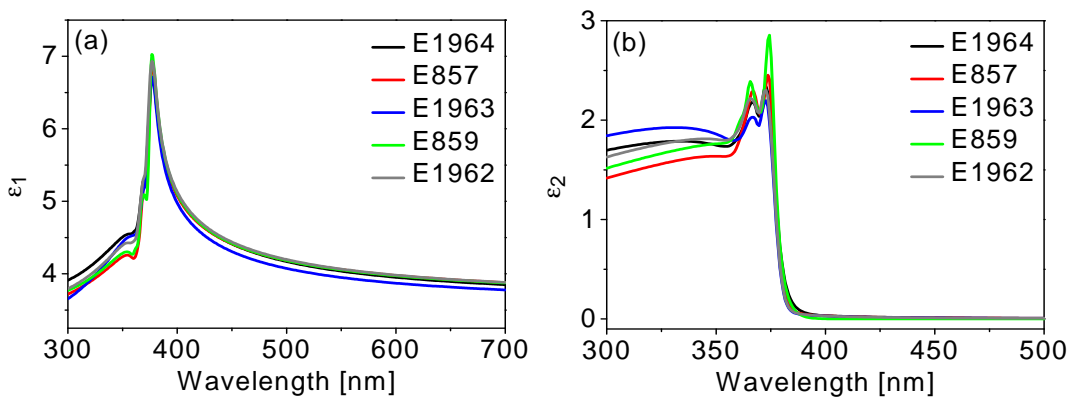


Figure 3.7 (a) Real and (b) imaginary part of the dielectric functions for all ZnO films

the exciton-A contains the total contribution from both. The real part of the dielectric function is very similar for all the ZnO films. In the imaginary part, the region below 375nm exhibits some differences between the samples. It should be noted that the aforementioned is the ground state dielectric function of ZnO which contains information about the valence band (ground state) and all the empty levels namely the conduction band and the exciton states. As already mentioned in sections 3.2.2 and 3.3.2 that the inherent intrinsic defects manifest themselves as donor-like levels within the bandgap in ZnO. However, the ellipsometric measurements done on the samples do not reveal any information about these states. Also, there is slight discrepancy between the experimental and the modelled dielectric function around 375nm.

### 3.4.2 Transmission measurements of ZnO films

#### 3.4.2.1 Transmission spectra of ZnO films

Figure 3.8(a) shows the transmission spectra of E857 and E859 on *c-plane* sapphire substrate while figure 3.8(b) depicts that of E1964, E1963 and E1962 films on *a-plane* sapphire respectively. The pure *c-plane* sapphire is transparent over the entire spectral region of interest. All the ZnO samples exhibit high transmission above 375nm and strong absorption below it. The transmission increases between 300-375nm with decreasing thickness; the highest being for E1964. The thinner the sample the lesser absorbing ZnO it contains, resulting in higher transmission. A small kink observed around the lower end of band edge, most visible for thinner samples, is the exciton contribution in the ZnO films under investigation. There is indication of scattering in the samples as even the pure sapphire exhibits only around 80% transmission.

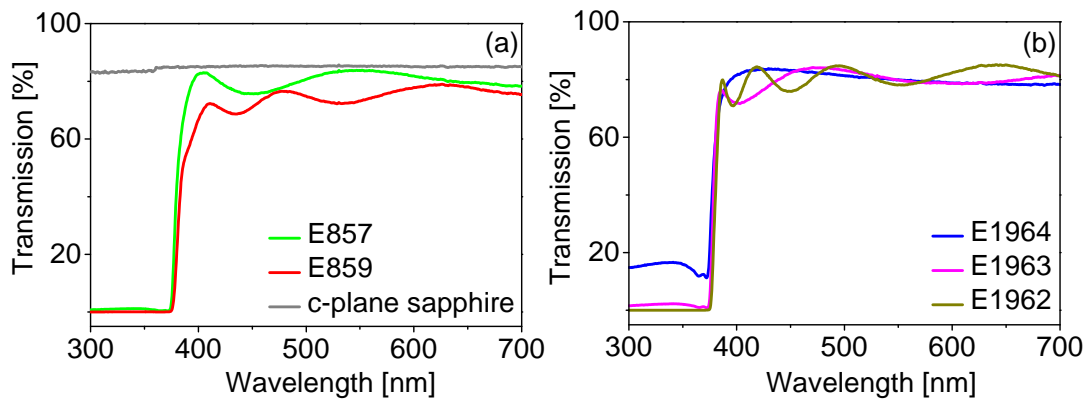


Figure 3.8 Experimental transmission spectra of ZnO films

The oscillations observed between 400-600nm are due to interference in the film. Constructive and destructive interferences take place between the probe light reflected from the top and bottom surfaces of the ZnO layer, which give rise to fringes. The transmission spectrum of the film shows these interference fringes in terms of periodic variations in wavelength, as can be observed between 400-600nm. Below 375nm, the oscillations are strongly damped by the absorption. It is also evident from the figure that the period of oscillations depends on the thickness of the film with the thinnest E1964 sample exhibits one oscillation and the thickest E1962 shows as many as four oscillations. Furthermore, the amplitude of the oscillations is connected to the contrast between the refractive indices of the layer and the substrate.

### 3.4.2.2 Simulation of transmission spectrum of ZnO

In order to calculate transmission changes in the time resolved pump probe spectra, it is crucial to first simulate the transmission spectra of ZnO samples. Knowledge of the exact dielectric function of ZnO determined using ellipsometry enables one to calculate it. Figure 3.9 illustrates a schematic of paths traversed by a ray of light incident on a thin film. The incident light ray L is bifurcated into a reflected ray along AR and a ray refracted through ZnO layer striking the lower interface at B<sub>1</sub>. Since the sample is transparent, a very small fraction of the incident light is reflected as the ray AR at the upper surface. The light which enters the ZnO layer suffers multiple reflections from the front and back surfaces. After even number of passes in the medium, an even smaller fraction emerges as reflected light (rays R<sub>1</sub>, R<sub>2</sub>, R<sub>3</sub>...). Most of the light is transmitted as ray B<sub>1</sub>T<sub>1</sub> during the first pass. The amplitude of the subsequent transmitted rays after reflection from the film's inner surfaces gradually diminishes. These emerging multiple transmitted rays superimpose with one another giving rise to interference fringes [28,29].

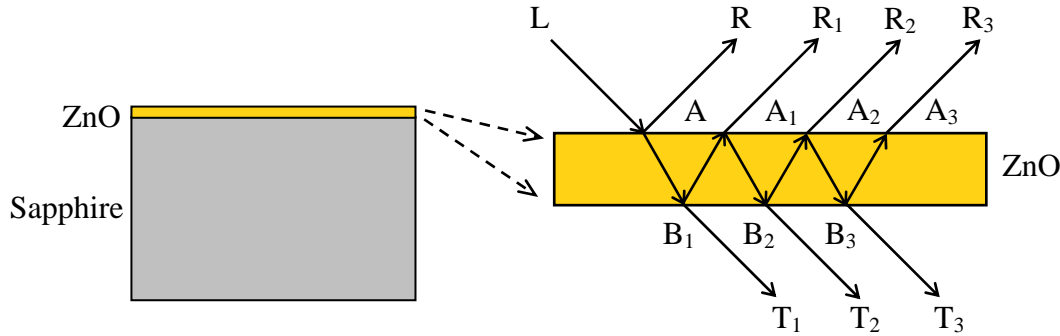


Figure 3.9 Sketch of the ZnO film on sapphire substrate along with the schematic depicting interference phenomena in a thin film

**Mathematical treatment (Transmission mode):** Suppose that a plane wave is incident upon a ZnO film of thickness  $t$  at an oblique incidence  $\theta$  with respect to the normal. The relative phase between the transmitted rays depends on the angle of refraction  $\theta'$  at the upper surface and the refractive index  $n(\lambda)$  by the relation (3.13).

$$\delta(\lambda) = \frac{2\pi n(\lambda)t}{\lambda} \cos \theta', \text{ where } \theta = 0^\circ \quad (3.13)$$

For normal incidence, the cosine term equals unity. Furthermore, during each pass through the ZnO layer, the beam suffers an absorption loss of  $\exp(-\alpha t/2)$ . The total field due to the superposition of  $p$  transmitted rays is given by the expression (3.14). The amplitude of these fringes of multiple beam interference, also known as Fabry-Perot fringes go in geometric progression. Equation (3.15) describes the combined reflectivity  $r(\lambda)$  of front and back interfaces where  $n_{12}$  and  $n_{23}$  are the effective refractive indices at the ZnO-sapphire and air-ZnO interfaces respectively expressed in equation (3.16).

$$E^d(\lambda) = (1-r)e^{i\delta} e^{-\frac{\alpha t}{2}} \left[ 1 + r e^{2i\delta} e^{-\alpha t} + \dots + r^{p-1} e^{2(p-1)i\delta} e^{-(p-1)\alpha t} \right] \quad (3.14)$$

$$r(\lambda) = \left( \frac{n_{12}(\lambda) - 1}{n_{12}(\lambda) + 1} \right) \left( \frac{n_{23}(\lambda) - 1}{n_{23}(\lambda) + 1} \right) \quad (3.15)$$

$$n_{12}(\lambda) = \frac{n_{\text{ZnO}}(\lambda)}{n_{\text{sapphire}}(\lambda)}, \quad n_{23}(\lambda) = \frac{n_{\text{ZnO}}(\lambda)}{n_{\text{air}}} \quad (3.16)$$

The complex summation of this geometric series is given by:

$$E^d(\lambda) = (1-r)e^{i\delta} e^{-\frac{\alpha t}{2}} \left[ \frac{1 - r^p e^{2pi\delta} e^{-\alpha p t}}{1 - r e^{2i\delta} e^{-\alpha t}} \right] \quad (3.17)$$

$$T(\lambda) = E^d(\lambda) \cdot E^d(\lambda)^* \quad (3.18)$$

Following the above treatment, the resultant transmitted intensity is obtained as:

$$T_p(\lambda) = \frac{(1-r)^2 e^{-\alpha t} \left[ \left( 1 - r^p e^{-p\alpha t} \right)^2 + 4r^p e^{-p\alpha t} \sin^2(p\delta) \right]}{\left( 1 - r e^{-\alpha t} \right)^2 + 4r e^{-\alpha t} \sin^2(\delta)} \quad (3.19)$$

In expression (3.19) for transmitted intensity from a thin film, the terms in the denominator and within the square bracket in the numerator can be interpreted as the interferometric contribution while the pre-factor  $e^{-\alpha t}$  represents the pure absorption due to ZnO. It should be mentioned that finite number of transmitted rays are considered for the estimation of transmission. Since taking infinite transmitted rays, i.e. in the limit  $p \rightarrow \infty$ , the expression (3.19) becomes indeterminate. Additionally, after transmission through the ZnO layer, there is a minor loss in the intensity of light due to the back reflectivity from the sapphire substrate. Therefore, in addition to the aforementioned interferometric contribution due to  $p$  rays transmitted through the ZnO layer, reflectivity from sapphire back surface can be explicitly incorporated in the formalism as  $T(\lambda) = T_p(\lambda) - (1 - r_{\text{sapphire}}(\lambda))$  [30]. In a transparent material like sapphire where the absorption coefficient is very small, the extinction coefficient  $\kappa$  is assumed to be negligible in the calculation of this reflectivity.

Using the refractive index as well as the absorption coefficient determined specifically for each ZnO sample using the above formalism, their respective transmission spectra were computed. Figure 3.10 (a) shows one such simulated spectrum along with the experimental one for E859. As mentioned earlier, most of the incident light is transmitted through the first ray, thereafter the subsequent strengths decrease gradually. Analysis of the modelled transmission spectrum showed that after  $p=3$  transmitted rays, there is a very small change in transmission intensity, of the order of  $10^{-3}$ , in the sample. It can be seen in the figure 3.10 (a) that there is no observable difference between the spectrum with 3 transmitted rays and the one with 300 rays.

In figure 3.10(b), the discrepancy in the experimental and simulated spectrum is plotted for the ZnO films. The residual transmission spectra reveal that the model overestimates

the amount of transmission especially around 400nm. This residual absorption can be due to the contributions by defect states shown by the conventional transmission spectra but not by the ellipsometric one. It may include scattering contributions as well. The contribution from defect states would not be accounted in the model dielectric function if they are filled. Also, the presence of a minor oscillatory component indicates that the refractive index of ZnO is not perfectly described by the ellipsometric data. From the enlarged view of the bandedge spectral region in figure 3.10(c), a dip around 380nm for all the films is visible. It is maximum for the thickest E1962 and minimum for E1964. Necessary refinement in the dielectric function of ZnO is required to improve the fit.

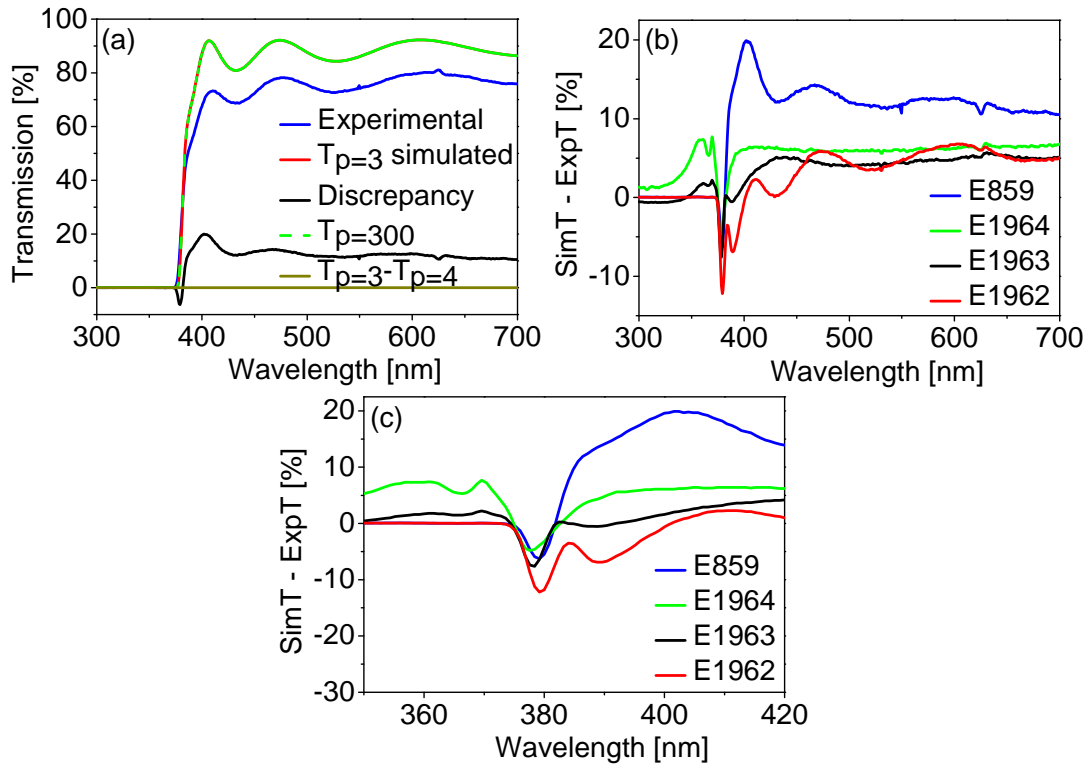


Figure 3.10 (a) Experimental and simulated transmission spectra of E859 (b) and (c) Discrepancy between simulated and experimental transmission spectra of ZnO films

As an annotation, it should be mentioned that the interferometric contribution from the sapphire substrate is not taken into account. Since the thickness of sapphire layer is quite large ( $\sim$  hundreds of  $\mu\text{m}$ ) as compared to the wavelength of the light, the order of resulting fringes is quite high and thereby the resulting oscillations are too narrow to be resolved by the spectrometer. Hence, the interference contribution due to sapphire can be ignored.

### 3.4.3 Microscope images of ZnO films

Figure 3.11 shows microscope images of E857, E859, E1964, E1963 and E1962. The damage at the sample surface caused by exposure to 400nm femtosecond laser pulses can be seen [31]. There is indication of scratches and surface defects in E857, E859 and E1964. In order to characterize the surface of these films in more detail, more sophisticated techniques like atomic force microscopy was used.



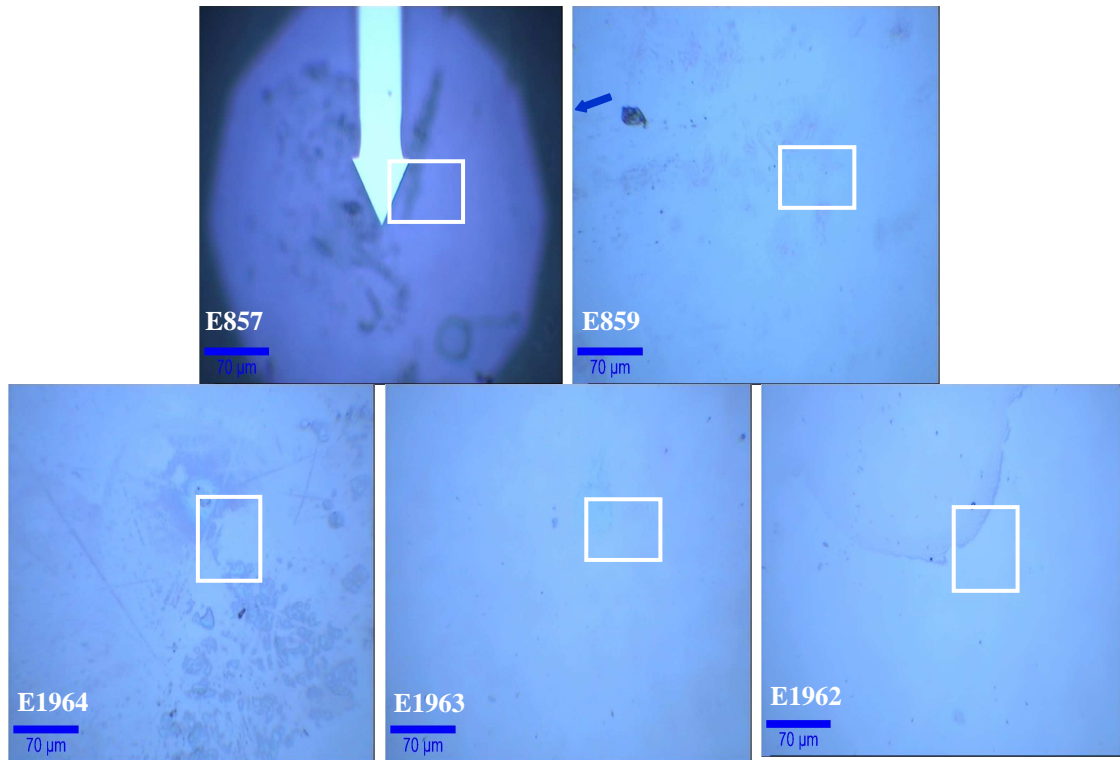


Figure 3.11 Microscope images of the surfaces of E857, E859, E1964, E1963 and E1962

### 3.4.4 Atomic force microscopy on ZnO films

The surface morphology and surface roughness in ZnO samples were investigated using AFM. Figures 3.12 and 3.13 show the AFM images of the areas which are squared in the microscope images all the ZnO samples. The heights of some of the spikes are written on the images. It is visibly clear that the surface of ZnO is not smooth, rather it has considerable roughness [31]. The surface of E1962 is relatively smoother and clean. In case of E859 and E1963, it shows some rod like features, marked with white squares in the AFM images, that seem to be absent in other samples. They may lead to higher scattering in these films. In E1964 and E1963, the horizontal step contrasts are scanning artefacts introduced during AFM. The colour contrast from one end to another end in all the samples is a scanning artefact too. The black step on the left side in E857 is a defect or scratch on the surface.

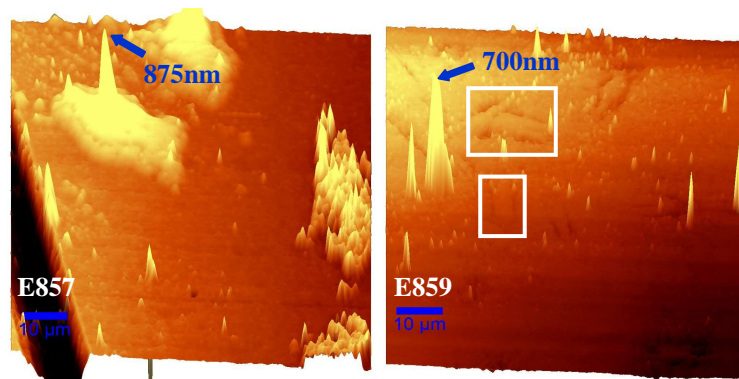


Figure 3.12 AFM images of the surfaces of E857 and E859

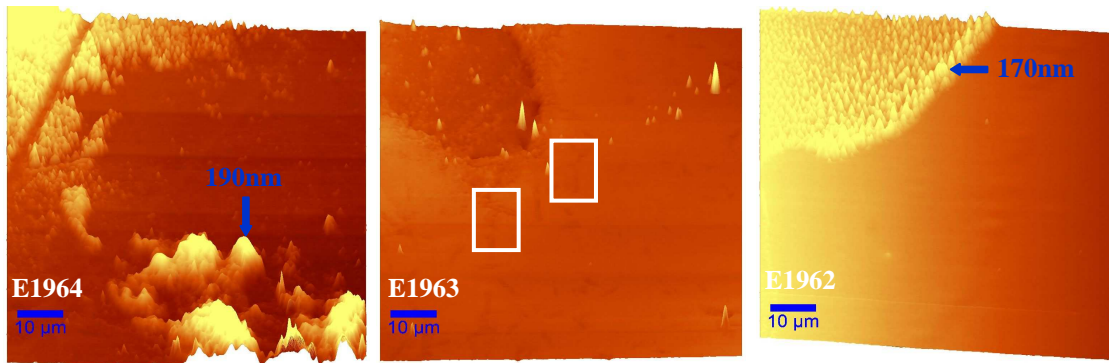


Figure 3.13 AFM images of the surfaces of E1964, E1963 and E1962

The AFM images reveal that the samples are not identical since they differ not only in thickness but in surface morphology too. The thickness given by ellipsometry which is used in the modelling of time resolved spectra is an average one. The thickness is not constant over the entire film due to the considerable surface roughness in them. Hence the ZnO films under investigation do not make a “perfect” interferometer. This is an important revelation which must be kept in mind as it may introduce some discrepancy in tallying the modelled time resolved spectra valid for the perfect interferometer with the experimental spectra for the real “not-perfect” system. Secondly, scattering of the strong pump beam is expected from the surface roughness in these films.

## Chapter 4. Disentanglement of contributions in the time resolved spectra of ZnO films

### 4.1 Model

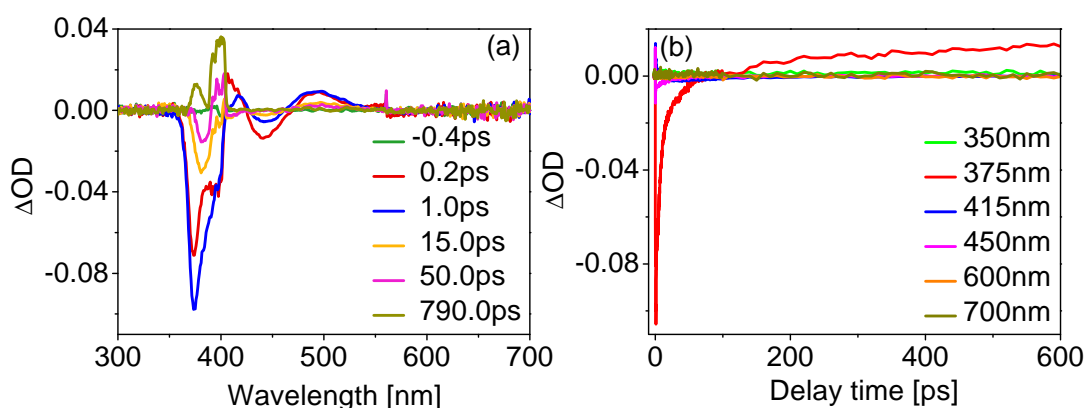


Figure 4.1 Time resolved spectra for E859 (a) Change in optical density as function of wavelength for selected delay times (b) Change in optical density as function of time for selected wavelengths

The femtosecond pump probe experiments generate complex three dimensional data. Figure 4.1 illustrates typical time resolved data for E859 sample. In figure 4.1(a), one can observe changes in optical density at various spectral positions between 300-700nm. By mere visual analysis of the spectrum, it is impossible to understand the physical background behind these features. The variation of each of these features with time adds further complexity in the analysis and its interpretation. Hence, in order to extricate information about various physical processes from it and understand the carrier dynamics in ZnO films, a careful and thorough theoretical analysis of the time resolved pump probe data is required. Also, it is known from the preceding chapter (refer to figure (3.4)) that the spectral positions of different contributions in the dielectric function of ZnO overlap with each other. This too strongly indicates that the time resolved dynamics in ZnO is expected to have a complex overlap from these contributions. Hence, a model must be built using which different contributions to the time resolved spectra can be analysed to gain knowledge about the dynamical processes in ZnO upon excitation with strong femtosecond pulse.

Based on the known dielectric function of ZnO, a model is developed to simulate the time dependent spectral changes. Taking the absorption coefficient and the refractive index of the sample into account, the ground state transmission of the sample (equation (3.19) of chapter 3) before the pump irradiation is calculated. For convenience, it has been rewritten as equation (4.1). Upon excitation the pump pulse modifies the dielectric function of ZnO. Consequently, the altered absorption coefficient and refractive index leads to changes in the transmission from the sample. Therefore, a variation of the parameters of the known dielectric function, resulting in changes in absorption and refractive index, is used to calculate the modified transmission after the excitation and hence the corresponding change in optical density at each spectral position.

$$T(\varepsilon(\lambda)) = \frac{(1-r)^2 e^{-\alpha} \left[ \left(1-r^p e^{-p\alpha}\right)^2 + 4r^p e^{-p\alpha} \sin^2(p\delta) \right]}{\left(1-r e^{-\alpha}\right)^2 + 4r e^{-\alpha} \sin^2(\delta)} \quad (4.1)$$

$$\Delta OD(\varepsilon(\lambda)) = \log \left( \frac{T_{bp}(\lambda)}{T_{ap}(\lambda)} \right) \quad (4.2)$$

The change in optical density ( $\Delta OD(\lambda)$ ) is defined as the logarithm of the ratio of unchanged to the changed transmission before ( $T_{bp}(\lambda)$ ) and after ( $T_{ap}(\lambda)$ ) the pump excitation respectively. Levenberg Marquardt optimization routine was implemented to optimize the parameters in dielectric function to fit the experimental time resolved spectrum. It is discussed briefly in the following sub-section. The above formalism is implemented to simulate the spectral changes in optical density for every measured delay time. The spectral analysis of transmission changes gives signature of the states created by the pump pulse while its temporal analysis would yield the dynamics of the transitions. In this way, the theoretical model based on the dielectric function can thus render detailed insights into the ultrafast dynamics of individual processes in ZnO films.

It should be emphasized that the dielectric function of ZnO contains all the ground state contributions. However, it is known from chapter 3 that the modelled dielectric function is not able to completely describe the defects in the system. As a result, the dielectric function based formalism to simulate the time resolved spectra would not be able to account for contributions from defect states. Therefore if present, these contributions must be additionally incorporated in the model. Moreover, under strong excitation there are many effects one might observe in the time resolved dynamics such as early time coherent interactions like AC Stark effect, bandgap renormalisation [1,2]. Since all them are induced processes, the above mentioned ellipsometric formalism cannot explain them. Since these transitions initiating from excited levels or levels which are initially filled in the unexcited state are not inherently included in it, they must be additionally incorporated.

$$sim\Delta OD(\lambda) = \Delta OD(\varepsilon(\lambda)) + \frac{A}{w\sqrt{\frac{\pi}{2}}} e^{-2\left(\frac{\lambda-\lambda_c}{w}\right)^2} \quad (4.3)$$

Therefore, all the additional contributions can be formally incorporated into the model, should this be necessary, by suitably introducing a Gaussian or Lorentzian curve at the corresponding spectral position  $\lambda_c$ . In the second term of equation (4.3),  $A$  and  $w$  indicate the amplitude and width of a normalised Gaussian curve. In this way, the model is equipped to explain all kinds of processes in case they appear in the time resolved spectra of ZnO films.

### 4.1.1 Implementation of Levenberg Marquardt optimization routine

Levenberg Marquardt routine is a nonlinear least square optimization procedure where a non-linear model function is fitted to measured data [3]. It determines optimum values of the parameters of a model function (presented in equation (4.3) in the current case) so as to best fit the experimental time resolved spectrum. These simulations were efficiently performed in Matlab. For a single time resolved spectrum, the data set consists of discrete empirical data pairs ( $exp\Delta OD_i, \lambda_i$ ). The model function,  $sim\Delta OD(V, \lambda_i)$ , is a nonlinear function of the parameters of the dielectric function where  $V$  is a vector of initial estimates of the parameters to be optimized. The step size is kept to be 0.8nm which is in accord with the resolution of the diode lines in the spectrometer. The residual is defined as difference between the experimentally measured value and that estimated by the model. By varying the chosen set of parameters of the dielectric function,  $S(V)$ , the residuals squared at each wavelength position and summed over all wavelength points is minimized. It is illustrated in equation (4.4).

$$S(V) = \sum_{i=1}^n (\exp\Delta OD(\lambda_i) - sim\Delta OD(V, \lambda_i))^2 \quad (4.4)$$

To start the minimization, an initial guess for the chosen set of parameters of the dielectric function to be varied is provided while the rest of the parameters are kept fixed. Levenberg Marquardt optimization routine requires an iterative procedure to establish a direction of search at each major iteration. All the chosen parameters are varied simultaneously in the routine until the simulated spectrum matches with the experimental spectrum for a particular delay time. The iterative process is terminated when the convergence criterion is satisfied and thus the optimized values which best describes the experimental spectrum is obtained. Likewise, this treatment is repeatedly done to the pump probe spectra of all delay times. It should be noted that the same set of chosen parameters are consistently varied for all the subsequent delay times.

The Levenberg Marquardt optimization is robust as well as very fast and finds a solution even if it starts far off the final minimum. It must be added though, that the space of parameters of the model function may have many local valleys. Therefore, starting the optimization with an educated guess of the initial estimates can be critical. During excitation by the pump pulse, the parameters start changing from their initial values to modify the  $\Delta OD(\lambda)$ . Maximum change of parameters occurs for early delay times after which they subsequently decay back to their original values. Therefore, the optimized values of parameters generated for a differential optical density spectrum at a delay time is fed as the initial estimate for the next successive delay time.

## 4.2 Implications of different dielectric components on simulated difference optical density spectrum

In the simplest implementation of the model, the effect of different parameters of the dielectric function of E859 on the simulated difference optical density spectra was studied extensively. The following subsections describe them in detail.

### 4.2.1 Exciton bleaching

Reducing the amplitude of the exciton absorption results in transmission increase in the differential optical density spectrum. Figure 4.2(a) shows the simulated spectrum ( $\text{sim}\Delta\text{OD}(\lambda)$ ) where the amplitude of the discrete exciton-A is reduced by 5%. It is expressed as Lorentzian line with a FWHM of  $\sim 8.43\text{nm}$ . In addition to the main bleaching peak at 375nm, minor oscillations can be traced above 390nm, their amplitude being very small on the order of  $\sim 10^{-3}$ . Figure 4.2(b) depicts transmission increases for  $n=1$  and  $n \geq 2$  discrete exciton-A levels at 375nm and 366nm respectively. Both the contributions are equally populated by reducing each of their amplitude by 5%. Transmission increase due to  $n \geq 2$  exciton states produces a bulge in the left wing of the overall exciton-A contribution. Changing the amplitudes of excitons-B and -C produce similar results at 373nm and 366nm respectively.

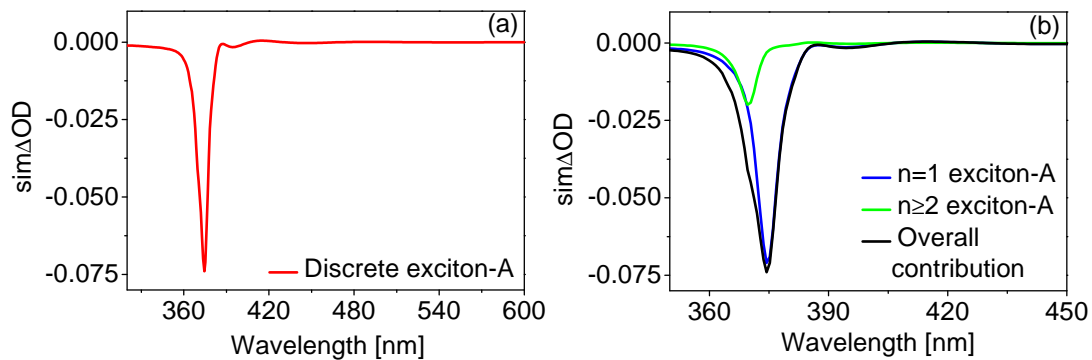


Figure 4.2 (a) Transmission increase at 375nm due to discrete exciton-A (b) Individual contributions from  $n=1$  and  $n \geq 2$  levels to the overall exciton-A bleaching

By reducing the amplitude of exciton-A by 2, 5, 10, 15 and 20%, the exciton bleaching consequently increases. As evident from figure 4.3(a), a 10% decrease in the amplitude of exciton-A results in a large change in optical density of  $\sim -0.147$ . In spite of the gradual increase in peak  $\Delta\text{OD}$ , the FWHM of exciton bleaching remains constant. The left wing of exciton bleaching spreads out as far as 350nm in the ultraviolet region for larger variation of exciton-A. The centre wavelength remains stable at 375nm. Additionally, the effect of varying the linewidth of the exciton along with the amplitude is illustrated in figure 4.3(b). In the expression for exciton broadening in equation (3.6), the constant term placed before the exponential term is varied. The amplitude of exciton-A is fixed to 95% of the original value while the constant term is decreased by 1%, 2% and increased by 2% respectively.

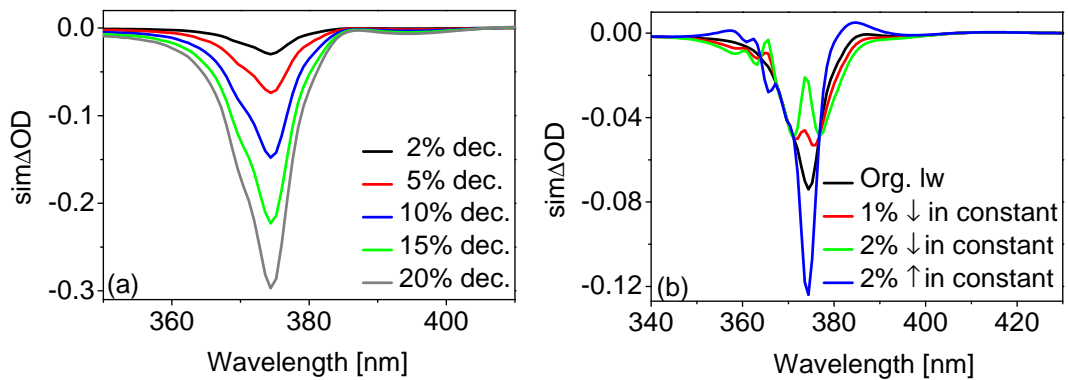


Figure 4.3 (a) Transmission increases due to decrease in the amplitude of discrete exciton-A by various amounts (b) Effect of increasing the linewidth of exciton-A

The amplitude of exciton bleaching diminishes as the constant term in the linewidth is decreased. The exciton peak splits due to the distortion in the centre of the peak. The right shoulder of the bleaching peak broadens while there is a complex amplitude variation in the left one. Upon increasing the constant term by 2%, the overall bleaching amplitude increases along with distortion in its left wing.

## 4.2.2 Modulations

A number of parameters in the dielectric function of ZnO generate oscillatory behaviour between 400-600nm in the differential optical density spectrum. These parameters are  $A_{pol}$ ,  $E_{pol}$ , the continuum excitons-A and B and the free electrons contributions A, B, C. Figure 4.4(a) depicts the oscillatory behaviour produced upon reducing the amplitude of continuum exciton-A by 5%. The strength of the modulations weakens towards the red side of the spectrum. Varying the amplitude of the continuum exciton-A in the opposite direction, i.e. increasing it by 5%, results in complete reversal of the modulations. This is illustrated in figure 4.4(b).

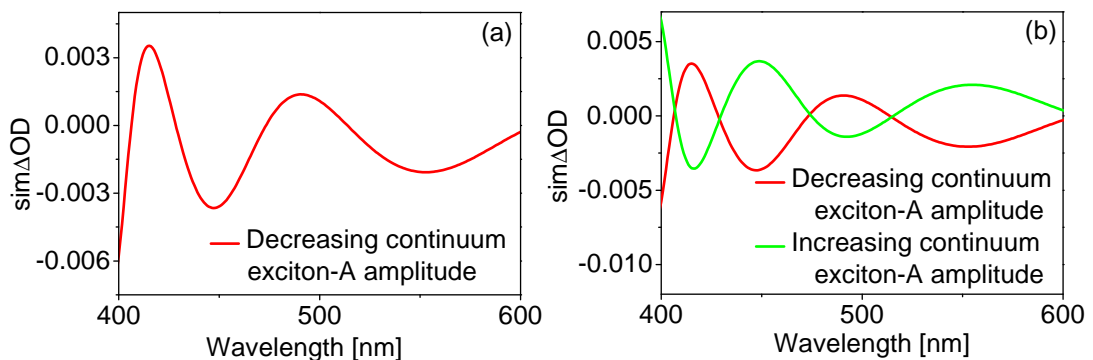


Figure 4.4 (a) Oscillatory behaviour due to decrease in the amplitude of continuum exciton-A (b) Comparison of oscillatory behaviour due to increase and decrease in continuum exciton-A amplitude by equal amounts

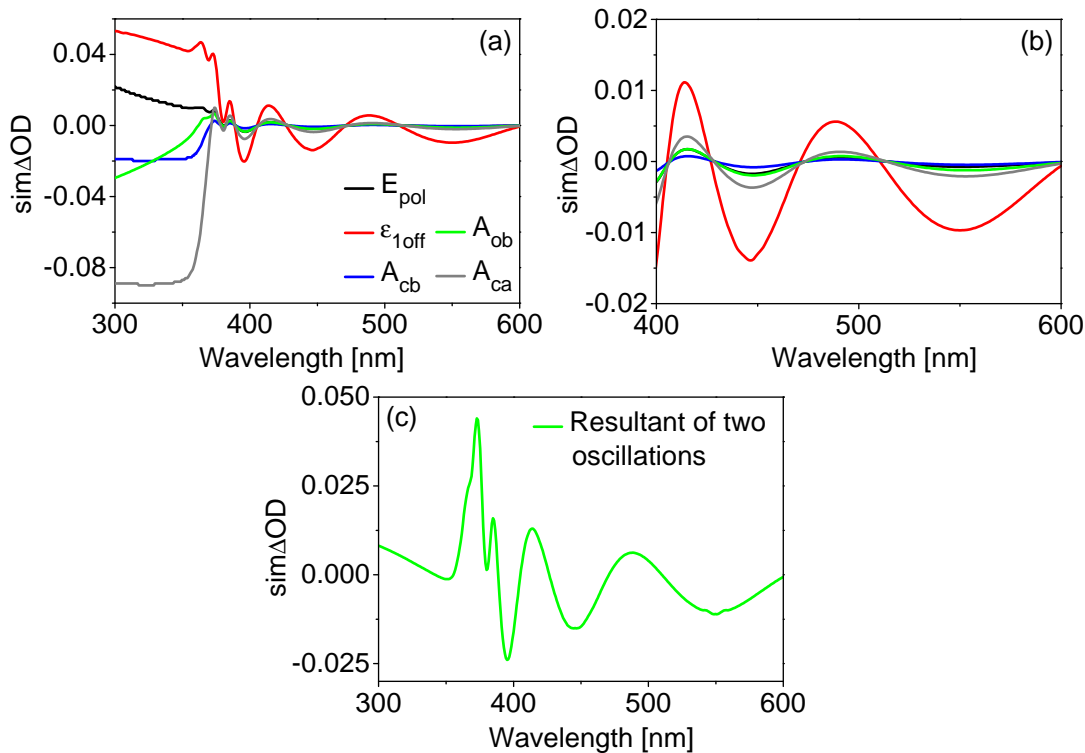


Figure 4.5 Change in optical density spectra due to various parameters in the dielectric function that result in oscillatory behaviour between (a) 300-600nm and (b) 400-600nm (c) Change in optical density as a result of sum of combined variation of  $A_{ca}$  and  $\epsilon_{1off}$

Different dielectric parameters that generate oscillatory behaviour between 400-600nm can be studied in detail from figure 4.5(a) and (b). All the parameters are varied by 5%. It is clearly evident that the parameters do not contribute equally to the differential optical density in the entire spectral range of interest. Moreover, some parameters produce positive  $\Delta OD$  and some negative  $\Delta OD$  in the ultraviolet region.  $\epsilon_{1off}$  produces the strongest modulations in the visible region as well as a considerably high positive amplitude in the UV region. On the other hand, continuum exciton-A yields smaller modulations but shows the highest amplitude variation in the UV region.  $A_{pol}$ ,  $E_{pol}$ , continuum exciton B and free electron B produce relatively much smaller modulations. Free electron-A and C, not shown in the graph, give even minor contributions. Additionally, it can be deduced from a qualitative analysis of figure 4.5(b) that a configuration can be achieved by carefully choosing a combination of two or more parameters such that they cancel each other's effect in the UV while adding up their oscillatory contributions between 400-600nm. As an illustration, figure 4.5(c) shows such a simulated spectrum where a combination of continuum exciton-A and  $\epsilon_{1off}$  are selected.  $A_{ca}$  is reduced by 2.5% while  $\epsilon_{1off}$  is decreased by 5%. Their individual contributions add up between 400-600nm and counteract in the UV region to keep the  $\Delta OD$  to minimum. It can be seen that this configuration also produces a complex behaviour between 340-390nm. Hence, a combination of strongest parameters that yield the lowest sum of the residuals in the entire spectral range of interest ought to be the fundamental criterion for the optimal choice of parameters in the mathematical description to generate such modulations.



### 4.2.3 Bandgap variation

Varying the bandgaps A, B and C introduced by 5K increase in temperature according to equation (3.6) produces strong complex variation at the bandedges of all three bands. Figure 4.6 illustrates this effect on the spectral change in optical density.

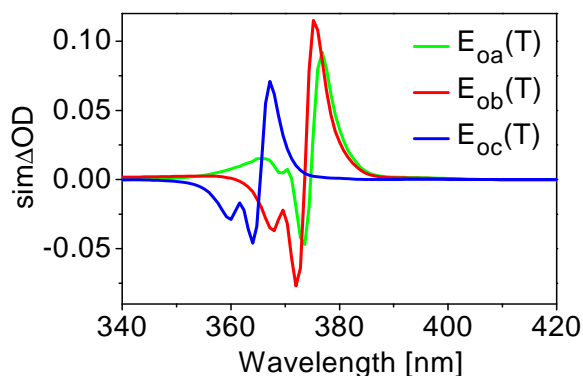


Figure 4.6 Effect of changing the bandgaps through 5K increase in temperature on the change in optical density spectra

### 4.3 Confidence tests of the optimization routine

A number of self-consistent checks were done to confirm the integrity of the complete optimization routine which is implemented in the model developed to simulate the time resolved spectral changes in transmission. Systematic model simulations were performed to evaluate the reliability of the optimization routine. A set of optimized parameters was obtained by fitting a curve to an experimental pump-probe spectrum. In the next step, this simulated spectrum with the known actual values of parameters was fed in the routine as a pseudo-experimental spectrum to be optimized. The motivation behind this procedure was to check that when the exact values of the parameters of an input curve are known, how correctly the routine converges the optimized values to the original ones. Figure 4.7 shows the results of modelling of the simulated spectrum and the difference between both the spectra is plotted in the inset graph. The curves match perfectly, confirming that the optimization routine indeed converge the varying values

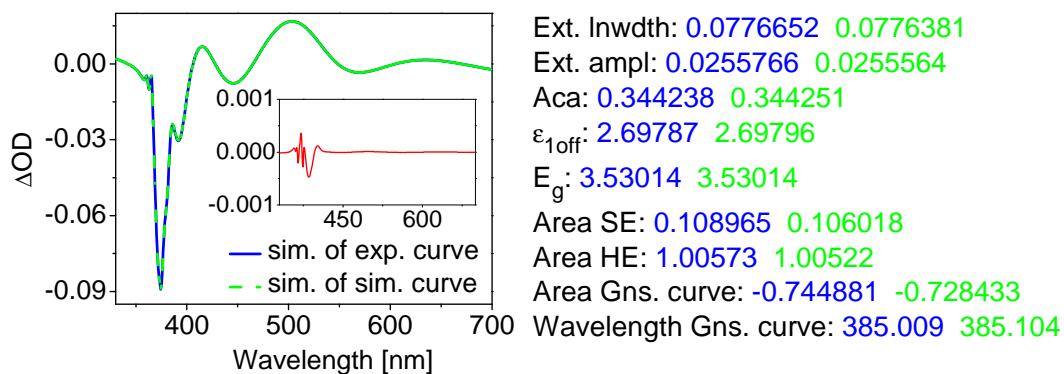


Figure 4.7 Pseudo-experimental (simulated) spectrum and its corresponding simulated fit. The optimum values of the varying parameters for both curves are written as well.

of the parameters to the actual ones. The slight variation around 400nm in the difference spectrum is of the order of  $10^{-4}$ , which is beyond the resolution of the spectrometers used in measuring the pump probe data. Additionally, for comparison, the original values of parameters as well as that yielded after optimization are written in the right column.

As the next step to determine the accuracy of the fitting procedure, the range of variation of the optimized values was studied by inputting different initial estimates for the same parameters. The fluctuation in the resulting values was in the range of less than 3%, which defines the accuracy of the optimization. Additionally, in order to ascertain the correctness of the large and complex formulation of the developed model with the infixed optimization procedure, the best fit parameters given by the routine were fed in another simpler program without any optimization routine (in Mathcad) to calculate the simulated  $\Delta OD(\lambda)$ . It produced the exact spectrum as supplied by the optimization routine. This further confirmed the correct functioning of the formulation.

#### 4.4 Simulation of time resolved spectra: Illustrations

The experimental time dependent transmission changes in ZnO films were modelled using the Levenberg Marquardt optimization procedure implemented on the above described model. In this section, few simulations of the experimental time resolved spectra of ZnO films would be shown as illustrations. Figure 4.8(a) depicts the experimental and it corresponding fitted spectra along with individual contributions at 0.4ps for time resolved measurements done on E859 at a pump energy of 56 $\mu$ J.

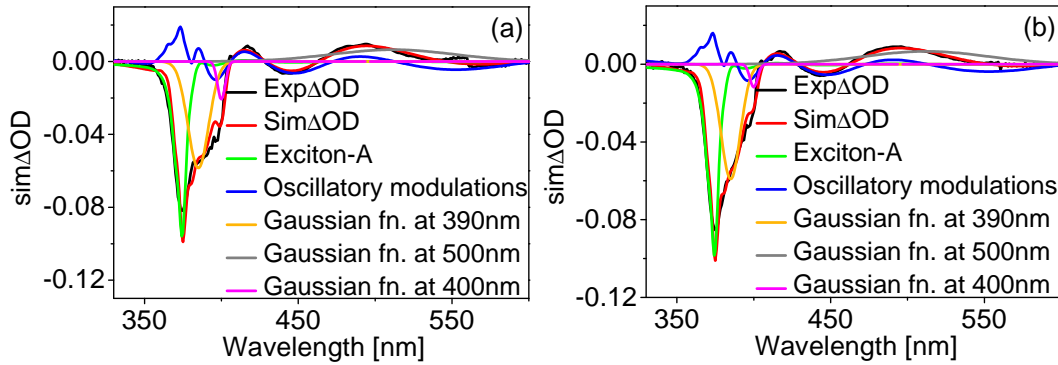


Figure 4.8 Experimental and simulated spectra for E859 at (a) 0.4ps (b) 1.2ps

The transmission increase at 375nm is fitted by varying the amplitude and linewidth of discrete exciton-A. To describe the oscillatory component between 400-600nm, a combination of continuum exciton  $A_{ca}$  and constant real term  $\epsilon_{1off}$  is used. The refractive index modulations fit better to the first oscillation at 405nm. However, there still remains an additional positive  $\Delta OD$  around 500nm which these oscillations cannot account for. In order to incorporate this residual contribution into the mathematical

$$sim\Delta OD(\lambda) = \Delta OD(\epsilon(\lambda)) + \frac{A_1}{w_1 \sqrt{\frac{\pi}{2}}} e^{-2 \left( \frac{\lambda - \lambda_{c500}}{w_1} \right)^2} + \frac{A_2}{w_2 \sqrt{\frac{\pi}{2}}} e^{-2 \left( \frac{\lambda - \lambda_{c390}}{w_2} \right)^2} \quad (4.5)$$

framework, an additional Gaussian curve is introduced at  $\sim 500\text{nm}$  (middle term in equation (4.5)). It is clear from the analysis done in section 4.2 regarding the manifestation of various parameters of the dielectric function in the simulated change in optical density spectrum that none of them can describe the experimentally observed transmission increase at  $390\text{nm}$ . It is an induced contribution and therefore, a second Gaussian curve is introduced at the same spectral position, as shown in equation (4.5). The widths as well as amplitudes of both the Gaussian curves centred at  $390\text{nm}$  and  $500\text{nm}$  were varied. In a similar way, a third Gaussian curve is included at  $400\text{nm}$ . The simulated spectra agree with the experimental time resolved spectra with excellent accuracy. The sum of residuals squared at each wavelength position is of the order of  $10^{-3}$ .

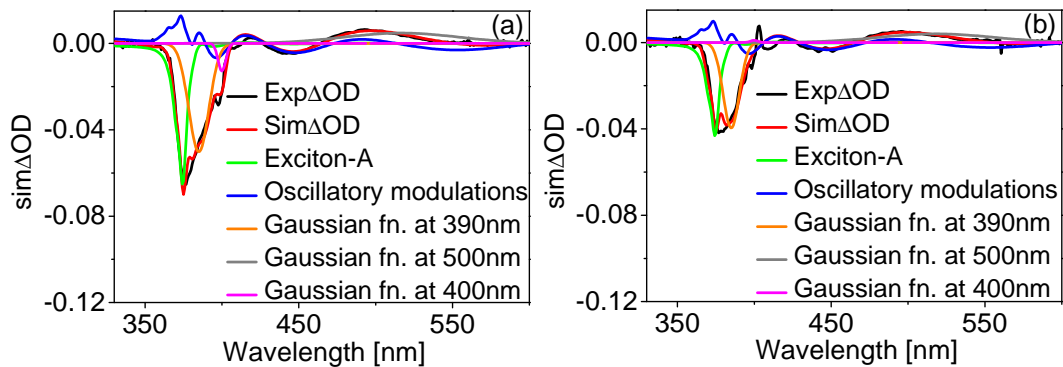


Figure 4.9 Experimental and simulated spectra for E859 at (a) 3.8ps (b) 8.1ps

Due to the complexity of the various contributions, a single spectrum is not a sufficient criterion, rather the entire time sequence must be analysed. Only those spectral components which have a reasonable time evolution can be included in the self-consistent picture. Figure 4.8(b), 4.9(a) and (b) show fitted spectra with corresponding contributions at 1.2ps, 3.8ps and 8.1ps for the same measurement on E859. At 3.8ps, the additional broad absorption increase around  $500\text{nm}$  reduces in amplitude. The simulation for this delay time reveals larger and broader contribution at  $390\text{nm}$  shown by grey Gaussian curve while the transmission increase at  $375\text{nm}$  due to discrete exciton-A is narrow. In an attempt to minimize the discrepancy between the experimental and estimated values in the ultraviolet region, the optimization routine apparently underestimates the oscillations.

From the above illustrations of the simulated spectral changes using the aforementioned model, it is shown that it can successfully account for the various spectral features observed in the time resolved data of ZnO films. The known contributions from the dielectric function cannot explain all features observed in the transient spectra and further non-equilibrium components are required which are incorporated by suitable Gaussian functions. In the ensuing step, the real physical origin of all the different contributions including the empirically included unknown components of the simulated spectra, in tandem with their time evolution must be carefully analysed to understand the charge carrier dynamics in ZnO.



## **Chapter 5. Time resolved dynamics in ZnO films**

### **5.1 Introduction**

The charge carrier dynamics in semiconductor films are strongly governed by intrinsic as well as extrinsic properties. The intrinsic parameters of the ZnO films under investigation, essentially contained in its static dielectric function, have been extensively studied in chapter 3. It has been shown there that the exciton contribution dominates the dielectric function of ZnO and significantly modifies the optical spectrum especially around the band edge. Of utmost importance at this juncture is the question that under excitation by strong femtosecond laser pulses, which fundamental components of the dynamic dielectric function play a significant role in the charge carrier dynamics in ZnO [1,2]. Furthermore, it is known from the literature about the presence of defects in ZnO which create donor like states within the bandgap, described in chapter 3. Additionally, it has been indicated in section 3.4.2 of chapter 3 that the ZnO films contain defect levels within the bandgap that give rise to additional absorption across a wide spectral range between 375-700nm and especially around the band edge. This conjecture leads to another intriguing aspect that whether these defect states manifest themselves in the ultrafast carrier dynamics in ZnO. The answer would reveal their exact role in the carrier dynamics in ZnO and also establish more conclusively their presence in order to understand the underlying background behind the discrepancy between the experimental and modelled transmission spectra. In order to elucidate all these facts, the ultrafast charge carrier dynamics in ZnO films were investigated by performing femtosecond pump probe transmission spectroscopy with 400nm as the excitation pulse. All the measurements were performed at room temperature. The experimental time resolved pump-probe results for E859 are reported in section 5.2. The simulated time evolution of different contributions obtained using the model developed in the preceding chapter are presented next. The underlying physical processes in the time resolved spectra are identified and a schematic of the band picture illustrating fundamental relaxation mechanisms is proposed. An elaborate quantitative as well as qualitative analysis to understand these contributions is performed. A summary of key points is presented at the end of the section.

A critical parameter which significantly governs the carrier dynamics is the wavelength of excitation. Exciting the system with different wavelengths below the bandgap may alter the excitation mechanisms as well as the subsequent relaxation pathways. Therefore, excitation-wavelength dependent time-resolved experiments were

performed to explore different mechanisms in the carrier dynamics of ZnO films. This study was driven by the fact that the time resolved measurements performed with 400nm pulse as the excitation wavelength is far off from the resonance in ZnO at ~365nm. Hence apart from 400nm pump, experiments were carried out with two other excitation wavelengths of 409nm and 391nm, on either side of 400nm. Energy states within the bandgap can be directly accessed by pumping the films even farther off the resonance with 409nm pulse. In this case, excitons would definitely be indirectly excited. In contrast, excitation at 391nm was chosen with the intent of directly exciting the far red wing of the excitons. These experiments would also serve as a test if 18nm difference in excitation wavelengths is sufficient to significantly alter the relaxation mechanisms in ZnO. In section 5.3, the results of excitation wavelength dependent time resolved measurements are reported. A detailed analysis of modelled results is performed to gain insight on the different decay channels and understand how these interactions affect the lifetime of various processes. The section ends with a summary of the key findings from these experiments.

A yet another crucial aspect to further the understanding about the nature of the fundamental relaxation mechanisms in ZnO deals with the amount of energy put into the system. If the excitation is weak, the absorption and refractive index modulations are small. On the other hand, at high excitation intensities saturation effects play a pivotal role in the carrier dynamics [15,1]. Secondly, the exciton density is dependent on the number of carriers excited from valence band and hence exciton-related effects will be strongly influenced by the excitation intensity. In the light of these arguments, excitation energy dependent time resolved measurements were performed to investigate its influence on the carrier dynamics in the ZnO films. The 400nm pump pulse was varied in energy from 7.5 $\mu$ J to 56 $\mu$ J. The results of the excitation energy dependent measurements are presented in section 5.4 along with the simulations that reveal how the pump energy influences the spectral variation of different processes and their corresponding lifetimes. At the end of the section, the important revelations from this analysis are summarized.

The time resolved carrier dynamics for different ZnO films were studied. A significant aspect is to understand the role of film thickness on the carrier dynamics of the ZnO films. In the time resolved differential transmission spectra of ZnO presented as example in section 4.4, an oscillatory component between 400-600nm is clearly evident. It is known from chapter 3 that the conventional transmission spectrum of ZnO exhibits oscillations due to interference in the film. The interference effect is strongly influenced by the thickness of the film. These arguments bespeak that the thickness of the film may have a strong bearing on the time resolved dynamics in ZnO. For this reason, time resolved transmission measurements were performed on ZnO films with different thicknesses. In addition, this investigation would also elucidate information about the optical processes that stem from bulk like behaviour as well as surface contributions, if present. In section 5.5, the results of the pump-probe experiments for different samples are presented. Moreover, the sample analysis presented in chapter 3 revealed that the investigated ZnO films are not perfectly identical and that they differ not only in thickness but also in structural properties and surface morphology. These measurements would also reveal that whether these differences have a bearing on the time resolved spectra from these ZnO films. The key findings from the analysis are presented at the end of the section.

## 5.2 Time resolved results of ZnO films

### 5.2.1 Experimental results

#### 5.2.1.1 Spectral variation

Time resolved transmission measurements were performed on E859 film grown on *c-plane* sapphire with 400nm excitation pulse with energy of 26 $\mu$ J. Figures 5.1 and 5.2 show the experimental time resolved spectra for delay times upto 600ps respectively. The change in optical density ( $\Delta OD(\lambda)$ ), which is a measure of change in transmittance of the sample, is plotted as a function of wavelength for different times. At this point, it would be useful to restate that  $\Delta OD(\lambda)$  represents the change in transmission of the probe spectrum upon excitation. Hence, negative  $\Delta OD(\lambda)$  indicates transmission increase and positive  $\Delta OD(\lambda)$  indicates vice-versa. At very early delay times starting, a strong bleaching around 375 nm is observed along with a broad positive feature, which seems to be a combined effect of oscillatory behaviour between 400-600nm and an absorption increase centred around 500nm. The absorption increase between 430-560nm rises and decays very rapidly. It lasts upto 0.2ps, after that only an oscillatory component remains which too diminishes gradually after 2ps. The 375nm contribution increases in amplitude peaking at around 0.8ps. It is accompanied by a spectral broadening that extends as far as 347nm on the blue side. Thereafter, though the amplitude diminishes but the broadening persists until  $\sim$  1ps. It can be seen clearly from figure 5.1(b) that a prominent red shifted structured shoulder at  $\sim$ 387nm starts to develop from 0ps onwards. The distinct peak can clearly be observed until 0.3ps. After 0.5ps, this feature doesn't remain distinct but smears out with the 375nm peak. Furthermore, it is evident that the spectral features are not stable in their positions with time. It can be seen in figure 5.2(a) that the amplitude as well as width of 375nm peak reduces after 1ps. This transmission increase at 375nm along with its red shifted shoulder at  $\sim$ 387nm is observed for short times up to  $\sim$ 20ps and  $\sim$ 200ps respectively. From 100ps onwards in figure 5.2(b), an additional absorption increase centred at 374nm is traced which rises and red shifts up to 600ps and beyond. At 400nm, a structured positive feature develops from 5ps onwards which prevails even at longer delay times upto 590ps and beyond. This feature is due to the scattering of the pump wavelength in the sample.

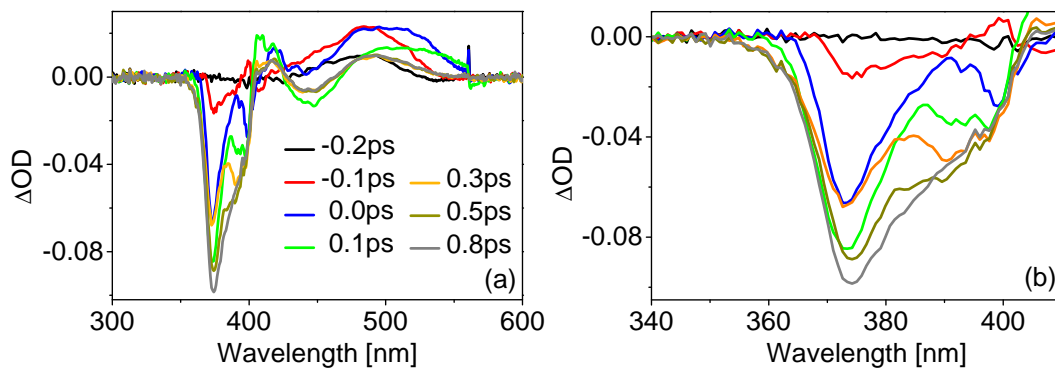


Figure 5.1 Time resolved spectra of E859 for times up to 1ps

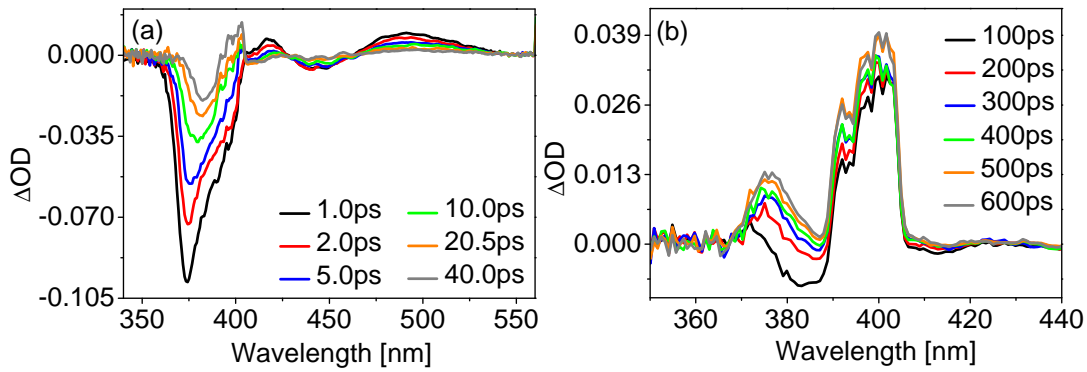


Figure 5.2 Time resolved spectra of E859 for times upto 40ps and 600ps

### 5.2.1.2 Temporal evolution

In figure 5.3(a) and (b), the change in optical density spectra as a function of delay times upto 600ps and 10ps respectively are plotted for selected wavelengths. The time evolution of ZnO for various wavelengths exhibits complex behaviour with a fast contribution at early times followed by a slower decay at longer times. The process at 375nm wavelength decays faster than the one at 385nm that decays on a longer timescale with reduced amplitude. A large absorption increase is found at 400nm for longer times upto 600ps and beyond, which corresponds to the scattering in the sample. At 500nm, a fast positive absorption increase can be traced for short delay times. Additionally, ultrafast dynamics take place on 100-200fs timescale, evident from the figure 5.3(b).

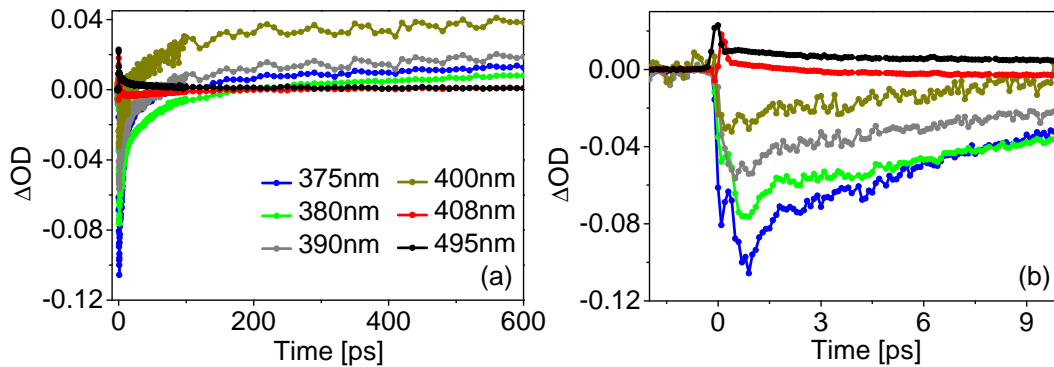


Figure 5.3 Temporal evolution of different wavelengths in time resolved spectra of E859

## 5.2.2 Results of modelling: Ultrafast carrier dynamics in ZnO films

The time resolved pump probe spectra were simulated using the model developed in chapter 4. In order to disentangle the different spectral features and identify the underlying physical processes, a variation of the parameters of the known dielectric function, resulting in modification of the absorption coefficient and refractive index, is used in the first step. Among the many parameters in the dielectric function, the criteria for choosing a particular parameter to vary in the fitting procedure are as follows. Firstly, the parameter that yield minimum squared sum of the residuals in the



optimization routine for the entire spectral range is chosen. Secondly, if there is more than one parameter that can fit to a particular spectral feature, then the parameter which has to be varied least is considered the optimal choice since physically it is a more plausible quantity to describe the observed effect. Then in the second step, all the other spectral changes that cannot be explained by the dielectric function are introduced into the mathematical framework by a Gaussian function at the appropriate spectral position. The changes in dielectric function can account for all the ground state transitions. As mentioned earlier in section 4.1, any induced process except ground state transitions must be additionally incorporated in the ellipsometric model. It has been by illustrated in section 4.4 of chapter 4 that the same set of parameters in the fitting routine cannot fit to all the spectral features in different types of data sets. There are some inherent spectral features that are observed in all kinds of time resolved measurements. For instance, the transmission increase around 375nm or the early time absorption increase around 505nm. So, the corresponding parameters are always varied in the routine. However, some data sets additionally show distinctive time dependent spectral contributions, depending on the experimental input conditions. For instance, a measurement taken for different sample thickness or one performed under strong excitation conditions. Therefore, in that case the relevant parameters are additionally varied in the model. Once the parameters are zeroed in for a data set, then the same set of parameters are consistently varied for all the subsequent time sequences. Finally all the contributions in the model have to be assigned the correct corresponding physical processes.

The modelling was done for the above presented time resolved measurement on E859. Figure 5.4 shows a corresponding fit along with all the individual contributions given by the Levenberg Marquardt optimization routine for the spectral changes measured at 1.5ps. In order to fit this data set the amplitude of discrete exciton-A,  $A_{ca}$  and  $\epsilon_{1off}$  parameters in the dielectric function need to be varied.

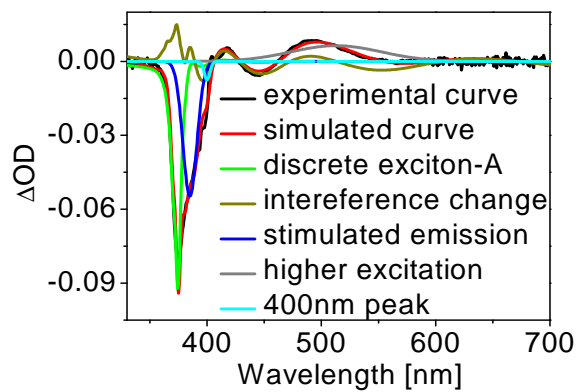


Figure 5.4 Experimental and simulated spectra depicting different contributions in the carrier dynamics of E859 at 1.5ps

It can be seen from the figure that there still remains an additional positive  $\Delta OD(\lambda)$  around 505nm which cannot be described by these dielectric function generated oscillatory modulations alone. Similarly, the 385nm transmission increase cannot be explained by any of the four contributions to the dielectric function. Therefore, based on the arguments described at the beginning of this section and in chapter 4, two Gaussian curves are introduced at 385nm and 505nm respectively to include these unaccounted

spectral contributions. A third Gaussian curve at 400nm was added to take the scattering contribution into account. This is necessary for the correct optimization of the other varying parameters, lest the routine attempts to compensate for the unaccounted contribution by an inappropriate variation of other contributions.

The simulated spectrum shown by the red curve is in good agreement with the experimental time resolved spectrum. The sum of the squared residuals given by the optimization routine is on the order of  $2.7 \times 10^{-3}$ . Fitting all the measured time sequences of the optical density changes, the temporal evolution of different contributions are simulated. The following sub-sections describe in detail the spectral as well as temporal evolutions of all the processes induced by ultrafast excitation of ZnO.

### 5.2.2.1 Interpretation of the modelled time resolved data

In figure 5.4, the most obvious spectral contribution that can be identified is the transmission increase around 375 nm which is described by the variation of the amplitude of discrete exciton-A. This transmission increase is explained by the population of the discrete exciton-A. It is important to note that the excitons cannot be directly created since the system is excited with 400nm laser pulse that is far off from its resonance at 375nm. This leads to an important conclusion that exciton bleaching cannot be the first step in the dynamics.

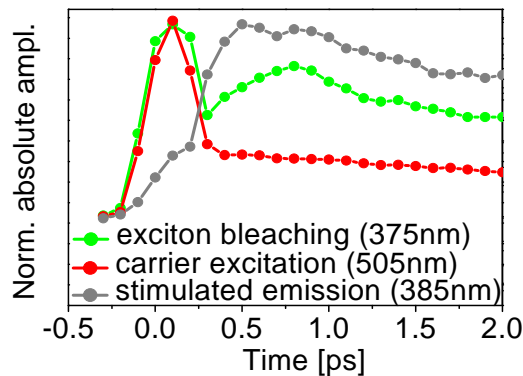


Figure 5.5 Comparison of early time evolution of various processes in the carrier dynamics of ZnO

For the identification of other contributions in the model, it is crucial to first do a comparative study of the very early time behaviour of the three contributions at 375nm, 505nm and 387nm respectively. In figure 5.5, the temporal rise of the 375nm discrete exciton bleaching, the 505nm absorption increase and the 385nm transmission increase are compared. For the sake of better comparison, the absolute values of their amplitudes are plotted. Additionally, they are normalised to show similar amplitudes. It is clearly evident that the 505nm absorption increase and exciton bleaching at 375nm rise simultaneously after excitation by 400nm pulse. Furthermore, the transmission increase at 385nm rises slowly on a longer timescale of about 1ps.

From the sequential rise of the different contributions, the time sequence of processes in the carrier dynamics can be concluded. A schematic of the bandstructure depicting different processes involved in the initial dynamics is depicted schematically in figure

5.6. The sequence of early time carrier dynamics is proposed as follows: The earliest contribution in the dynamics is attributed to the formation of photoexcited charge carriers at 505 nm. The excitation pulse depletes an intermediate initially filled and short-lived level within the bandgap. This elementary absorption of the 400 nm excitation pulse transfers electrons from defect states into the conduction band. Consequently, due to the depletion of the defect states some electrons in the valence band absorb the weak probe pulse to occupy the newly created vacant defects states showing an absorption increase at 505 nm. The excited electrons rapidly relax to the band edge and occupy the lower energy exciton levels. Since the exciton levels which are otherwise empty are now occupied, the probability of their further occupation decreases leading to increase in transmission and hence the exciton bleaching. This is confirmed from figure 5.5 where there is a rapid rise of the absorption increase at 505 nm along with simultaneous rise of exciton bleaching.

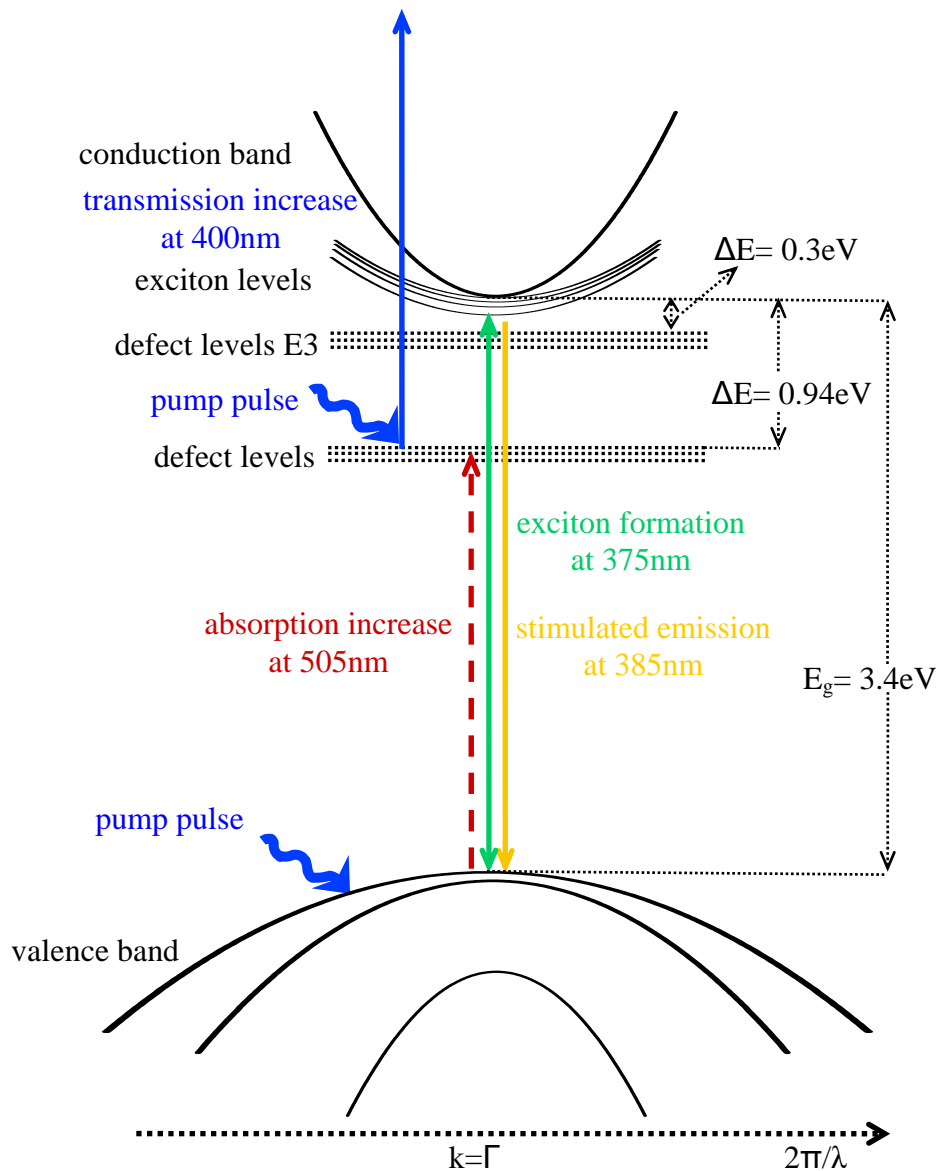


Figure 5.6 Schematic of bandstructure illustrating various processes in carrier dynamics of ZnO films

With the passage of time, as the population in the exciton level rises, their proximity increases and they begin to interact with each other. The high concentration of excitons leads to collisions between them and the energy is subsequently released as stimulated emission (SE) around 385nm. A slightly delayed and slower build up of stimulated emission in comparison to exciton bleaching in figure 5.5 confirms this assertion. The rise time of stimulated emission is rather slower than exciton bleaching itself since it takes some time for the exciton population to build up before the exciton-exciton scattering starts. For recombination of electrons, holes required at the top of the valence band are most probably created by the interaction of the pump pulse with the valence band. The relaxation of holes to the top of the valence band may also require some time as well, contributing to the delay in the stimulated emission.

### 5.2.2.2 Carrier excitation

The positive absorption increase around 505nm is principally explained by contributions of carrier excitation from defect states. The pump pulse excites the carriers from the defect states located within the bandgap to the conduction band. Consequently, the formation of vacancies in these defect levels induces absorption increase centred around 505nm. A rather broad absorption increase indicates that these defect states do not have discrete levels but are diffused in the k-space. The above mentioned rapid absorption increase at around 500nm due to defect levels can be correlated well to the oxygen vacancies. Photoluminescence measurements done on undoped ZnO exhibit a green luminescence band peak at 2.45eV (~506nm) attributed to defects arising from oxygen vacancies in ZnO [3,4,5,6].

Figure 5.7 illustrates the spectral variation of this contribution. The amplitude, width as well as centre wavelength of this contribution were varied in the model. The temporal behaviour of the carrier excitation contribution is plotted as a function of delay time in figure 5.8. With a rise time of ~300fs, the contribution has the fastest build up among all contributions and decays very rapidly on the next 300fs timescale. Thereafter, only small residual component remains which decays gradually. From figure 5.8(a), it is clear that the width of carrier excitation increases from 40nm to approximately 78nm for very early times. At later times, the decrease in amplitude is accompanied by increase in the width. Also, figure 5.7 shows that the spectral position shifts from 465nm towards the red side of the spectrum to 530nm and then the peak shifts back

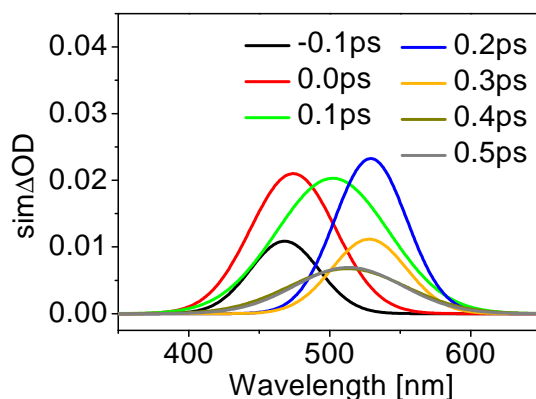


Figure 5.7 Spectral evolution of carrier excitation contribution for selected delay times

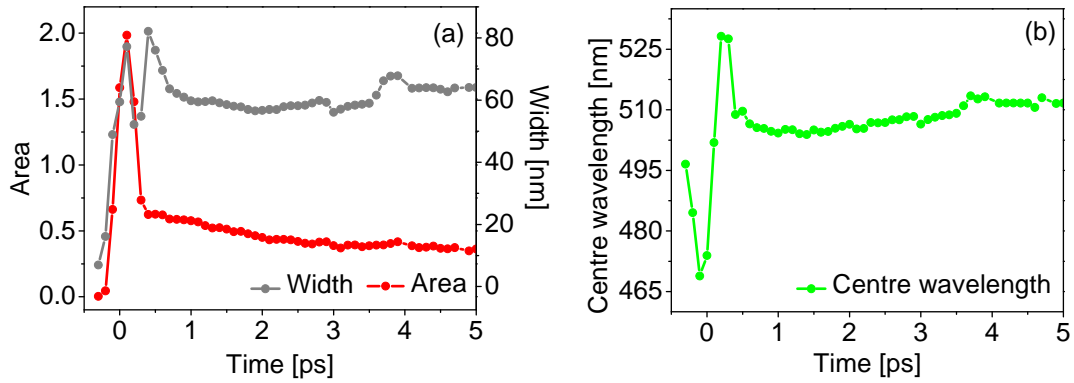


Figure 5.8 Time evolution of area, width and spectral position of carrier excitation contribution

slightly to 505nm. Figure 5.8 (b) shows that the shift towards the red side of the spectrum persists only till the first 500fs after which the peak shifts back to the blue side to 495nm till the contribution decays back by 100ps. The shift can be attributed to coherent interactions taking place at very early delay times in which the positions of the energy levels are not fixed.

### 5.2.2.3 Bleaching of discrete exciton

The transient optical density spectrum reveals the bleaching of exciton-A at 375nm. Figure 5.9 schematically depicts the process of bleaching. When the sample absorbs a photon of a certain wavelength, it excites an electron from valence band to the upper state which can either be conduction band or an exciton level, consequently leaving a hole behind. This leads to a subsequent decrease in the population of carriers in the ground state available for further absorption. As a result, the transmission is increased and the sample bleaches at that wavelength.

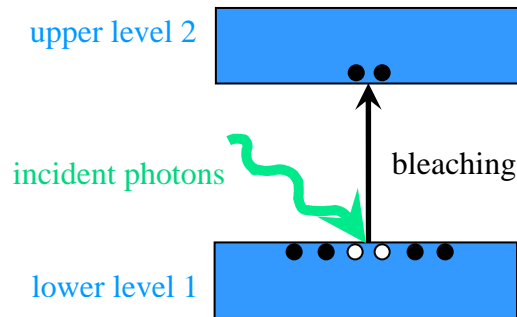


Figure 5.9 Schematic of a two level system depicting bleaching

Mathematically, the transmission change which occurs during transition between a two level system is given by equation 5.1. If the number of carriers in levels 1 and 2 are given by  $N_1$  and  $N_2$  respectively, then the change in optical density can be written as given in equation (5.1).

$$\Delta OD(\lambda, t) = \Delta T(\lambda, t) = \frac{T_1(\lambda, t)}{T_2(\lambda, t)} = e^{-\sigma \cdot (N_1(\lambda, t) - N_2(\lambda, t)) \cdot x} \quad (5.1)$$

The absorption cross-section and scattering length are given by  $\sigma$  and  $x$ . The population of both the levels before excitation by the pump pulse is written in equation 5.2. Before the excitation, when all the carriers occupy the ground state, the initial number of carriers in the ground state is  $N$  and that in the excited state is zero.

$$N_1' = N, N_2' = 0 \quad (5.2)$$

$$N_1 = N - \Delta N, N_2 = \Delta N, \Delta N = N_1 - N_2 = -2\Delta N \quad (5.3)$$

$$\Delta OD(\lambda, t) = \log \Delta T(\lambda, t) \propto N_1 - N_2 = -2\Delta N(\lambda, t) \quad (5.4)$$

After excitation with pump pulse,  $\Delta N$  carriers are transferred to the upper state. Transient increase of the occupation of the higher state leads to consequent depletion of the ground state. As a result, the total number of electrons available in the ground state to further absorb photons decreases. The difference of occupation becomes smaller by  $2\Delta N$  as shown by equations (5.3) and (5.4). This decrease in absorption leads to transmission increase and the sample bleaches at the corresponding wavelength.

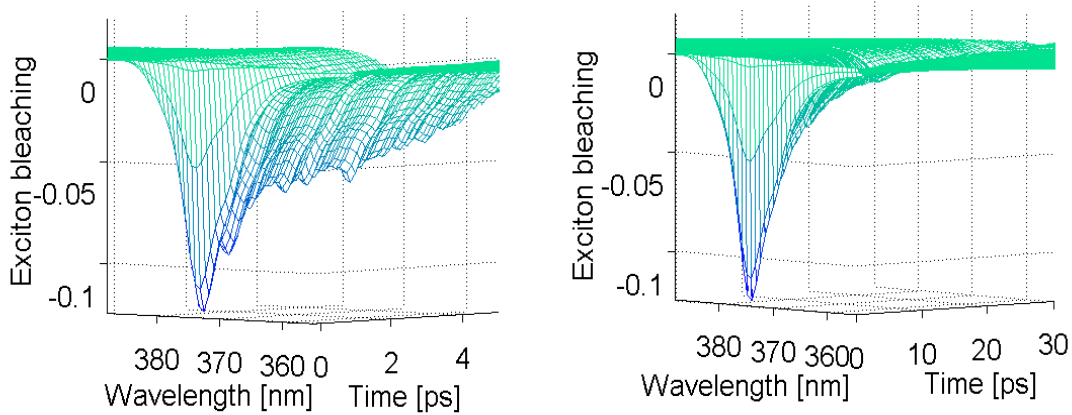


Figure 5.10 Three dimensional views the spectral evolution of bleaching of discrete exciton-A for two different timescale of 5ps and 30ps respectively

Figure 5.10 shows three dimensional views of the spectral as well as temporal evolution of exciton bleaching contribution. After the pump excitation, the population in exciton

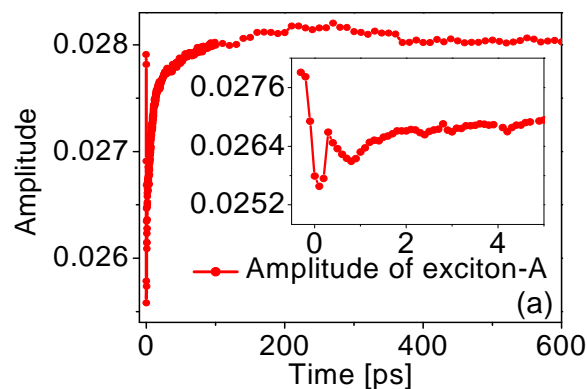


Figure 5.11 Temporal evolution of discrete exciton-A bleaching

level increases leading to an increase in amplitude of the exciton bleaching for early delay times. Higher exciton states with  $n \geq 2$  causes broadening of the blue wing of the bleaching peak. The maximum change in amplitude of exciton-A is 8.28%. Figure 5.11 shows the time evolutions of the amplitude of discrete exciton-A. It can be clearly seen that the exciton bleaching is nonexponential with fast component on less than 500fs timescale followed by a second longer lived contribution. The fast contribution of exciton bleaching peaks at around 0.1ps after which it decays for a short time till 0.3ps. At  $\sim 0.8$  ps, again a dip is observed after that it decays monotonously. Figure 5.11(a) reveals that the exciton recombination takes place on 20ps times scale.

#### 5.2.2.4 Stimulated emission

The right shoulder of the A-exciton bleaching at 385nm is attributed to stimulated emission. There are two possibilities for transmission increase to occur. It can occur due to bleaching, but none of the components in the dielectric function can explain this negative contribution as bleaching. The second possibility for transmission increase is brought upon by stimulated emission. The general description of stimulated emission is presented in section 3.1 of chapter 3. Since it is an induced process, it is not contained in the dielectric function. This physically justifies the need to incorporate this contribution as an additional Gaussian curve in the model. The amplitude and width were varied while the centre wavelength was kept fixed at 387nm. The spectral as well as temporal variation of this contribution can be visualised in figure 5.12. Centred at around 385nm, the stimulated emission increases in amplitude and spans a spectral range between 375-400nm width as time progresses.

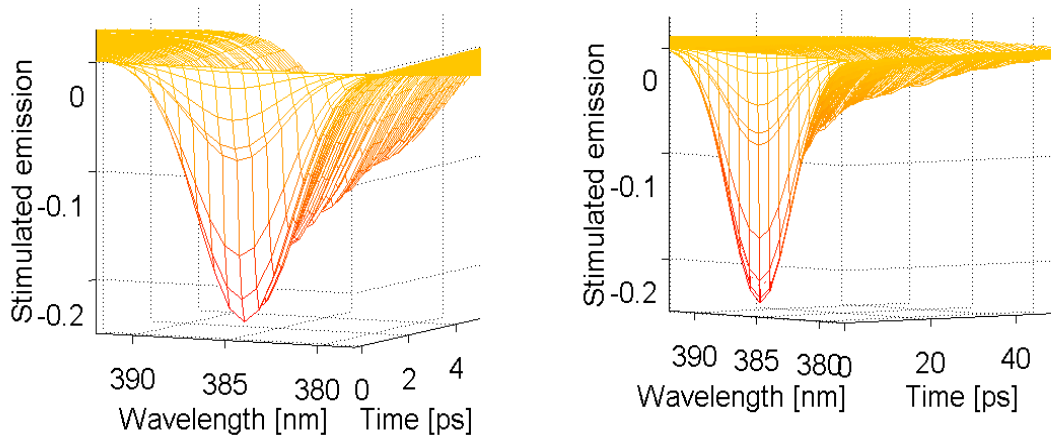


Figure 5.12 3-D view of temporal as well as spectral evolution of stimulation emission

The temporal evolutions of area and width of the stimulated emission are shown in figure 5.13. Being a relatively slow process, the SE peaks at 0.5ps accompanied by increase in area and width. It must be emphasized that the time evolution of area under stimulated emission is not a single exponential. It indicates two processes; a fast component followed by a slower decay on 200ps timescale. A second order exponential fit fitted to the area of stimulated emission yields time constants of  $\sim 4$ ps and  $\sim 34$ ps.

Instead of the exciton wavelength of 375nm, the stimulated emission occurs at 385nm. This implies that some intermediate states are involved in the process to where the excitons relax rapidly, before the SE takes place. After the excitation, the stimulated emission is observed to rise relatively slower. This is because after the exciton

formation begins, some time is required during which the exciton population rises before efficient exciton-exciton scattering takes place. Additionally, the holes are needed at the top of the valence band to directly recombine with the electrons in the upper level during SE. Since the valence band is broad, the heavy holes take some time to reach of the top of the band (phonon assisted transitions) which may also add to delay in SE rise.

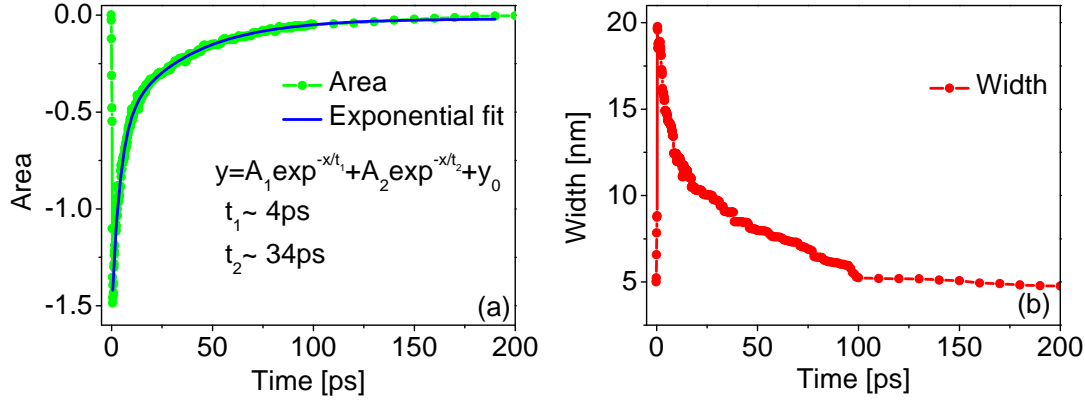


Figure 5.13 Time evolution of area and width of stimulated emission

Optically pumped stimulated emission has been observed in ZnO films by many researchers [4,7]. The centre frequency of the observed stimulated emission at 385nm corresponds to  $\sim 3.17$  eV emission due to inelastic exciton-exciton scattering observed under high excitation conditions reported in literature [8,9,10,11,12,13]. ZnO has large exciton binding energy of  $\sim 60\text{meV}$  which makes the exciton stable at room temperature. The inelastic collisions between the excitons result in one of the two excitons scatter into a higher state while the other recombines radiatively. At low power, the density of exciton is small and the separation between excitons is large. The efficiency of exciton-exciton scattering is very low. At high power, the density of carriers in the exciton level increases. Eventually, the density is high enough so that exciton-exciton-interactions become significant, as a result the efficiency of stimulated emission enhances. The exciton wave functions overlap occurs when the exciton-exciton distance is equal to exciton diameter. The density at which this occurs is known as the Mott density. The Mott density in ZnO at room temperature is given by equation (5.5) where exciton Bohr radius is  $a_B = 18\text{\AA}$  and  $E_B^{ex} = 60\text{meV}$  for ZnO.

$$n_M = \frac{K_B T}{2a_B^3 E_B^{ex}} \approx 3.7 \times 10^{19} \text{ cm}^{-3} \quad (5.5)$$

When the exciton density approaches Mott density, collisions between excitons cause the exciton gas to dissociate into an electron-hole plasma (EHP) and the highly energetic charge carriers are no longer bound to form excitons. This effect occurs at very high excitation intensities. This causes exciton broadening with reduction in the absorption strength. It is reported that SE originating from exciton interactions and/or recombination of EHP can be observed depending on the excitation intensity and the quality of the samples. In the presented work, since the excitation wavelength lies within the bandgap, the possibility of stimulated emission due to EHP can be excluded. Stimulated emission and lasing was observed at room temperature in ZnO films grown



by plasma enhanced MBE on *c-plane* sapphire, for excitation intensities exceeding  $400\text{kW}/\text{cm}^2$ . The exciton-exciton scattering related stimulated emission peak appeared at  $3.18\text{eV}$  that grew superlinearly. At higher excitation intensities ( $800\text{kW}/\text{cm}^2$ ), the electron hole plasma peak was found at  $3.14\text{eV}$  which broadened and red shifted due to bandgap renormalization with further increase in the excitation intensity. They reported threshold for the stimulated emission lines from the exciton-exciton scattering and EHP mechanisms to be  $1.2$  and  $1.9\text{MW}/\text{cm}^2$  respectively. At high exciton densities, other effects like the formation of exciton molecules known as biexcitons, emission due to biexcitons, exciton-exciton and exciton-carrier interactions may also be observed [14,15,16].

### 5.2.2.5 Interference contribution

For the description of the long wavelength modulations between  $400\text{-}600\text{nm}$ , a rather complex variation of the dielectric function is needed. The oscillatory behaviour is simulated by varying the amplitudes of continuum exciton-A,  $A_{ca}$  and the real constant term,  $\varepsilon_{\text{off}}$  since they both add up in the region between  $400\text{-}600\text{nm}$  and nullify each other's contribution in UV to keep the  $\Delta\text{OD}(\lambda)$  close to the experimentally observed value of zero. The detailed analysis about the choice of this combination of parameters has been discussed in section 4.3 of chapter 4. The oscillatory behaviour can be explained as a result of change in refractive index induced by the pump pulse. The pump pulse increases the refractive index of ZnO as a result of which the interference pattern is modified.

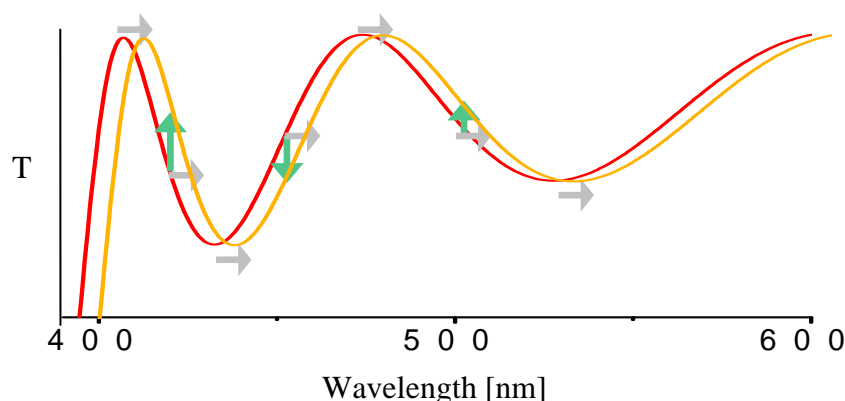


Figure 5.14 Schematic depicting change in transmission spectrum of E859 upon excitation by pump pulse

Upon excitation, the pump pulse shifts the transmission spectrum. Figure 5.14 schematically describes the modification in the intensity distribution. In the figure, the original transmission spectrum shown by the red curve is shifted to higher wavelength side. The original interference pattern in transmission spectrum of E859, depicted as red curve, shifts towards the red side of the spectrum. Maximum change in transmission occurs at the points of zero-crossing i.e. at the centre of the rising and trailing parts of the oscillation. In the time resolved pump-probe spectra (refer to figure 5.1), it can be seen that the peaks of the oscillations indeed occur at these wavelengths ( $\sim 408\text{nm}$  and  $500\text{nm}$ ). At the maxima and minima positions of the transmission curve, only the spectral position is shifted but there is no change in transmission intensity and hence in the optical density.

In figure 5.15, the spectral variation of simulated oscillations is plotted for selected delay times. The oscillations increase with time, peaking at 0.5ps. Their contribution is almost negligible after 20.5ps. As evident from the figure, the oscillations also produce a large complex variation below 380nm. Additionally, it should be noted that the 2<sup>nd</sup> negative peak at 390nm contains a small interference contribution due to refractive index change.

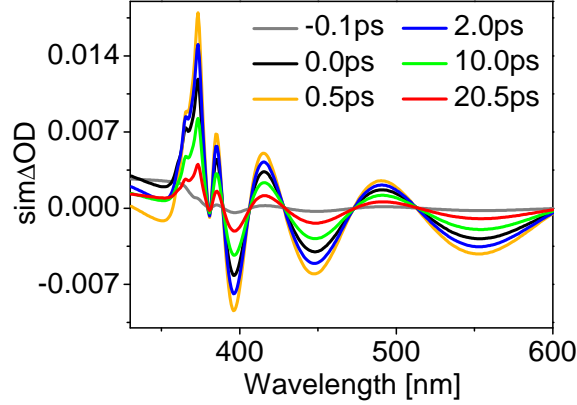


Figure 5.15 Spectral evolution of interference oscillations for selected delay times

In figure 5.16, parameters  $A_{ca}$  and  $\epsilon_{1off}$  that generate these oscillations are plotted as a function of time. They both show a very similar time evolution with a fast component is traced on less than 1ps timescale. Overall, both the components decay back to their original values on a ~20ps timescale.

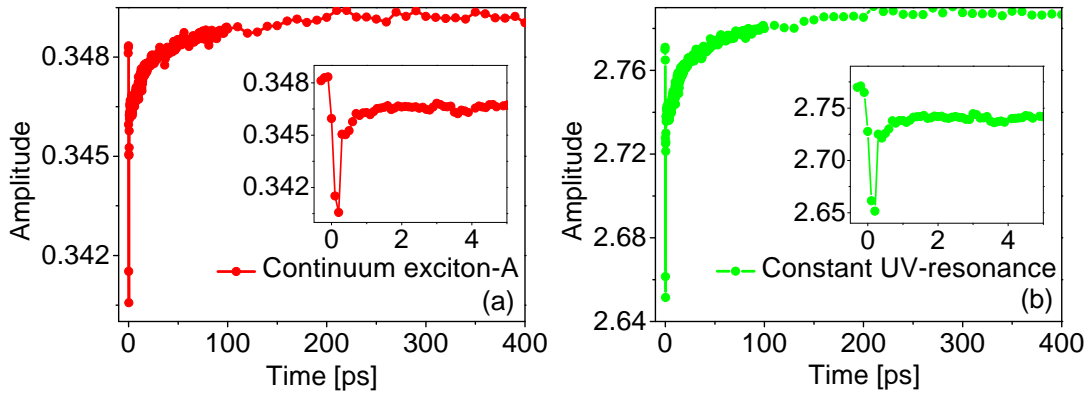


Figure 5.16 Time evolution of continuum exciton-A and  $\epsilon_{1off}$

It is clear from equation (3.19) of chapter-3 that apart from refractive index change, another possibility of interference change is due to change in sample thickness. During volume expansion and contraction, the excited carriers couple to phonons or lattice vibrations which generates a mechanical perturbation in the sample. The phonons in material medium travel at the speed of sound. For a film of thickness  $t$ , the required time  $T$  for volume expansion to occur can be calculated using equation (5.6).

$$v = \frac{t}{T} \quad (5.6)$$

$$t = 458\text{nm}, v = 340.29\text{m/s} \rightarrow T \approx 1.35\text{ns} \quad (5.7)$$

This simple estimation shows that for E859, the thickness change will occur on the order of nanoseconds. However, the time scale on which the observed oscillations decay in the time resolved spectra of ZnO is on the order of  $\sim 50\text{ps}$ , which is too fast for volume expansion. This confirms that the observed change in interference pattern in the time resolved spectra is indeed due to modification in the refractive index of ZnO by the excitation pulse.

### 5.2.2.6 Transmission increase at 400nm

If the proposed sequence in the interpretation of early time carrier dynamics is correct, then the transmission increase at 400nm due to the transfer of carriers to the defect states and consequent depletion of defect states must be observed as well in the time resolved spectra. In order to take the scattering contribution by the pump pulse into account in the model, a Gaussian curve was added at 400nm. The three dimensional visualisation of the spectral and temporal variation of the Gaussian curve is shown in figure 5.17. In the figure, transmission increase at early delay times and large absorption increase for later times can be observed. However, it is not possible to decisively conclude anything from these observations for E859 since it shows considerable scattering at the 400nm pump wavelength, as pointed out in section 2.3.4 of chapter 2. All the presented data have been corrected for scattering, but it doesn't appear to be stable with delay time. The presence of the inherent scattering around 400nm makes any relevant physical interpretation of the observed spectral changes very dicey. Moreover, it can be seen from figure 5.2(b) that the spectral width of the observed feature around 400nm is larger than that of the pump pulse ( $\sim 2.2\text{nm}$ ) which suggests that there may be additional processes taking place. The E3 defect levels at 400nm attributed to oxygen vacancies mentioned in chapter 3 cannot be the reason behind it since they are optically not active.

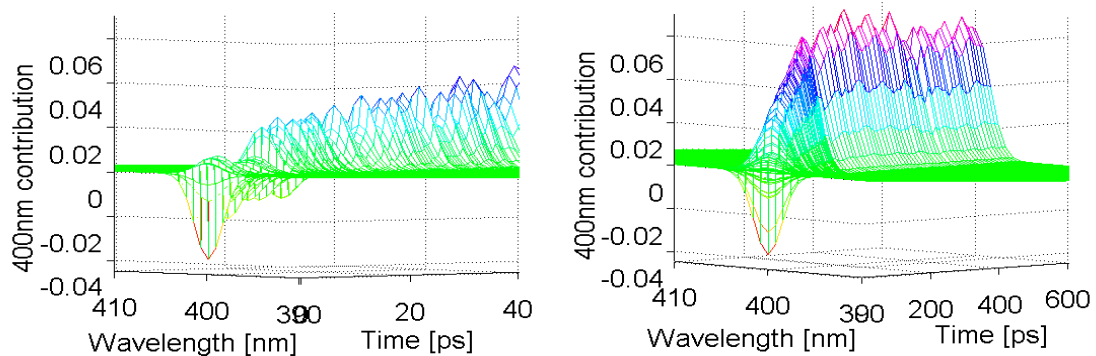


Figure 5.17 Spectral and temporal evolution at 400nm

To get around the problem of scattering, time resolved measurements were performed on a different E1962 which exhibits lesser scattering. The experimental spectral variation for this film is plotted in figure 5.18 for short times upto 0.5ps. In this sample, the transmission increase at 400nm is clearly evident. Analysing the time evolution at 400nm yields a clearer picture since it is not influenced by the scattering. First a very fast absorption increase is observed and then the expected transmission increase occurs. The rapid absorption increase is most probably due to coherent interactions prevalent at

very early time. At times much longer than the duration of the pulse, only incoherent interactions are present. The time evolution reveals that the overall lifetime of the 400nm transmission increase is very short, it decays on less that 0.2ps timescale. The bleaching at 400nm for early delay times confirms concretely that the above interpretation of the pump pulse exciting the carrier from defects levels at 400nm and the simultaneous absorption increase around 505nm in the carrier dynamics is indeed correct.

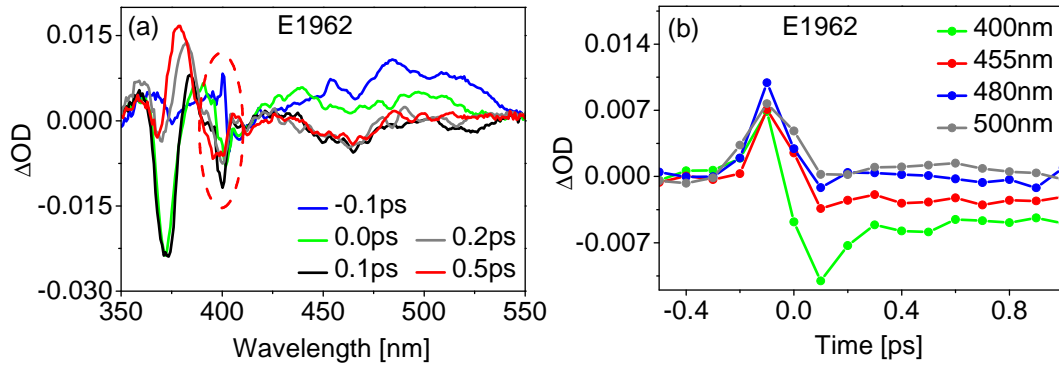


Figure 5.18 Change in optical density for E1962 for selected delay times

### 5.2.3 Effect of temperature

Upon excitation by the pump pulse, at first very fast coherent dynamics containing the phase information of the processes take place. The excited electrons then collide with each other leading to the loss of coherence. As the electrons scatter with each other, they lose energy in the form of heat and the electronic temperature of the film increases. This is generally a fast process. The electrons thereafter couple to the phonons to slowly transfer heat to the lattice leading to an increase in the lattice temperature. The heat is finally dissipated to the thermal bath (surroundings).

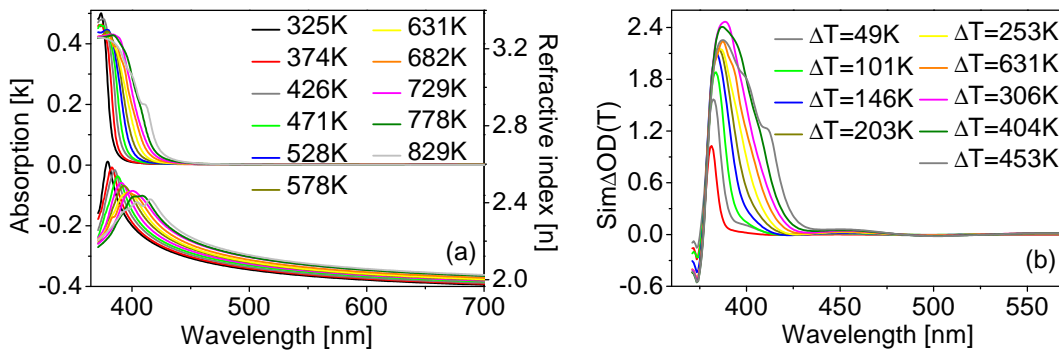


Figure 5.19 (a) Temperature dependent absorption and refractive index of ZnO (b) Change in optical density as a result of temperature change

In order to estimate the influence of temperature on the time resolved spectra, the dielectric function of ZnO measured at different temperatures ranging from 325K to 829K was studied. These measurements were not performed on the ZnO films under investigation. Figure 5.19 (a) shows the absorption and refractive index of ZnO with increase in temperature. Using the temperature dependent dielectric function, the change in optical density as a result of temperature variation can be calculated. The change in

optical density can be defined as the difference between the optical density at temperature before the excitation and that after excitation, as expressed in equation (5.8) and (5.9).

$$\Delta OD(T) = OD(T_{before.excitation}) - OD(T_{after.excitation}) \quad (5.8)$$

$$Transmission(\alpha(T), n(T)) = \frac{(1-r(T))^2 e^{-\alpha(T)t} \left[ \left(1-r(T)^p e^{-p\alpha(T)t}\right)^2 + 4r(T)^p e^{-p\alpha(T)t} \sin^2(p\delta(T)) \right]}{\left(1-r(T)e^{-\alpha(T)t}\right)^2 + 4r(T)e^{-\alpha(T)t} \sin^2(\delta(T))} \quad (5.9)$$

Figure 5.19(b) shows the change in optical density spectra due to a series of temperature changes. The analysis shows that the thermalization of the ZnO film induces a significant change in the absorption coefficient around  $\lambda=380\text{nm}$ . With larger increase in temperature, the amplitude of the contribution increases accompanied by a spectral shift to the red side of the spectrum. Reports in the literature show the thermalization process to be on the order of several picoseconds. This is evident in the time evolution of ZnO sample as well (refer to figure 5.1(d)) where positive absorption increase can be seen for wavelengths between 373-390nm stretching up to 600ps and beyond. Though the amplitude of the observed 380nm peak in the time resolved spectra is much smaller than that shown in figure 5.19(b). It should be noted that these temperature dependent absorption coefficient and refractive index were measured with the sample in equilibrium state at all temperatures. However, in pump probe spectroscopy, the sample doesn't remain in thermal equilibrium after excitation. Hence, the initial conditions for both studies should be considered carefully.

Additionally, it is important to note that not all the pump energy is utilized in the pump-probe measurement with 400nm excitation pulse. A small fraction of the pump pulse (approximately 5%) of the total pulse energy is absorbed by the sample since it is excited at 400nm far off from its resonance at  $\sim 365\text{nm}$ . The effect of temperature can be strongly influenced by the experimental conditions. The spectral position and amplitude of this contribution is affected by the pump energy as well as the overlap between the pump and probe pulses on the sample. The probe pulse measures the volume that is illuminated by the pump. If the overlap between both the beams on the sample surface is not maximum, then the probe pulse will not measure the entire heated volume but only a part of it and as a result the effect of temperature will be less prominent.

## Summary

The ultrafast carrier dynamics in E859 film was investigated by time resolved pump probe spectroscopy. The time dependent spectral changes were modelled using the ellipsometric model developed in chapter 4. The carrier dynamics in ZnO can be resolved into five fundamental contributions. There is weak absorption increase centred at around 505nm principally be explained by contributions of carrier excitation from defect states. It rises and decays on  $\sim 600\text{fs}$  time scale. This elementary absorption of the excitation pulse transfers carriers from defect states located within the bandgap to the conduction band, giving rise to transmission increase at 400nm for early delay times. The initially displaced carriers in the conduction band relax rapidly to the bottom

of the band. The carrier excitation leads to the bleaching of discrete exciton-A at 375 nm. With the passage of time, the carrier density in the exciton levels increases, so much so that they begin to interact with one other. The exciton-exciton scattering finally leads to stimulated emission centred at around 385 nm. Stimulated emission rises slowly on ~1ps timescale. The time evolutions of both exciton bleaching as well as stimulated emission exhibit complex non-exponential decay with fast and slow contributions. Overall, the exciton bleaching decays on 20ps timescale while the stimulated emission lasts upto 200ps. Changes in the refractive index of the sample by the excitation pump pulse generates oscillatory behaviour between 405-600 nm. To verify and confirm the described background of these processes in the time resolved carrier dynamics of ZnO, further measurements were performed which are discussed in section 5.3, 5.4 and 5.5. Analysis of the temperature dependent dielectric function of ZnO revealed that the 380nm absorption increase at longer times stretching beyond 600ps in the time resolved spectra in ZnO is a manifestation of temperature.

### 5.3 Carrier dynamics in ZnO for different pump wavelengths

The nature of the observed time resolved relaxation mechanisms in ZnO was further investigated by performing excitation wavelength dependent experiments on ZnO films with three different excitation wavelengths. In addition to 400nm pump excitation, information about the temporal evolution of the transient photoinduced spectral changes was probed by exciting with pump wavelengths of 391nm and 409 as well. It was established in section 5.2 that the excitons are indirectly excited with 400nm wavelength. The intent of selecting 391nm was to investigate if there is alteration in the excitation pathway by moving 9nm closer to the discrete exciton resonance. On the contrary, indirect excitation of excitons would take place by moving the excitation wavelength to 409nm which is even farther from the resonance. As a direct consequence, the subsequent relaxation processes may get altered. The time resolved measurements were performed by fixing the excitation energy to  $15.5\mu\text{J}$ .

#### 5.3.1 Experimental results

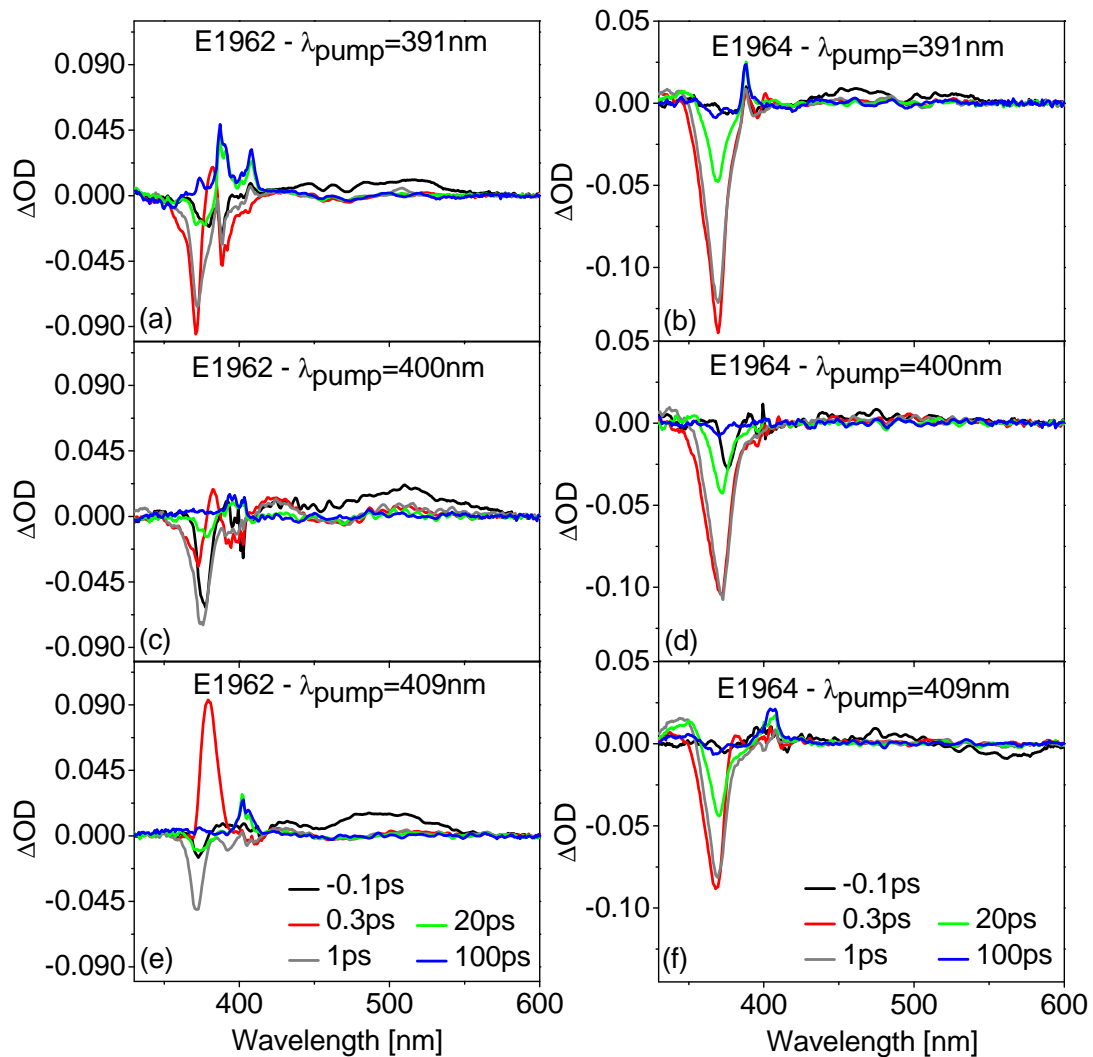


Figure 5.20 Experimental spectral variation of E1962 and E1964 for 391nm, 400nm and 409nm pump wavelengths respectively

Figure 5.20 shows the transient optical density spectra obtained for E1962 and E1964 with different pump wavelengths. Analysing the time resolved spectra for the thinner sample first, E1964 shows enhanced excitonic bleaching as the pump wavelength is decreased from 409nm through 400nm to 391nm. The induced absorption between 325-353nm is maximum for 391nm pump wavelength and peaks at 0.5ps. This contribution is diminished for higher pump wavelengths. There is no significant difference in the spectral variation between 400-600nm after excitation with different wavelengths. Like in E1964, the exciton bleaching decreases with increasing the pump wavelength in E1962 as well. In this sample, the 380nm contribution varies dramatically for different pump wavelengths. From 391nm excitation to 409nm, it increases more than twice in amplitude. Interestingly, for the 409nm pump at 0.3ps, it completely overrides all other processes occurring in the vicinity of 380nm. However, no significant difference in the oscillatory contribution was found between 391nm and 409nm pump, though the modulations are slightly stronger with 400nm excitation wavelength. At longer delay times, two broad spectral peaks are traced corresponding to an absorption increase at 388nm and 408nm that persist beyond 600ps. However, the long lived peaks at 380nm and 408nm don't seem to appear with 400nm excitation.

The time resolved spectra for different pump wavelengths were modelled using the Levenberg Marquardt optimization procedure. The key results of modelling are discussed in detail for E1962 in the following section since it exhibits the most dramatic difference in time resolved spectral changes for different excitation wavelengths. The amplitudes of all three excitons were varied in the optimization routine. The area, spectral width as well as centre wavelength of carrier excitation were optimized as well. The width and area of the Gaussian curve for the 380nm absorption increase were changed while the centre wavelength was kept fixed. The experimental spectra after 391nm and 408nm excitation exhibit broad scattering peaks at 388nm, 400nm and 408nm. Therefore, in order to fit the simulated curve with the experimental spectrum, three additional Gaussian curves were introduced in the routine at 388nm, 400nm and 408nm respectively. Along with the centre wavelength, the widths of 388nm and 400nm and 408nm curves were fixed at 5nm, 3nm and 5nm respectively. For consistency, all three contributions were included to model different excitation wavelengths.

### 5.3.2 Carrier excitation for different excitation wavelengths

The area, spectral width as well as centre wavelength of carrier excitation were optimized in the routine. The spectral variation of this contribution plotted in figure 5.21(a)-(c) demonstrates immense spectral coverage between 350-660nm. The FWHM are approximately 92nm, 110nm and 115nm at the maximum amplitude with 391nm, 400nm and 409nm pump wavelengths respectively. The carrier excitation sequentially increases as the pump wavelength is shifted from 391nm to 409nm. This reveals that there is more efficient and stronger absorption of longer wavelengths by the defect states. On the other hand, their absorption strength reduces if the pump wavelength is shifted closer to the bandgap. In figure 5.21(d), the temporal evolution of carrier excitation is plotted for early delay times for all the three excitation wavelengths. It depicts that except for difference in amplitudes, the time evolution of this contribution is rather similar for all 400nm and 409nm pump wavelengths with a rise and fall time of less than 0.5ps. With 391nm excitation, it decays slightly faster. When the pump interacts with the defect levels and depletes them, irrespective of the excitation



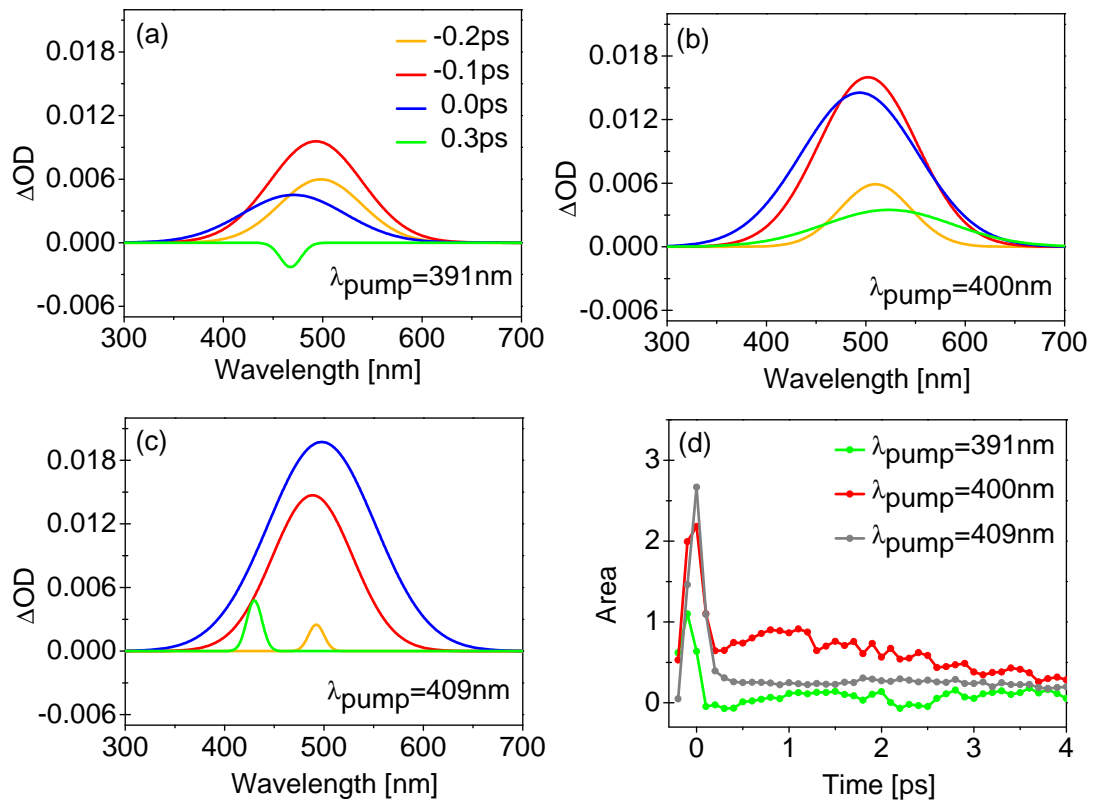


Figure 5.21 Spectral evolution of carrier excitation contribution after excitation with (a) 391nm (b) 400nm (c) 409nm (d) Temporal variation of carrier excitation at different pump wavelengths

wavelength, the rate of build up and decay absorption increase due to carrier excitation must indeed be independent of the pump wavelength.

### 5.3.3 Indirect and direct formation of excitons

Figure 5.22 shows spectral evolution of bleaching of discrete excitons-A, B and C for 391nm, 400nm and 409nm excitation wavelengths. It is clearly visible that the amount of exciton bleaching decreases with increasing pump wavelength. The early time spectra observed after excitation with shorter wavelength (391nm) gets broader on the short wavelength side due to higher occupation of exciton-B and C levels compared to the corresponding spectrum observed after 409nm excitation. The adjoining table in figure 5.22 summarizes the maximum percentage in the three exciton amplitudes upon excitation with 391nm, 400nm and 409nm wavelengths. With 409nm pumping, approximately 6.1% of exciton-A levels are occupied while exciton-B and C experience negligible population. Excitation with 400nm increases the maximum population of exciton-A level to 14.8%. The broadened blue wing of the bleaching peak after 391nm excitation appears due to higher transient population of excitons in A, B and C levels of 8.1%, 8.5% and 2.7% respectively.

Although the carrier excitation from the defect levels is reduced upon excitation with shorter wavelength, even then the exciton bleaching contribution increases. This proves

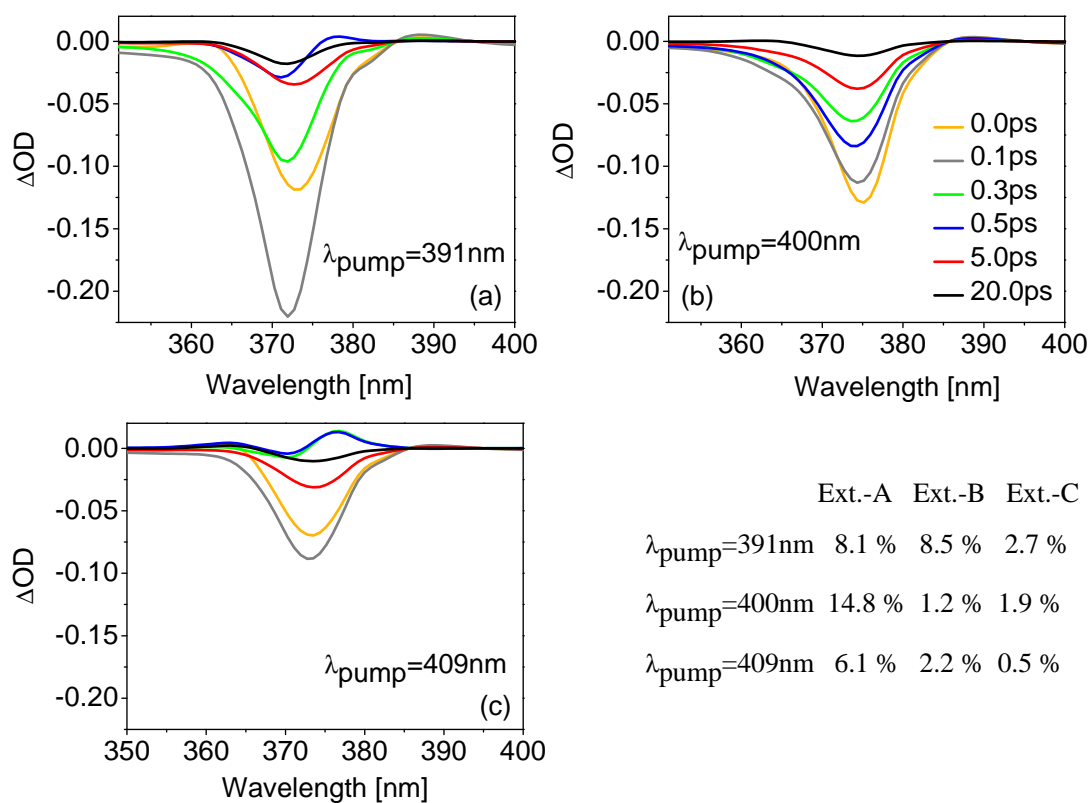


Figure 5.22 Spectral variation of bleaching of excitons-A, B and C at different pump wavelengths

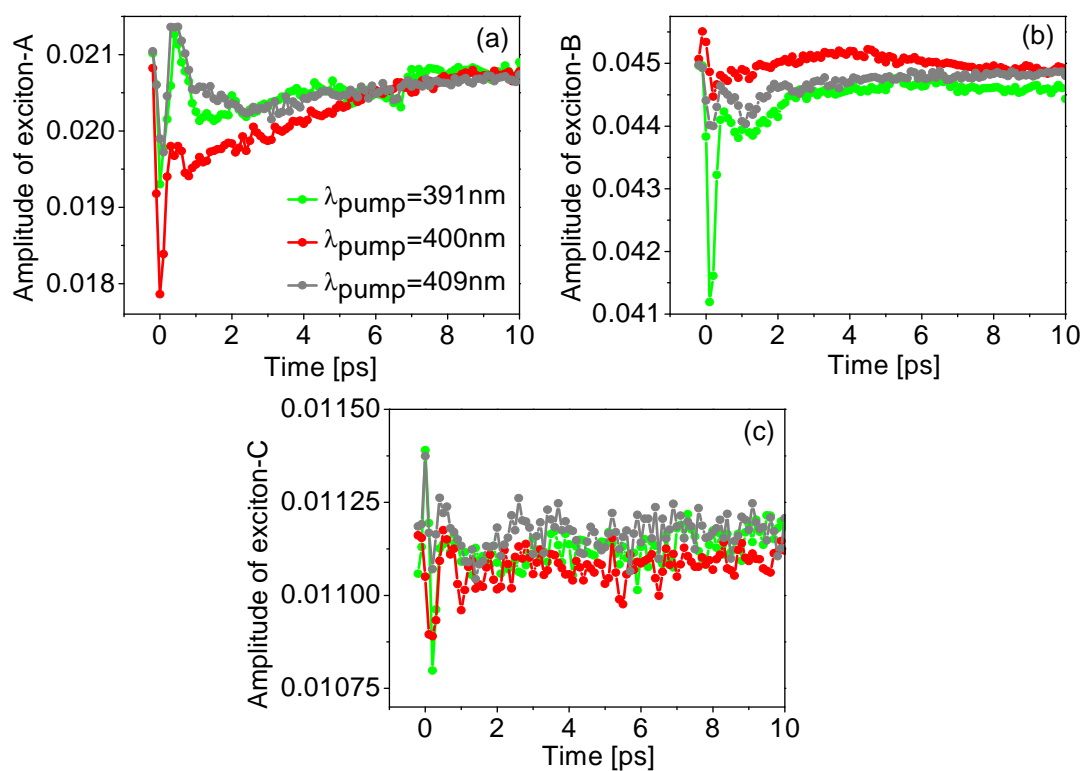


Figure 5.23 Temporal evolutions of all the three exciton contributions after excitation with 391nm, 400nm and 409nm wavelengths

that apart from the excitation pathway via defect levels, some direct formation of excitons also takes place when the wavelength of excitation is moved closer to the exciton resonance. Direct excitation with 391nm is plausible as it lies in the far red wing of the exciton absorption.

The temporal evolution of exciton-A, B and C amplitudes is plotted in figure 5.23 for all three excitation wavelengths. There is a very fast component on less than 0.5ps time scale followed by a slow component for excitons-A, B and C for all the three pump wavelengths. The short time decay dynamics of excitons is not significantly influenced for the chosen range of the excitation wavelengths. Though the long time behaviour of exciton-A and B exhibit variation in their decay with excitation wavelengths. When pumped with 391nm, excitons-A and B decay on ~8ps timescale. With 409nm excitation, the excitons decay fastest.

### 5.3.4 Bleaching at different excitation wavelengths

It was established in section 5.2 that when the 400nm pump pulse interacts with the defect states, carriers from these states are excited to the conduction band giving rise to transmission increase at 400nm accompanied by an induced absorption around 500nm. If this holds true, then when the excitation wavelength is changed, transmission increase must always be observed at their corresponding spectral positions. In order to study this, the experimental temporal evolution at 400nm and 409nm are plotted for the corresponding pump wavelengths respectively. Indeed, there is a very rapid change in optical density at the wavelengths of excitation. As already mentioned in section 5.2,

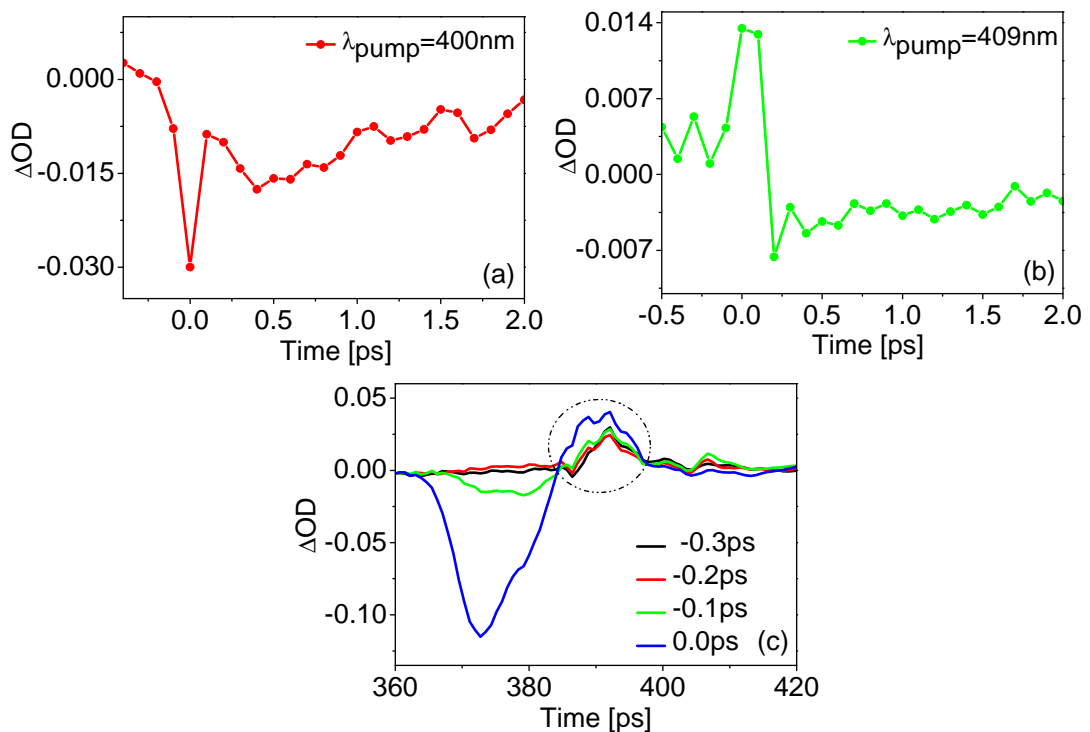


Figure 5.24 Transmission increase at the excitation wavelengths of (a) 400nm (b) 409nm and (c) scattering at 391nm

here too the coherent interactions show their signature as rapid positive and negative  $\Delta OD(\lambda)$  at very early delay times. But no transmission increase could be traced at 391 after 391nm excitation due to large amount of scattering at this pump wavelength. For illustration, figure 5.24 shows the spectra for 391nm excitation at early delay times. With such a high amount of scattering at 391nm, it is impossible to detect any transmission increase at that wavelength since the expected change in amplitude of the desired contribution at 391nm falls in the range of error.

## Summary

The optical response after excitation with different wavelengths provided fundamental information about the relaxation mechanisms in the ZnO films and successfully confirmed the proposed interpretation about the nature of excitation mechanisms and exciton bleaching processes explained in section 5.2. The excitation wavelength dependent measurements showed the primary excitation from defect levels always occurs with all three pump wavelengths. This absorption increase around 505nm increase with increasing pump wavelength but no significant influence on its temporal behaviour is traced. The investigation also revealed that apart from indirect excitation, some direct formation of excitons also takes place with 391nm excitation wavelength. However, excitons are indirectly created after pumping with 400nm and 409nm respectively. The recombination decay lifetime of excitons show slight pump wavelength dependence. A rapid transmission increase at the excitation wavelength was observed after excitation with 400nm and 409nm which proved the conjecture made in section 5.2 more conclusively that the excitation of carriers from the defect states with a simultaneous absorption increase around 505nm is the excitation mechanism in the ultrafast dynamics in ZnO films. Additionally, the studies also revealed that in E1962, a fast rising absorption increase is present at around 380nm contribution which depends significantly on the excitation wavelength. The exact background of this contribution and its correlation with pump wavelength are not yet clear.

## 5.4 Intensity dependence of time resolved dynamics in ZnO

In order to investigate the intensity dependence of the carrier dynamics in ZnO, the time-resolved pump-probe measurements were carried out at four different excitation energies of  $7.5\mu\text{J}$ ,  $14.5\mu\text{J}$ ,  $28.0\mu\text{J}$  and  $56.0\mu\text{J}$ . The measured time sequences of optical density changes were fitted for all the excitation energies for different ZnO films. Apart from other processes, stimulated emission is expected to depend critically on the excitation energy. For this reason, the results of simulation for E857 are presented in the following sections since it exhibits considerably higher stimulation emission. Key distinctions in the intensity dependence of other film thicknesses are briefed as well towards the end of this section. Along with the regular varying parameters which will be mentioned in the relevant sub-sections, an extra Gaussian curve was introduced at  $400\text{nm}$  to account for the scattering contribution.

### 5.4.1 Linear nature of carrier excitation

In the model, the amplitude, width as well as the centre wavelength of carrier excitation contribution were varied. Figure 5.25 shows the temporal variation of all the three parameters of carrier excitation contribution at all the four excitation energies for early delay times. It can be seen from the figure that as the pump energy is increased, the amplitude of this contribution increases but there is no significant change in its temporal evolution. The carrier excitation at the lowest energy of  $7.5\mu\text{J}$  shows rather small contribution and rapidly decays back within  $0.5\text{ps}$ . Figure 5.25(c) shows maximum value of the area plotted as a function of pump energy. A linear correlation between area under carrier excitation contribution and excitation intensity is observed. Apart from amplitude variation, the width of this contribution does not display any remarkable trend in its time evolution for different pump energy.

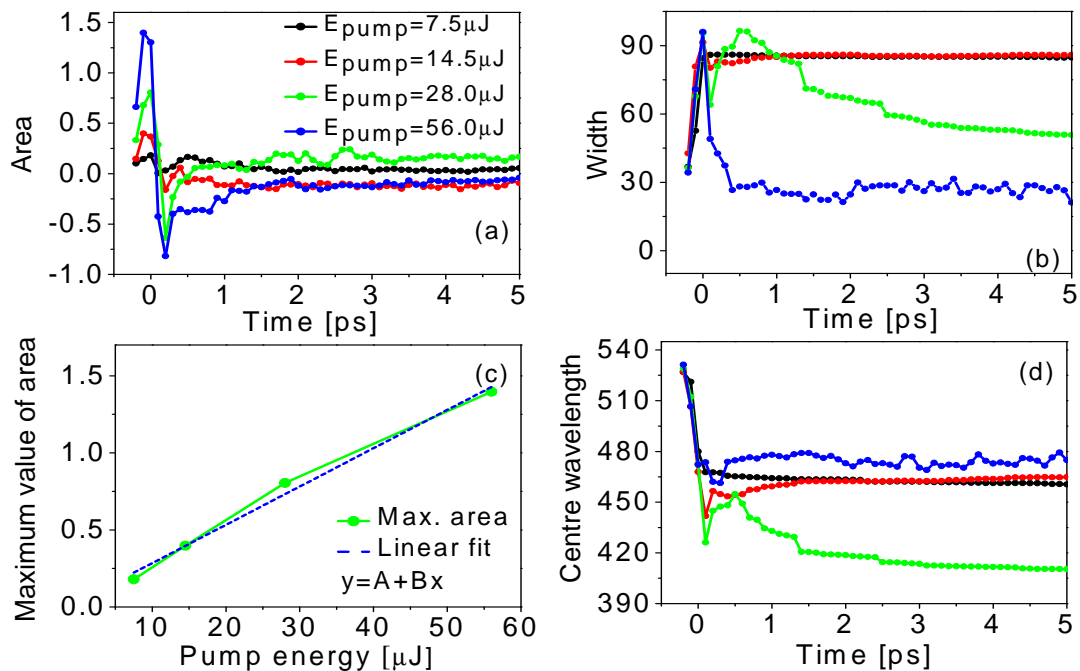


Figure 5.25 Time evolution of carrier excitation contribution at different excitation energies for E857

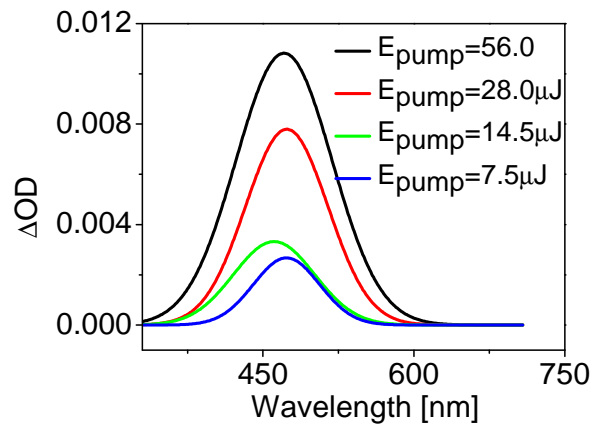


Figure 5.26 Spectral evolution of carrier excitation contribution at different excitation energies for E857

Figure 5.26 shows the spectral evolution of carrier excitation contribution with increasing pump energy. With increasing pump energy, the carrier excitation increases in amplitude accompanied by significant spectral broadening. From about 60nm for the lowest pump energy of 7.5 $\mu$ J, the broadening is as wide as 95nm for 56 $\mu$ J. Upon stronger excitation, more vacancies are created in the intermediate defect levels consequently leading to higher induced absorption increase. The widening of the spectral width of this contribution indicates that larger number of defect levels is depleted at higher pump energies.

#### 5.4.2 Excitation energy dependence of exciton bleaching

In order to investigate the influence of pump energy on exciton bleaching contribution, excitons-A and C amplitudes were varied in the optimization routine. As already mentioned in chapter 3, exciton B=0 for E857. Figure 5.27 shows the decay behaviours of both the exciton contributions at different excitation intensities for E857. It can be seen that exciton-A and C have the highest population for the highest pump energy. These results reveal that the rate of charge carrier recombination decreases with increasing excitation photon energy. Between exciton-A and C, carriers in exciton-C

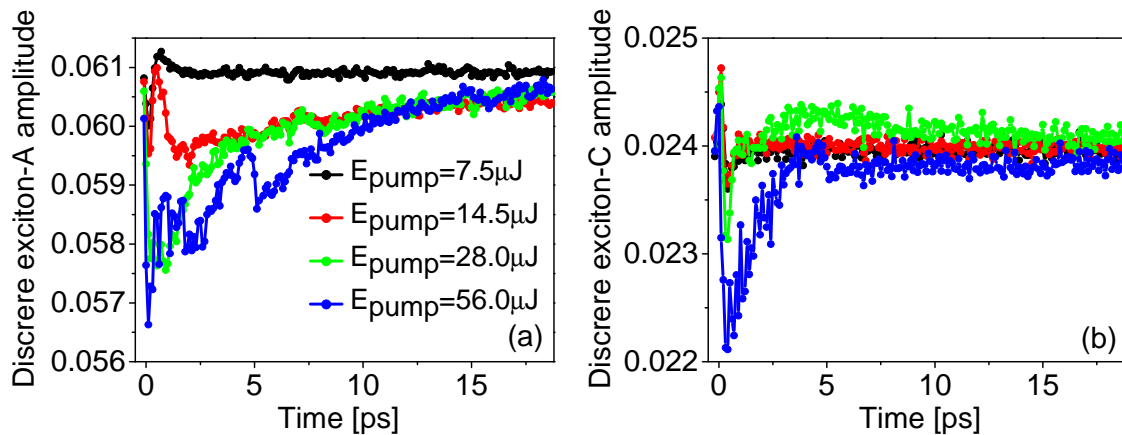


Figure 5.27 Temporal evolution of exciton contributions at different pump energies for E857

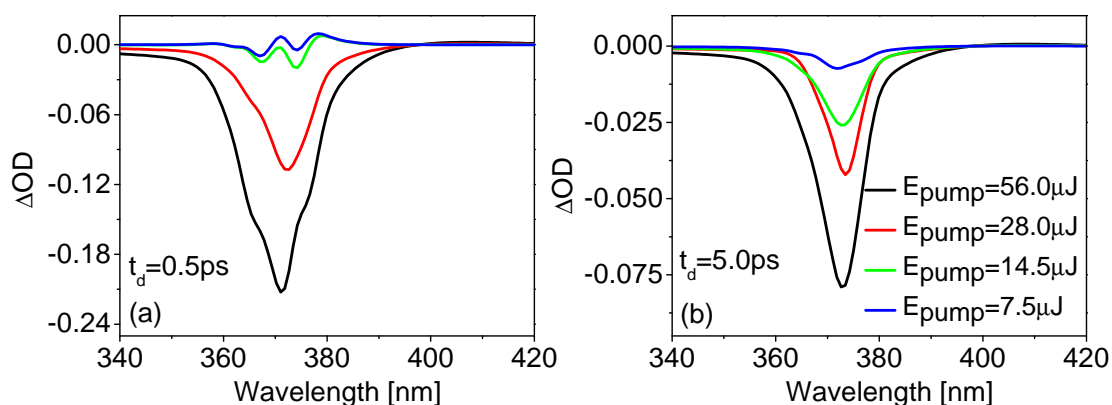


Figure 5.28 Spectral variation of discrete exciton bleaching with increasing excitation energies for delay times (a) 0.5ps and (b) 5ps

recombine faster than exciton-A. As energy increases, the slower component becomes slower in both the exciton bleaching while the faster one doesn't seem to have any significant influence of the pump energy. Discrete exciton-A decays on more than 20ps timescale for higher energies. At lower energies, the relatively smaller population of excitons rapidly decays back to the ground state. Figure 5.28 shows traces of the modelled spectral variation of discrete exciton bleaching contribution for different excitation intensities for E857 at 0.5ps and 5.0ps respectively. An order of magnitude difference in the vertical scales for the both the plots should be noted. The excitation energy critically influences the transient optical density profile. A stronger bleach of all the exciton bands is observed with increasing pump energies. For the lowest energy of 7.5 $\mu$ J, the contribution broadens till 360nm whereas the spread is as far as 340nm for the highest 56.0 $\mu$ J pump energy. At low excitation energies, the contribution from exciton-C is rather small. With increasing intensity, the amplitude of discrete exciton bleaching increases nonlinearly. This shows that the exciton bleaching is a nonlinear process since its absorption coefficient depends on the intensity of light. From the energy dependent measurements, it is established that the spectral broadening of the blue wing of exciton bleaching contribution is purely an intensity dependent effect in ZnO.

### 5.4.3 Non-linear nature of stimulated emission

The simulated time sequences of stimulated emission were obtained by varying its area as well as width while the centre wavelength was kept fixed at 390nm. Figure 5.29 shows the temporal evolution of the area under stimulated emission. The total area under stimulated emission increases with increasing energy and exhibits fast and slow contributions. As the energy is increased, the density of excitons increases and so does the exciton-exciton interaction. Consequently, the efficiency of stimulated emission goes up. The fast component rises faster with increasing excitation intensity. In contrast, the slow component reaches its peak amplitude slower as the pump energy is increased. However, it decays faster for higher pump energies. The appearance of fast contributions, on very similar timescale, and slow ones in both exciton bleaching and stimulated emission strongly suggests the involvement of two types of prevailing

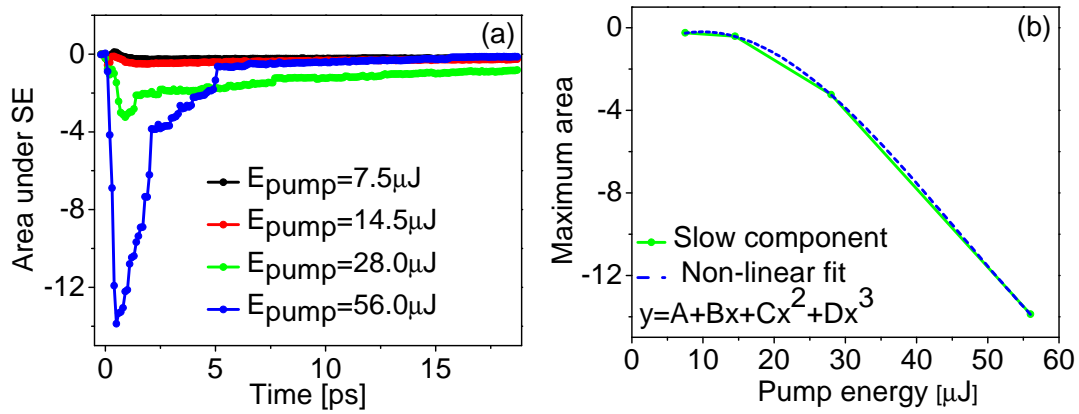


Figure 5.29 (a) Stimulated emission for different excitation energies for E857 (b) Non-linear fit to the maximum area of stimulated emission

interrelated relaxation mechanisms in the carrier decay. These relatively short decay lifetimes suggest that the carrier dynamic behaviours are significantly affected by fast nonradiative processes. In figure 5.29(b), maximum area of stimulated emission is plotted as a function of pump energy. A cubic fit to the curve reveals that the stimulated emission exhibits nonlinear dependence with the excitation energy. At low powers, the density of excitons is small and the separation between excitons is large. Hence, the exciton-exciton scattering is very low.

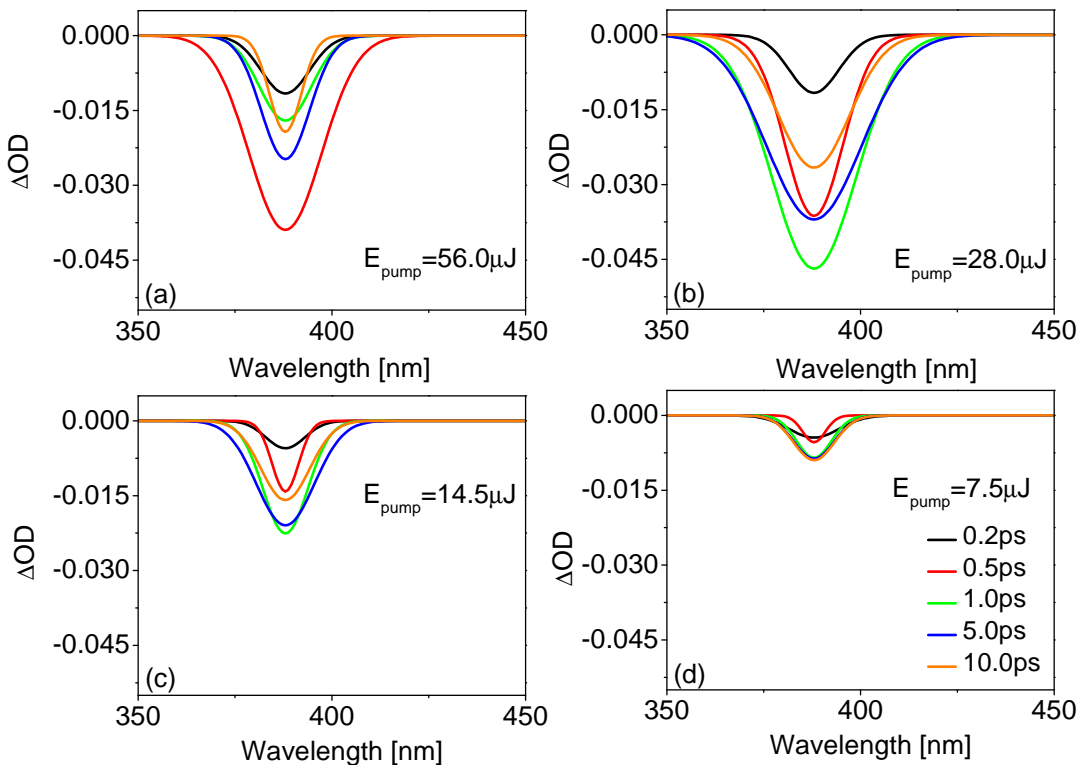


Figure 5.30 Stimulated emission for different excitation energies for E857



### 5.4.4 Excitation energy dependence of interference contributions

To generate the oscillatory behaviour between 400-600nm, continuum exciton-A and real UV resonance term are varied in the optimization routine. Figure 5.31 plots their temporal evolution at different pump energies. The interference modulations experience higher amplitudes for higher excitation energies. If the excitation is weak, refractive index modulations are small. On the other hand, higher pump energy causes higher modulation of refractive index in ZnO. The time evolution of  $A_{ca}$  and  $\epsilon_{1off}$  show a fast component on less than 1ps timescale followed by a slower decay.

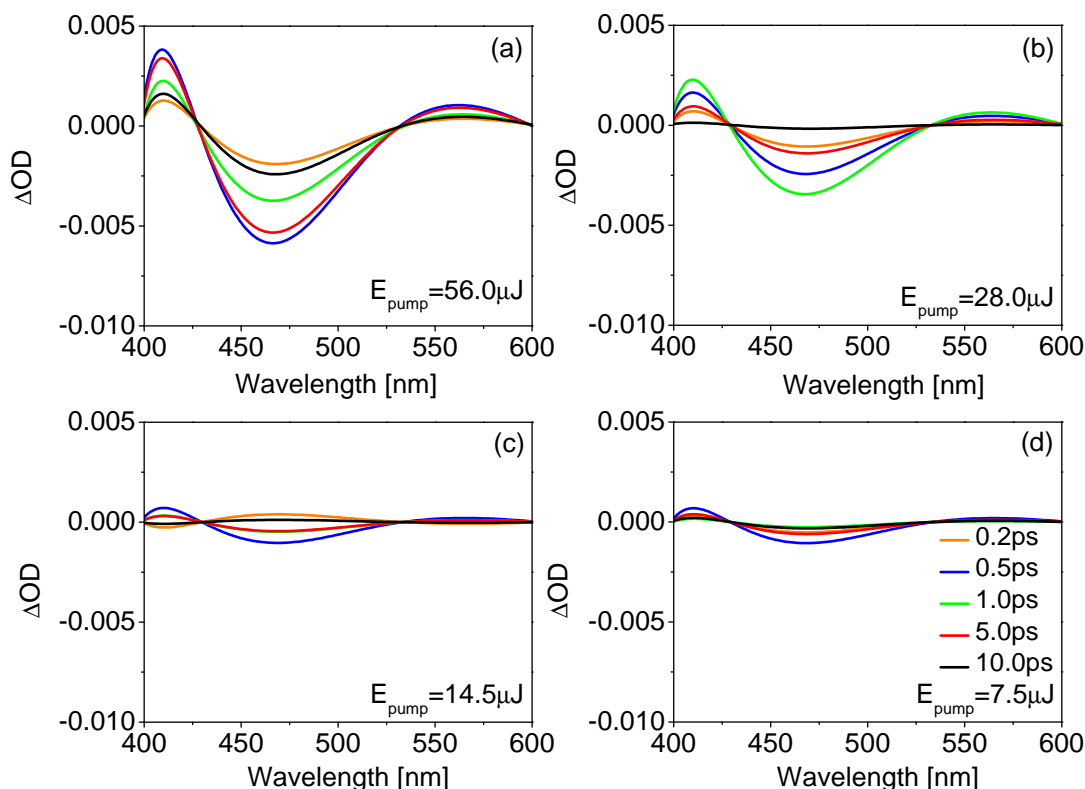


Figure 5.31 Interference contributions for different pump energies for E857

### 5.4.5 Bleaching at fundamental wavelength for different pump energies

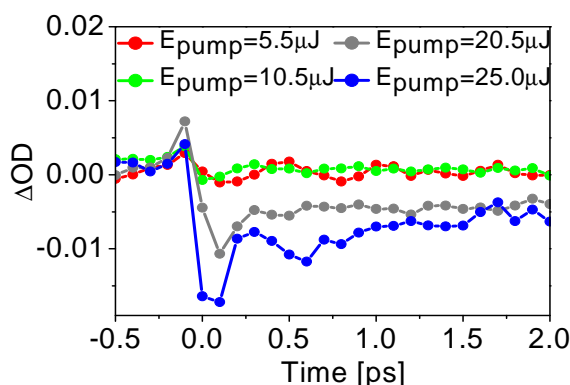


Figure 5.32 Transmission increase at 400nm for E1962 at different excitation energies

E1962 and E1963 exhibit a rapid change in optical density at 400nm for very early delay times which increases with increasing excitation energy. In figure 5.32, for E1962 the temporal variation of 400nm wavelength is plotted at different pump energies. This contribution increases with increasing pump energy. With increasing pump energy, the amount of depleted carriers being excited to the conduction band increases, leading to higher transmission increase at 400nm.

### 5.4.6 Pump energy dependence of other ZnO films

Figure 5.33 shows the difference optical density traces of various pump intensities ( $\lambda_{\text{pump}}=400\text{nm}$ ) for E1964, E1963 and E1962 for two delay times of 0.0ps and 0.5ps. The mechanisms that are enhanced with increasing pump energy are different for different film thickness. The samples E1964 and E1963 display stronger excitonic interactions at higher pump fluence. The left shoulder of the bleaching peak significantly broadens upto 340nm in the ultraviolet region with increasing excitation energy. The spread of the right wing of exciton bleaching is relatively lesser. For

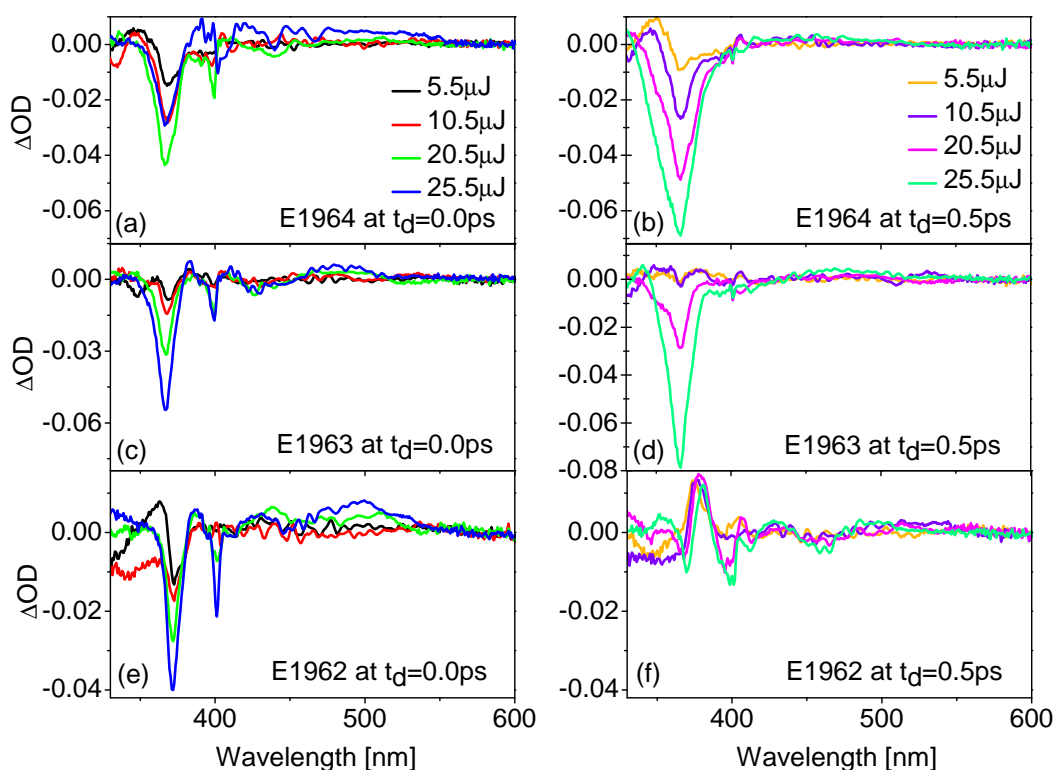


Figure 5.33 Difference optical density traces at different pump intensities for E1964, E1963 and E1962 for two delay times 0.0ps and 0.5ps respectively

E1962, the bleaching peak increases in amplitude with increasing pump energy without any significant spectral broadening. At high energies, all three excitons-A, B and C bleach in E1964 and E1963 whereas the exciton C does not play significant role in the dynamics for E1962. The excitons decay rate increases from E1964 to E1962. The exciton-B and C decays on 20ps timescale while exciton-A is longer lives and decays on 50ps time scale. For early delay times (0ps), figure 5.33 depicts higher amplitudes of the carrier excitation related short-lived absorption increase at around 500nm with

increasing excitation energies. However, as evident from figure 5.33(f), for E1962 the 380nm contribution doesn't seem to be influenced by pump energy.

### **Summary**

The effect of excitation energy on time resolved dynamics in ZnO films was studied extensively by performing energy dependent measurements on them. The results show a distinct excitation intensity dependence of the below-bandgap carrier dynamics in ZnO. Carrier excitation contribution exhibits a linear correlation with pump energy. It was found that the stimulated emission exhibits a nonlinear dependence on the excitation energy. The transient optical density spectra reveal higher occupation of all three excitons for higher intensities which lead to broadening of the overall exciton bleaching contribution. The discrete exciton-C has maximum population at higher energies. For lower energies, exciton-A and B bleaching are the dominant contributions. The rate of the decay of excitons depends on the excitation energy. Higher pump energy also induces stronger variation in the refractive index which results in stronger interference oscillations. The rapid change in optical density at 400nm increases with increasing pump energy.

## 5.5 Comparison of carrier dynamics in different ZnO films

Time resolved pump-probe experiments were performed on ZnO films having different thicknesses. A set of five ZnO films with thicknesses 98nm (E1964), 227nm (E1963), and 476nm (E1962) on *a*-plane sapphire and 264nm (E857) and 458nm (E859) on *c*-plane sapphire were investigated. In order to minimize saturation effects, the energy of the 400nm excitation pulse was kept fixed at moderate value of 15.2 $\mu$ J during the measurements on E1964, E1963, and E1962. Separately, experiments were done on E857 and E859 with pump energy of approximately (7mW after SHG). Figure 5.34 and 5.35 show the spectral variation of the experimental transient optical density at selected delay times for both the sample sets. The exciton bleaching centred around 375nm is observed for all the ZnO films. Its low wavelength wing is broadened for E1964 and E1963 as compared to E1962. The spectral variation between 400-600nm is more prominent for the thicker samples as compared to thinner ones. There is an additional contribution observed for E1962, clearly seen at delay time 0.3ps where the spectral profile at 380nm changes from transmission increase into positive rising absorption increase at early delay times. It first shifts to the blue side and then slightly to the longer wavelengths. This contribution seems to be absent or at least diminished in E1963 and E1964. The sample E1963 shows large positive peak at 400nm due to scattering in the sample.

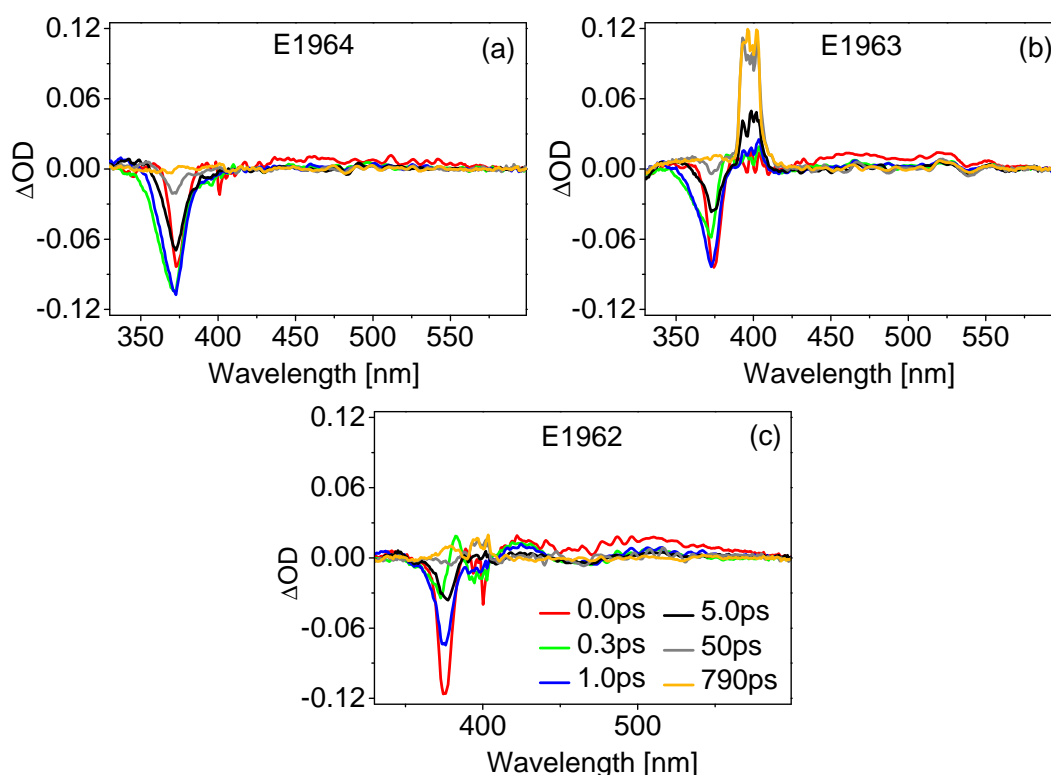


Figure 5.34 Transient optical density spectra for E1964, E1963 and E1962

The stimulated emission is observed to be very low, almost negligible in all the three films of E19xx series grown on *a*-plane sapphire. In sharp contrast, films of E8xx series grown on *c*-plane sapphire exhibit much higher stimulated emission centred around 390nm as evident from figure 5.35. Though not present in the data set shown, the early time 380nm absorption increase is observed in E857 and E859 as well, more clearly

visible at low excitation intensity. At moderate to high intensities however, this contribution seems to be overshadowed by increased stimulated emission around 387nm due to its spectral proximity. Moreover, like in E1962, there is no significant spectral broadening of the left shoulder of the bleaching peak in both the films. The sharp positive peak around 400nm is due to the scattering of pump beam in the sample. The interference oscillations as well as carrier excitation contributions experience higher amplitudes for E859 as compared to E857. Overall, it is observed that except for difference in stimulated emission, all other processes in the time resolved spectra of E8xx films possess similar characteristics observed for the E19xx series.

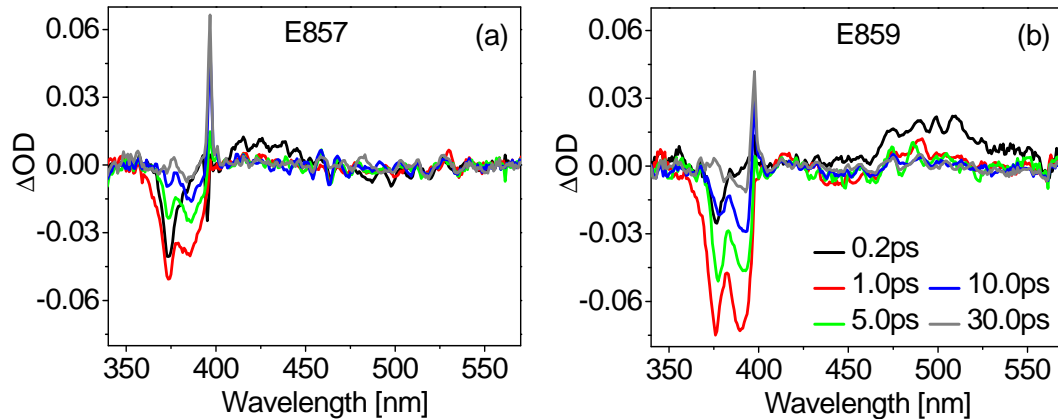


Figure 5.35 Transient optical density spectra for E857 and E859

The time dependent spectral changes presented above were modelled using the Levenberg Marquardt optimization procedure. The following sections demonstrate the thickness dependence of interferometric modulations and stimulated emission. A comparative study of other contributions in different ZnO films is presented in the end.

### 5.5.1 Thickness dependence of interferometric modulations

For E1964, E1963, E857 and E1962, the oscillatory behaviour was modelled by variation of continuum exciton-A,  $A_{ca}$  and the real constant term,  $\epsilon_{1off}$ . Figure 5.36 shows the modulations produced in the time resolved spectra at selected delay times for these films. As the film thickness increases from 98nm upto 476nm, the oscillations become most prominent. The period of oscillation increases with the film thickness. It is discussed in chapter 3 that the interference from a thin film is dependent on the thickness of the film and that the period of oscillations decreases with increasing thickness. Figure 5.36 evidently shows that the period of modulations increases with the increase in sample thickness. This proves more conclusively that the modulations observed between 400-600nm indeed originates due to interference change and that the correct parameters are varied in the optimization routine to explain these modulations. The modulation in refractive index by the excitation pulse is higher for thicker samples which results in higher oscillatory behaviour. The AFM images of the investigated ZnO films reveal that the samples not perfect interferometer.

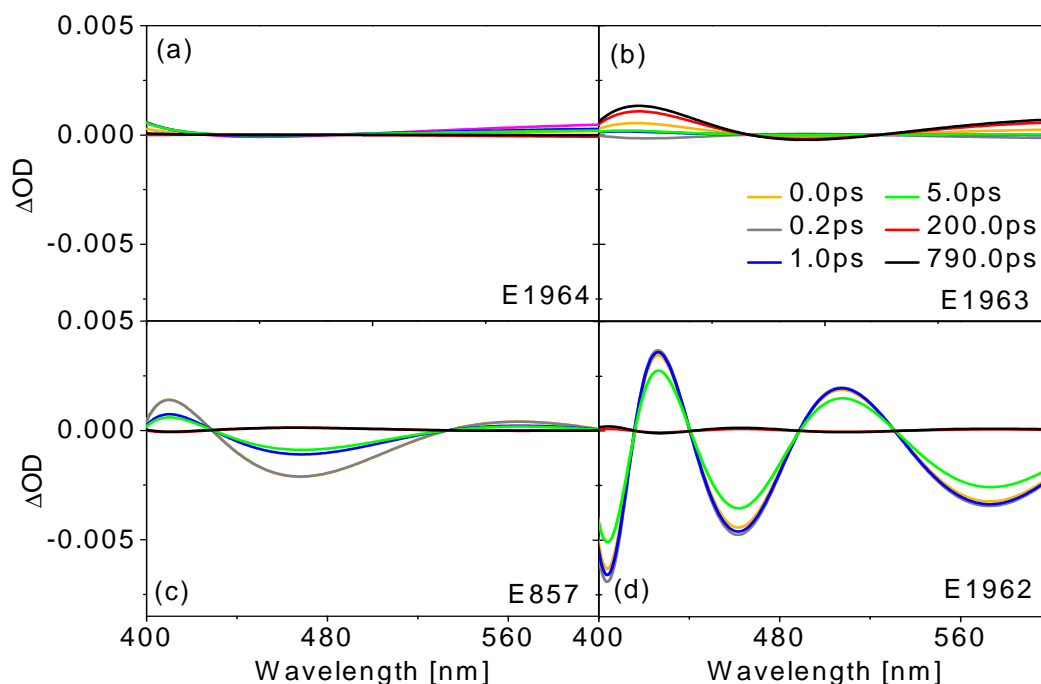


Figure 5.36 Interferometric oscillations for E1964, E1963, E857 and E1962

In figure 5.37, the amplitudes of continuum exciton-A and constant UV resonance term is plotted as function of delay time. The amplitudes have been normalised for better comparison of their temporal behaviour. The amplitudes of  $A_{ca}$  and  $\epsilon_{1off}$  do not exhibit any significant distinction in the temporal behaviour with varying film thickness. This proves that the rate of decay of interference contribution in the time resolved spectra is independent of the film thickness.

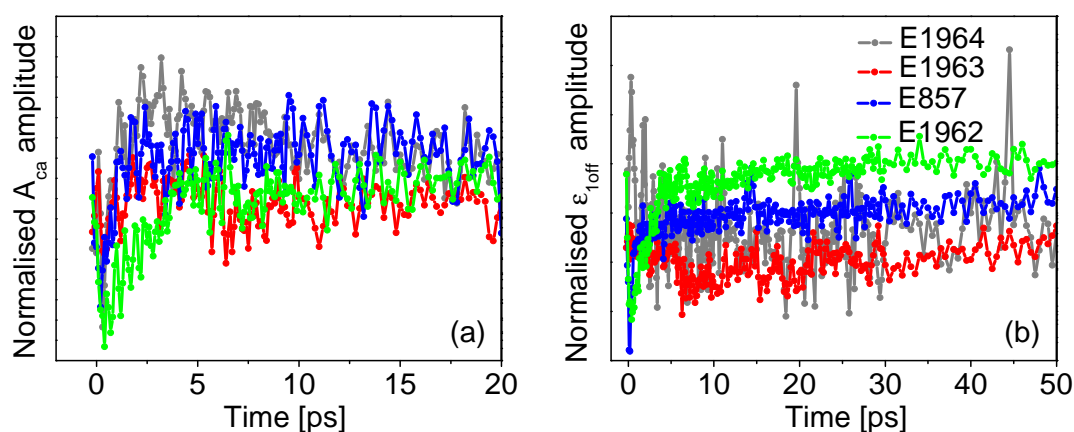


Figure 5.37 Time evolution of  $A_{ca}$  and  $\epsilon_{1off}$  for different film thicknesses

## 5.5.2 Thickness dependence of stimulated emission

The modelled stimulated emission contribution for E857 and E859 respectively are presented in figure 5.38(a) and (b) respectively. The 458nm thick sample E859 exhibits larger amount of stimulated emission as compared to the 264nm thin E857.

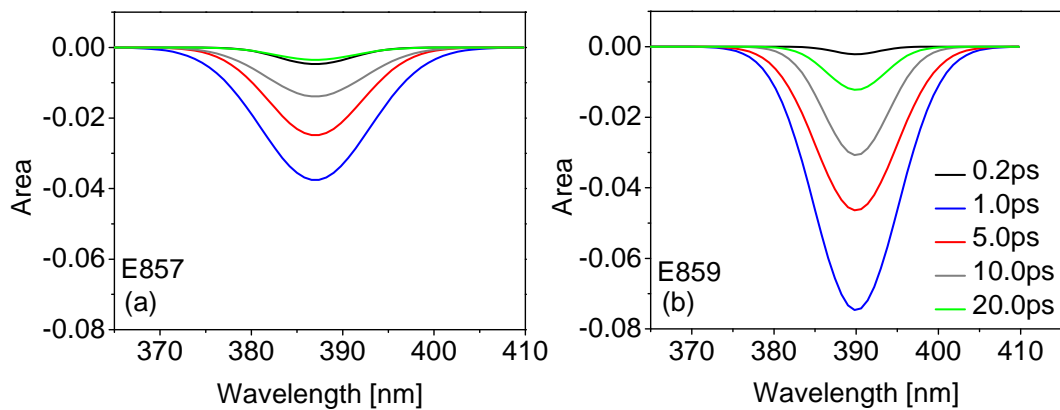


Figure 5.38 Spectra evolution of stimulated emission for E857 and E859

With an increase in thickness from 264nm to 458nm, the stimulated emission too increases approximately two orders of magnitude. Qualitatively, the thickness dependence of stimulated emission can be explained by increase in the number of emitters with the increase in the excited volume of the sample. It is also reported in the literature that the emission rate decreases significantly for thinner films [4].

As mentioned in the beginning of this section that higher stimulated emission is observed for E857 and E859 in the experimental time resolved spectra whereas E1964, E1963 and E1962 exhibit almost negligible stimulated emission. This stark contrast may be connected to the differences in the size of nanostructures and the grain sizes in these two sets of films. The influence of the size of nanocrystal and grain boundaries is reported in the literature [17,18,19]. Kawasaki et al and Zo et al investigated the effects of nanocrystal size on stimulated emission in ZnO thin films fabricated on c-plane sapphire substrates. The films having small nanocrystal size of about 50nm showed excitonic SE as well as SE from EHP. Unlike EHP induced SE, the exciton-exciton scattering induced SE was not present in the films having larger nanocrystal size. They concluded that there is an optimum hexagonally shaped microcrystallite size of  $(50\text{nm})^3$  for observing exciton-exciton scattering induced SE. Investigating similar results, Ohtomo et al argued that excitonic SE is due to the giant oscillator strength than can occur in high quality nanocrystals with dimension larger than the exciton Bohr radius ( $\sim 2\text{nm}$ ), but smaller than the optical wavelength (390nm). For large gain samples, the exciton superradiance effect becomes weak such that exciton-exciton collision process should not occur. Thus, the grain boundaries between nanocrystals are considered to serve as barriers resulting in the confinement of excitons in nanocrystals.

### 5.5.3 Differences in other contributions for different ZnO films

#### 5.5.3.1 Carrier excitation

The temporal evolution of the carrier excitation contribution is plotted in figure 5.39 for E1964, E1963, E857 and E1962. The early time rise and rapid decay of carrier excitation show very similar behaviour for all the thicknesses. It is observed that except for change in amplitude, the first 0.5ps decay profile of excitation of carriers is uninfluenced by the film thickness. This is an expected finding since the rate at which carriers are transferred from these states to the conduction band should be independent

of the film thickness. The slow component in E19xx series after a dip at around 0.3ps again shows an upward trend while E857 decays monotonously with time. E1962 decaying on a 10ps timescale and E857 decaying on less than 4ps time scale. The life time of slower component is almost same for E1963 and E1964 samples.

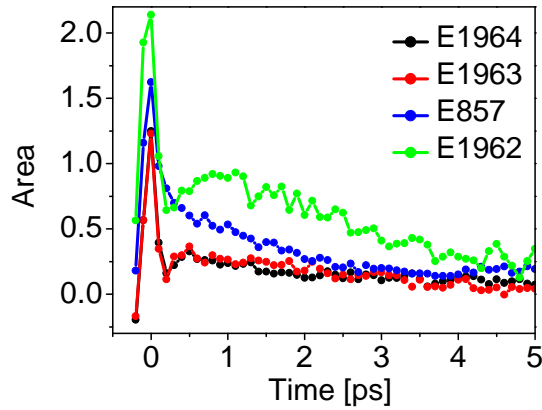


Figure 5.39 Temporal evolution of carrier excitation for E1964, E857, E1963 and E1962

### 5.5.3.2 Transmission increase at 400nm

The experimental transmission increase at 400nm for E1962 and E1964 is plotted in figure 5.40(a). The thicker E1962 sample shows higher bleaching at 400nm for very early delay times than the thinner E1964. This can be correlated with the discussion presented in section 5.2.2 regarding the carriers being excited from defect levels attributed to oxygen vacancies. With the increase in sample thickness, the volume excited by the pump pulse increases. This leads to more number of excited carriers being transferred to the conduction band which increases the change in optical density at 400nm. The sample E1963 could not be considered for this comparison since it shows very large scattering in the time resolved spectra as can be seen in figure 5.40(b). This made it difficult to observe any optical density changes.

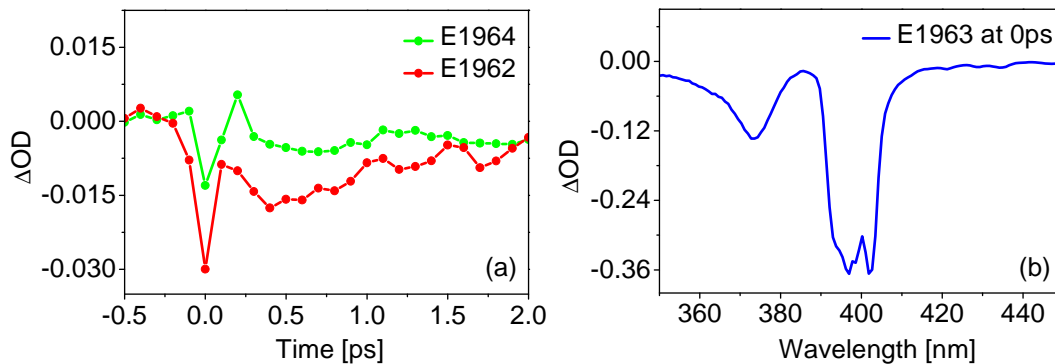


Figure 5.40 (a) Temporal evolution of change in optical density at 400nm for E1964 and E1962 (b) Spectral evolution of E1963 at 0ps



### 5.5.3.3 Exciton bleaching in different ZnO samples

In figure 5.41, the temporal evolution of excitons-A, B and C is plotted for E1964, E1963 and E1962. For better comparison, the amplitudes for different films thicknesses have been scaled since the individual values of the parameters were far part. It is observed that the very early times fast decay dynamics of the exciton contribution is independent of the film thickness. However, the slower component of the bleaching contribution becomes faster with increasing film thickness. The carriers in exciton levels A and B recombine faster for thicker sample but no clear any trend of the effect of thickness on lifetime of exciton-C decay can be traced.

In figure 5.41, the spectral variation of the overall bleaching contribution for selected times is plotted for different film thicknesses. The transient exciton bleaching around 375nm shows modification in the spectral pattern for different film thickness. As the thickness reduces from 476nm to 98nm, the blue wing of the bleaching contribution bulges out and broadens more toward the UV. The table in figure 5.41 shows the maximum percentage change in the excitons-A, B and C for all the three films. Overall, it is evident that thinner ZnO films display more exciton-bleaching while it reduces as the film becomes thicker. The maximum transient population of exciton-A is reduced from approximately 25.2% in ZnO-98nm to 17.5% and 14.5% for E1963 and E1962 respectively. Approximately 23.4% of exciton-A levels are occupied in E1964 which significantly reduces to 5.9% and 1% as the thickness increases through E1963 to E1962. The population of exciton-C level exhibits the most dramatic variation with as much as 50.7% population in E1964 which drastically reduces to 2% for the thickest E1962.

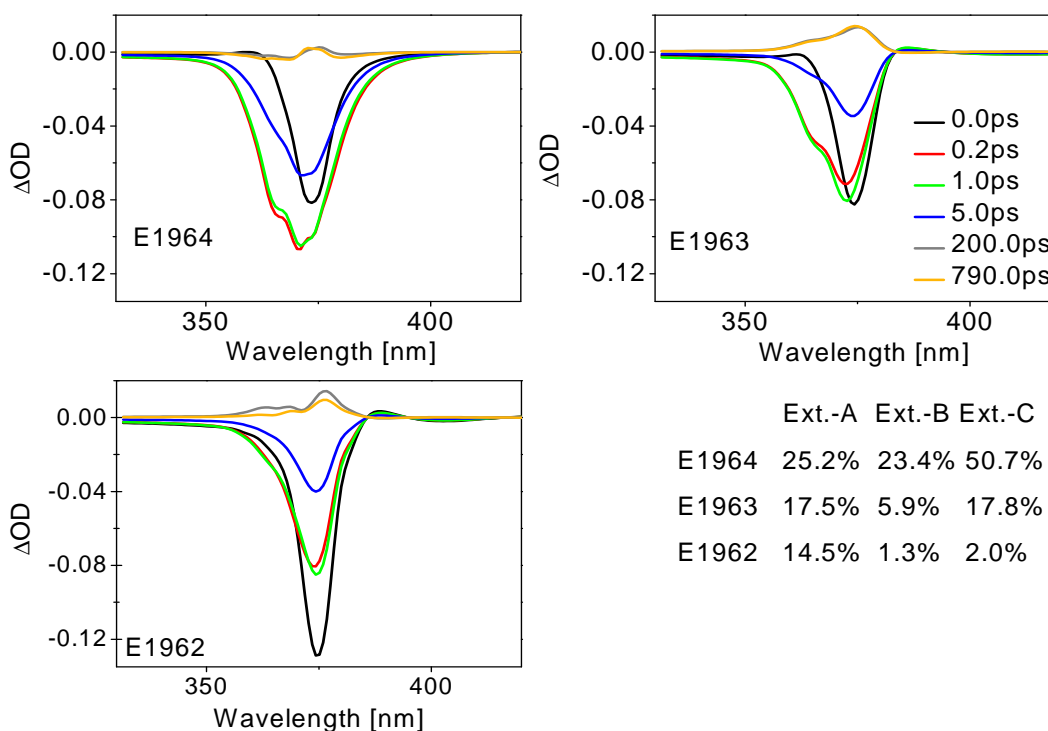


Figure 5.41 Spectral evolution of exciton bleaching for E1964, E1963 and E1962

The differences in spectral as well as temporal variation of exciton bleaching for different films may be a consequence of differences in the structural properties of the individual films. It is definitely not a result of varying film thickness.

#### 5.5.3.4 Absorption increase at 380nm

The 380nm absorption increase is largely a thickness dependent effect since it is observed for E1962 and E1963. In thinner E1964 sample, this effects seems to absent or atleast diminished. It is possible to fit this 380nm peak by bandgap variation in the optimization routine but this approach doesn't lead to a relevant interpretation of the physics behind the process since the optimization routine increases the bandgap to fit the peak. Contrary to this, literature reports show bandgap renormalization effects manifest themselves by reducing the bandgap of the material. Hence, instead of varying the bandgap, a Gaussian curve was introduced in the model at 380nm. The width as well as amplitude was optimized while the centre wavelength was kept fixed at 380nm.

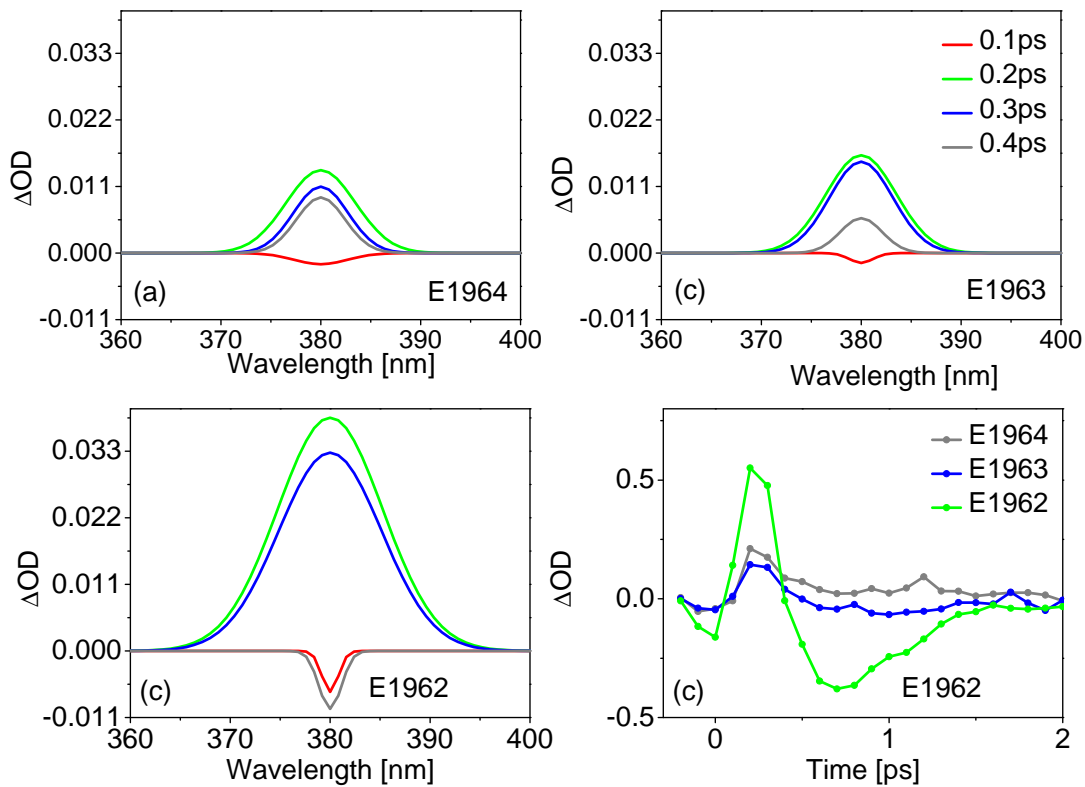


Figure 5.42 The absorption increase contribution at 380nm for different thickness of ZnO and its temporal variation

Figure 5.42 shows the temporal evolution of the amplitude of the 380nm absorption increase. Thicker ZnO films show an additional absorption increase at 380nm for very early delay times. It is evident from the figure that this contribution rises and decays rapidly on less than 500fs timescale. Since it starts at 0.2ps indicates that it is an induced process. Another aspect is that this 380nm effect is very fast and present for very early times  $\sim 0.3-0.5$ ps.

## Summary

The time resolved measurements performed on ZnO films of different thicknesses exhibit systematic thickness dependence of modulations between 400-600nm with the strength and period of oscillations increasing with sample thickness. It confirmed the origin of these modulations as arising from modification in interference pattern brought about by change in refractive index of ZnO by the intense 400nm excitation pulse. The stimulated emission increases with increase in film thickness.

The basic processes of carrier excitation, exciton bleaching and interference contributions are found to be present in all the ZnO films which inherently have structural differences between them. However, the non-identical nature of these films manifests some differences in spectral amplitude and time resolved dynamics in them. The structural properties of the ZnO films is found to influence the stimulated emission with films grown on *c-plane* sapphire exhibiting more efficient emission while those grown on *a-plane* sapphire display almost negligible stimulated emission. The dynamical behaviour of excitation of carriers centred around 500nm remains uninfluenced by the thickness. The exciton bleaching contribution centred around 375nm exhibits differences in spectral broadening for difference. The transmission increase at 400nm for very early times increases with film thickness further validating the interpretation of carrier dynamics done in section 5.1. The additional absorption increase at 380nm is observed only for thicker films E1962, E857 and E859. The exact background of this contribution and its correlation with film thickness are not clear. The observed differences in spectral as well as temporal evolution of contributions are outcome of rather complex combination of not only thickness but also the structural properties in the investigated ZnO films. In the future work, these differences can be addressed by careful investigation of the structural properties of ZnO films.



## **Summary and outlook**

The ultrafast carrier dynamics in ZnO films were investigated by time resolved transmission pump probe spectroscopy. The optical response provided the fundamental information about the relaxation mechanisms in ZnO films. A novel approach to resolve the carrier dynamics from the time resolved pump probe data has been developed which constitutes both the intrinsic dielectric function as well as extrinsic (non-equilibrium) induced processes. The ellipsometric model could successfully explain the time dependent spectral changes in the time resolved spectra.

The elementary absorption of the 400nm, 150fs excitation pulse transfers carriers from defect states located within the bandgap to the conduction band, giving rise to bleaching at 400nm for early delay times. The depletion of the defect levels induces an increase in absorption which manifests itself in the time resolved spectra as a broad and rather weak absorption increase centred around 505nm. It rises and decays on ~600fs time scale. The initially displaced carriers in the conduction band relax rapidly to the bottom of the band. The carrier excitation leads to the bleaching of discrete exciton-A at 375 nm. With the passage of time, the carrier density in the exciton levels increases, so much so that they begin to interact with one other. The exciton-exciton scattering finally leads to stimulated emission centred at ~390nm. The stimulated emission rises slowly on ~1ps timescale. The time evolutions of both exciton bleaching as well as stimulated emission exhibit non-exponential decay with fast and slow contributions. Overall, the exciton bleaching and stimulated emission decays on ~50ps and ~200ps respectively. Furthermore, it was found that changes in the refractive index of the sample induced by the excitation pump pulse generates oscillatory behaviour between 405-600nm in the time resolved spectra. In addition, analysis of the temperature dependence of dielectric function of ZnO revealed that the longer time nondecaying 380nm absorption increase upto 600ps in the time resolved spectra is a manifestation of thermalization of the sample.

The optical response after excitation with different wavelengths provided fundamental information about the relaxation mechanisms in the ZnO films and successfully verified the proposed interpretation about the nature of excitation mechanisms and exciton bleaching processes. The excitation wavelength dependent measurements showed the primary excitation from defect levels always occurs with all three pump wavelengths. This absorption increase around 505nm increase with increasing pump wavelength but no significant influence on its temporal behaviour is traced. A rapid transmission increase at the excitation wavelengths could be observed after excitation with 400nm and 409nm. The investigation also revealed that apart from

indirect excitation, some direct formation of excitons also takes place with 391nm excitation wavelength. However, excitons are indirectly created after pumping with 400nm and 409nm respectively. The recombination decay lifetime of excitons show slight pump wavelength dependence. Additionally, the studies also revealed that in thicker ZnO samples, a fast rising absorption increase is present at around 380nm contribution which depends significantly on the excitation wavelength. The true background of this contribution could not be ascertained.

Detailed knowledge about the nature of various processes in the dynamics was gleaned by performing excitation energy dependent experiments on ZnO films. The analysis shows a distinct excitation intensity dependence of the below-band-gap carrier dynamics in ZnO. The rapid change in optical density at 400nm increases with increasing pump energy. Carrier excitation contribution exhibits a linear dependence on the pump energy. The transient optical density spectra reveal the bleaching from all three excitons for higher intensities which lead to broadening of the overall bleaching contribution. The discrete exciton-C has maximum population at higher energies. For lower energies, exciton-A and B bleaching are the dominant contributions. It was found that the stimulated emission exhibits a nonlinear dependence on the pump energy. The rapid change in optical density at 400nm increases with increasing pump energy. Higher pump energy also induces stronger variation in the refractive index which results in stronger interference oscillations.

The time resolved measurements performed on ZnO films of different thicknesses exhibit systematic thickness dependence of modulations between 400-600nm with the strength and period of oscillations increasing with sample thickness. It confirmed the origin of these modulations as arising from modification in interference pattern brought about by change in refractive index of ZnO by the intense 400nm excitation pulse. The stimulated emission also increases with increase in film thickness. The basic processes of carrier excitation, exciton bleaching and interference contributions are found to be present in all the ZnO films which inherently had structural differences between them. However, the non-identical nature of these films manifests some differences in strength of processes and their dynamics. The observed differences in spectral as well as temporal evolution of contributions are outcome of rather complex combination of not only thickness but also the structural properties in the investigated ZnO films. In particular, the structural properties of the ZnO films is found to influence the stimulated emission with films grown on *c-plane* sapphire exhibiting more efficient emission while those grown on *a-plane* sapphire display almost negligible stimulated emission. In the future work, these differences should be addressed by careful investigation of the structural properties of ZnO films.

The current investigation presented in this thesis renders a thorough understanding on the relaxation mechanisms that govern the ultrafast carrier dynamics in ZnO films upon excitation with femtosecond laser pulse. These findings serve as a guide for more refined experiments to study the influence of defects on the carrier dynamics of ZnO to be able to more precisely control its electronic properties from applications point of view. Though there still remain some open questions that need to be addressed. The investigation revealed that the structure of the films and more importantly the defects in ZnO play a pivotal role in its carrier dynamics. The results obtained point to the requirement of further characterization of defects in more detail. There is a strong indication to refine the dielectric function of ZnO by proper inclusion of defects states as well other non-equilibrium components, to be able to model its time

resolved dynamics more precisely. Femtosecond time resolved spectroscopy in conjunction with ellipsometry is required for further analysis. Also, an in-depth characterisation of structural properties in ZnO films must be done through a variety of techniques like TEM, AFM, DLTS to better control these parameters in order to achieve a more complete understanding of the dynamic properties of charge carriers in ZnO films.

Also, the physical background of interference oscillations is not completely understood. One of the challenges encountered was that these oscillations exhibit a rather small amplitude in time resolved transmission experiments. In order to study them in more detail, one of the possibilities would be to perform these measurements in the reflection mode, instead of transmission mode. The following section shows the first results of simulations done in the reflection mode for E859. In both the modes, the amplitudes of the continuum exciton-A which is responsible for oscillations and discrete exciton-A giving rise to exciton bleaching are decreased by 5%.

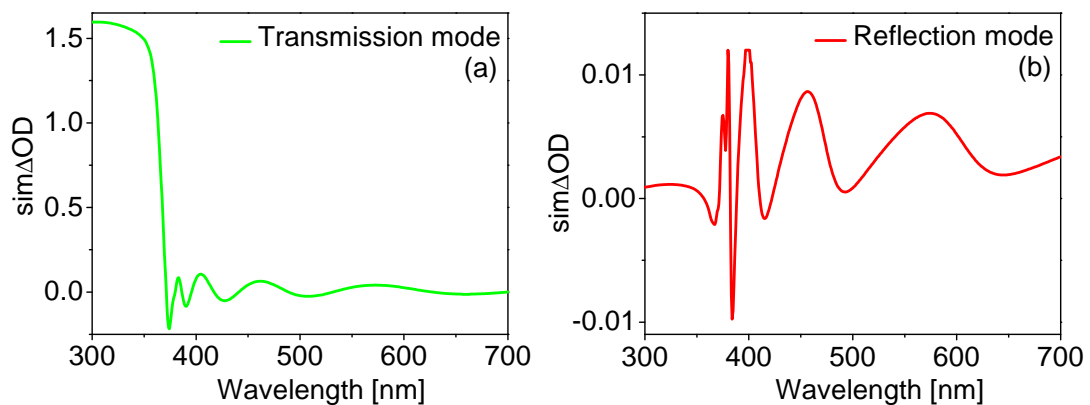


Figure 6.1 Simulations depicting spectral variation of change in optical density in transmission as well as reflection modes

It is evident from figure 6.1 that in the reflection mode, the UV resonance contribution is not as strong as in the transmission mode. The absolute amplitude of oscillations between 400-700nm is much lower in reflection than in transmission since owing to its high transparency, a very small fraction of incident light is reflected from ZnO surface. However, these results show that in reflection, the oscillations between 400-700nm are significantly enhanced relative to other contributions. This would help a great deal in analysing and finding out the origin of the interference contribution in the time resolved carrier dynamics.





## Appendix A

### Calculation of change in optical density in reflection mode

Figure A.1 schematically illustrates the paths traversed by a ray of light incident on a thin film where only emergent reflected rays are drawn. The incident light is divided into a reflected ray along AR and a ray refracted one through the thin film (ZnO layer) striking the lower interface at B<sub>1</sub>. Since the sample is transparent, only a small fraction of the incident light is reflected as the ray AR at the upper surface. The light which enters the ZnO layer suffers multiple reflections from the front and back surfaces. Thereafter, after even number of passes in the medium, an even smaller fraction emerges as reflected light (rays R<sub>1</sub>, R<sub>2</sub>, R<sub>3</sub>...). These emerging multiple reflected rays superimpose with one another giving rise to interference fringes.

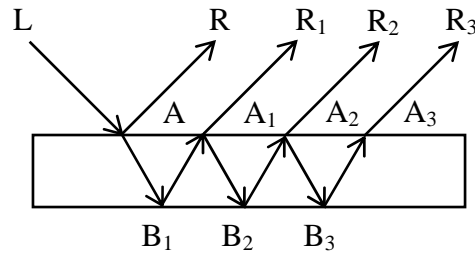


Figure A.1 Schematic depicting interference phenomena in a thin film in the reflection mode

After every two of passes through the thin film, the beam suffers an absorption loss of  $\exp(-\alpha t)$ . Therefore, the total field due to the superposition of  $p$  reflected rays is given by the expression (a.1).

$$E^d(\lambda) = \sqrt{r} - \sqrt{r}(1-r)e^{2i\delta}e^{-\alpha t} \left[ 1 + re^{2i\delta}e^{-\alpha t} + \dots + r^{p-1}e^{2(p-1)i\delta}e^{-(p-1)\alpha t} \right] \quad (\text{a.1})$$

The resultant reflected intensity is given by equation (a.2).

$$R_p(\lambda) = E^d(\lambda) \cdot E^d(\lambda)^* \quad (\text{a.2})$$

Since the final expression is very big, it has been divided into four expressions as written in equations (a.3) – (a.6).

$$R_{ap}(\lambda) = \frac{r \cdot \left[ \left( 1 + e^{-\alpha t} \right)^2 + \left( 1 + r^p (1-r) e^{-\alpha t (p+1)} \right)^2 \right]}{\left( 1 - r e^{-\alpha t} \right)^2 + 4 r e^{-\alpha t} \sin^2(\delta)} \quad (\text{a.3})$$

$$Rb_p(\lambda) = \frac{-r \left[ 1 + 2r^p (1-r) e^{-\alpha(p+2)} + 2r^{p+1} (1-r) e^{-\alpha(p+2)} \right]}{\left( 1 - r e^{-\alpha} \right)^2 + 4r e^{-\alpha} \sin^2(\delta)} \quad (\text{a.4})$$

$$Rc_p(\lambda) = \frac{4r e^{-\alpha} \sin^2 \delta \left[ 1 + r^p (1-r) e^{-\alpha(p+1)} + r^{p+1} (1-r) e^{-\alpha(p+1)} \right]}{\left( 1 - r e^{-\alpha} \right)^2 + 4r e^{-\alpha} \sin^2(\delta)} \quad (\text{a.5})$$

$$Rd_p(\lambda) = \frac{-4r^{p+1} (1-r) e^{-\alpha(p+1)} \sin^2(p+1) \delta}{\left( 1 - r e^{-\alpha} \right)^2 + 4r e^{-\alpha} \sin^2(\delta)} \quad (\text{a.6})$$

$$R_p(\lambda) = Ra_p(\lambda) + Rb_p(\lambda) + Rc_p(\lambda) + Rd_p(\lambda) \quad (\text{a.7})$$

The change in optical density in the reflection mode can be calculated using equation (a.8)

$$\Delta OD(\lambda) = \log \left( \frac{R_{without \cdot pump}(\lambda)}{R_{with \cdot pump}(\lambda)} \right) \quad (\text{a.8})$$

# Acknowledgements

First and foremost, I would like to express my deepest gratitude to Professor Dr. Heinrich Graener, former dean of the Physics department and head of the Optics group in Martin Luther University and now the dean of the faculty of Mathematics, Informatics and Natural Sciences at the University of Hamburg, for giving me the opportunity to pursue PhD under his excellent guidance. I would like to thank him for his in-depth involvement, stimulating discussions and invaluable suggestions. His encouragement, support and sheer enthusiasm has constantly inspired me.

I would like to express my sincere thanks to PD. Dr. Gerhard Seifert for all the fruitful discussions and guidance throughout. Special thanks to Dr. Jens Lange who helped me with all the technical obstacles I faced during the course of this work. Thanks to Mrs. Ingrid Otten for preparing the samples for ellipsometry. I would also like to thank Mr. Armin Warth and Mr. Andrei Stalmashonak for their help throughout and Mr. Moritz Beleites for helping me measure AFM and microscope images of the samples. I would also like to thank all the group members for creating a congenial working environment.

I wish to express my sincere gratitude to Dr. Monika Kaempfe, former coordinator of the International Max Planck Research School for Science and Technology of Nanostructures (IMPRS) for her immense support and guidance in various aspects ranging from administrative formalities to IMPRS academic activities to personal guidance during the course of three years. I am very much indebted to her for that.

I would like to thank the collaborators of this project Professor Dr. Marius Grundmann, head of the Semiconductor Physics group at the University of Leipzig and other group members Dr. Rüdiger Schmidt-Grund, Dr. Holger von Wenkster and Mr. Chris Sturm for providing the ZnO samples used in this investigation and performing ellipsometry and TAS measurements on them. I would also like to thank them for their invaluable contribution in furthering the understanding of the time resolved results of ZnO films.

I wish to acknowledge the sponsorship of this work by Sonderforschungsbereich (SFB) 762 for three years. I am also very grateful to Professor Dr. Jürgen Kirschner, director of the Max Planck Institute of Microstructure Physics, for providing financial support for the last leg of my PhD work. I would like to thank IMPRS for giving me the opportunity to learn and expand my knowledge by offering and organising various courses, seminars and workshops.

My sincere thanks go to the former member of my group Dr. Amin Abdolvand for his great help in completing all the administrative formalities and familiarising me with everything upon my arrival in Halle. I would like to thank him, his wife Natasha, Amir and Sara for their good and enjoyable company. Many thanks to all my friends in Halle, including my German teacher Mrs. Violetta Neuber, who have created an enjoyable and pleasant social environment during the course of my stay here.

*I believe that no words or actions would suffice to express my feelings about or even acknowledge my parents' and sister's contributions in my life. Yet, I would like to take this opportunity to express my deepest gratitude to my parents and sister who have been the pillars of immense love, support and strength throughout my life. Apart from being constant sources of inspiration, their perennial encouragement and guidance has made it possible for me to accomplish my research work. I also wish to thank my grandparents and all the other members of my family for their love and support.*



# Erklärung

Hiermit erkläre ich, dass ich diese Arbeit selbständig und ohne fremde Hilfe verfasst, andere als die von mir angegebenen Quellen und Hilfsmittel nicht benutzt und die den benutzten Werken wörtlich oder inhaltlich entnommenen Stellen als solche kenntlich gemacht habe.

Eine Anmeldung der Promotionsabsicht habe ich an keiner anderen Fakultät einer Universität oder Hochschule beantragt.

Halle (Saale), den 9. Oktober 2009

Sumedha Chouthi



# Curriculum Vitae

## Personal Details

Name: Sumedha Chouthe  
Date of Birth: 24<sup>th</sup> September 1982  
Place of Birth: Bhopal, India  
Nationality: Indian  
Marital Status: Single  
Address: Schleifweg 10, 06114 Halle (Saale), Germany

## Education

2006-current      Doctorate of Philosophy in Physics  
                         Martin Luther University Halle-Wittenberg, Germany  
                         Ph.D. Thesis: “Ultrafast dynamics of ZnO films using femtosecond pump probe spectroscopy”  
                         Supervisor: Prof. Dr. Heinrich Graener

2003-2005        Masters of Science in Physics  
                         Indian Institute of Technology, Bombay, India  
                         M.Sc. Thesis: “Surface enhanced Raman spectroscopy on biomolecules using silver nanoparticles and manganese titanate nanoparticles films”  
                         Supervisor: Prof. Dr. Tapanendu Kundu

2000-2003        Bachelors of Science in Physics  
                         University of Delhi, India  
                         B.Sc. Project: “Designing of circuits using IC-741 and 555 timer”  
                         Supervisor: Prof. Punkaj Narang

## Conference proceedings and Workshops

1. Sumedha Chouthe, Chris Sturm, Gerhard Seifert, Rüdiger Schmidt-Grund, Marius Grundmann, and Heinrich Graener, “*Femtosecond pump probe spectroscopy of ZnO thin films*”, Deutsche Physikalische Gesellschaft (DPG) spring meeting – Dresden, Germany, Paper HL 50.1 (2009).
2. Sumedha Chouthe, Snigdhatanu Acharya, Chris Sturm, Gerhard Seifert, Rüdiger Schmidt-Grund, Marius Grundmann, and Heinrich Graener, “*Charge carrier dynamics of ZnO and ZnO-BaTiO<sub>3</sub> thin films*”, International conference on optics of excitons and confined systems (OESC) – Madrid, Spain, submitted (2009).
3. Sumedha Chouthe, Chris Sturm, Gerhard Seifert, Rüdiger Schmidt-Grund, Marius Grundmann, and Heinrich Graener, “*Femtosecond pump probe spectroscopy of ZnO thin films*”, IMPRS workshop on advances in science and technology of nanostructures – Halle, Germany (2008).
4. Sumedha Chouthe, Chris Sturm, Gerhard Seifert, Rüdiger Schmidt-Grund, Marius Grundmann, and Heinrich Graener, “*Femtosecond pump probe spectroscopy of ZnO thin films*”, Sonderforschungsbereich (SFB 762) meetings – Halle and Wittenberg, Germany (2007, 2008, 2009).





# References

---

## Chapter 1.

- 1 Zhong Lin Wang, “Zinc oxide nanostructures: Growth properties and applications”, *Journal of Physics: Condensed matter*, Vol. 16, R829-R858 (2004).
- 2 Chennupati Jagadish, Stephen J. Pearton, “Zinc Oxide Bulk, Thin Films and Nanostructures”, Elsevier, ISBN 13: 978-0-08-044722-3 (2006).
- 3 Claus Klingshirn, Robert Hauschild, Johannes Fallert, Heinz Kalt, “Room temperature stimulated emission of ZnO: Alternatives to excitonic lasing”, *Physical Review B* 75, 115203 (2007).
- 4 Yefan Chen, N. T. Tuan, Yusaburo Segawa, Hang-ju Ko, Soon-ku Hong, Takafumi Yao, “Stimulated emission and optical gain in ZnO epilayers grown by plasma-assisted molecular-beam epitaxy with buffers”, *Applied Physics Letters*, Vol. 78, 11 (2001).
- 5 H. Cao, Y. G. Zhao, H. C. Ong, S. T. Ho, J. Y. Dai, J. Y. Wu, R. P. H. Chang, “Ultraviolet lasing in resonators formed by scattering in semiconductor polycrystalline films”, *Applied Physics Letters*, Vol. 73, 25 (1998).
- 6 Eun-Cheol Lee, K. J. Chang, “P-type doping with group-I elements and hydrogenation effect in ZnO”, *Physica B*, 376-377, 707-710 (2006).
- 7 M. G. Wardle, J. P. Goss, P. R. Briddon, “Theory of Li in ZnO: A limitation for Li based p-type doping”, *Physical Review B* 71, 155205 (2005).
- 8 Nohbert H. Nickel, Evgenii Terukov, “Zinc oxide – A material for micro- and optoelectronic applications”, Springer, ISBN-10 1-4020-3474-1 (2005).
- 9 J. Takeda, K. Takagi, T. Okabe, H. J. Ko and T. Yao, “Relaxation and diffusion of photoexcited carriers in ZnO epitaxial thin films”, *Phys. Stat. Sol. (c)* 1, No.4, 678-681 (2004).
- 10 Nobuyuki Arai, Jun Takeda, Hang-Ju Ko, Takafumi Yao, “Dynamics of high-density excitons and electron-hole plasma in ZnO epitaxial thin films”, *Journal of Luminescence*, 119-120, 346-649 (2006).
- 11 Jun Takeda, Nobuyuki Arai, Yuki Toshine, Hang-Ju Ko, Takafumi Yao, “Ultrafast dynamics of exciton-exciton and exciton-longitudinal optical-phonon scattering processes in ZnO epitaxial thin films”, *Japanese Journal of Applied Physics*, Vol. 45, No. 9A, 6961-6963 (2006).
- 12 J. Takeda, H. Jinnouchi, S. Kurita, Y. F. Chen, T. Yao, “Dynamics of photoexcited high density carriers in ZnO epitaxial thin films”, *Phys. Stat. Sol. (b)*, Vol. 229, No. 2, 877-880 (2002).

---

13 Y. C. Liu, S. K. Tung, J. H. Hsieh, “*Influence of annealing on optical properties and surface structure of ZnO thin films*”, *Journal of Crystal Growth* 287, 105-111 (2006).

14 Claus Klingshirn, Marius Grundmann, Axel Haffmann, Bruno Meyer, Andreas Waag, “*Zinkoxid – ein alter, neuer Halbleiter*”, *Physik Journal*, Vol. 5, No.1, 33-39 (2006).

15 Christophe Bauer, Gerit Baschloo, Emad Mukhtar, Anders Hagfeldt, “*Ultrafast relaxation dynamics of charge carriers relaxation in ZnO nanocrystalline thin films*”, *Chemical Physical Letters*, Vol. 387, 176-181 (2004).

16 Fanxin Wu, Jin Z. Zhang, “*Charge carrier dynamics of nanomaterials*”, *Dekker Encyclopaedia of Nanoscience and Nanotechnology*, Marcel Dekker, DOI 10.1081/E-ENN 120021414, 667-682 (2004).

## Chapter 2.

1 Claude Rulliere, “*Femtosecond laser pulses*”, Springer, ISBN 0-387-01769-0 (2003).

2 Wolfgang Demtroder, “*Laser spectroscopy Vol. 1: Basic principles*”, Springer, ISBN 978-3-540-73415-4 (2008).

3 Sterling Backus, Charles G. Durfee III, Margaret M. Murnane, Henry K. Kapteyn, “*High power ultrafast lasers*”, *Review of Scientific Instruments*, Vol. 69, 3 (1998).

4 Jean-Claude Diels, Wolfgang Rudolph, “*Ultrashort laser pulse phenomena*”, Academic press, ISBN 0-12-215492-4 (1996).

5 Rudiger Paschotta, “*Laser sources for ultrashort pulses*”, Tutorial, WILEY-VCH Verlag GmbH & Co. KGaA, Weinheim, www.laser-journal.de LTJ (2007).

6 H. Kuzmany, “*Solid-state spectroscopy*”, Springer (1998).

7 Yehuda B. Band, “*Light and matter*”, John Wiley & Sons, Ltd., ISBN-13: 978-0-471-89931-0 (PB) (2007).

8 A. M. Zheltikov, “*Let there be white light: Supercontinuum generation by ultrafast laser pulses*”, *Physics-Uspekhi* 49 (6) 605-628 (2006).

9 Ke Wang, Liejia Qian, Hang Luo, Peng Yuan, Heyuan Zhu, “*Ultrabroad supercontinuum generation by femtosecond dual-wavelength pumping in sapphire*”, *Optics Express* 6366, Vol.14, 13 (2006).

10 Jae Hun Kim, Meng-Ku Chen, Chia-En Yang, Jon Lee, Stuart Yin, Paul Ruffin, Eugene Edwards, Christina Brantley, Claire Luo, “*Broadband IR supercontinuum generation using single crystal sapphire fibers*”, *Optics Express* 4085, Vol.16, 6 (2008).

11 Stuart Shizhuo Yin, JaeHun Kim, Chun Zhan, JunWon An, Jon Lee, Paul Ruffin, Eugene Edwards, Christina Brantley and Claire Luo, “*Supercontinuum generation*

---

*in single crystal sapphire fibers*”, Optics Communication, Vol. 281, 1113-1117 (2007).

12 Robert. R. Alfano, “*The Supercontinuum Laser Source*”, Springer-Verlag, ISBN 0-387-96946-2 (1989).

13 Orazio Svelto, David C. Hanna, “*Principles of lasers*”, Plenum Press, ISBN-0-306-45748-2 (1998).

14 William T. Silfvast, “*Laser fundamentals*”, Cambridge University Press, ISBN-0-52183345-0 (2004).

15 G. Seifert, A. Podlipensky, J. Lange, H. Hofmeister, H. Graener, “*Ultrafast deformation dynamics of silver nanoparticles in glass induced by femtosecond laser pulses*”, Proceedings of SPIE, Vol. 6118, 244-253 (2006).

16 Anthony E. Siegman, “*Lasers*”, University Science Books, ISBN-0-935702-11-3 (1986).

17 Alexander Apolonskiy, “*Femtosecond Ti:Sapphire laser*”, LMU München.

18 M. Aoyama, T. Harimoto, J. Ma, Y. Akahane and K. Yamakawa, “*Second - harmonic generation of ultra-high intensity femtosecond pulses with a KDP crystal*”, Optics Express 579, Vol.9, 11 (2001).

19 Nicolaas Bloembergen, “*Nonlinear optics*”, Addison Wesley Publishing Company Inc., ISBN-0-201-57868-9 (1992).

20 S. A. Kovalenko, A. L. Dobryakov, J. Ruthmann, N. P. Ernsting, “*Femtosecond spectroscopy of condensed phases with chirped supercontinuum probing*”, Physical Review A, Vol. 59, 3 (1999).

21 Harland G. Tompkins, “*A users guide to ellipsometry*”, Academic Press, Inc., ISBN 0-12-693950-0 (1993).

22 Harland G. Tompkins, William A. McGahan, “*Spectroscopic ellipsometry and reflectometry*”, John Wiley & Sons Inc., PACS (1999).

23 R. M. A. Azzam, N. M. Bashara, “*Ellipsometry and polarized light*”, North Holland ISBN 0-444-87016-4 (1992).

24 Mathias Schubert, “*Infrared ellipsometry on semiconductor layer structures*”, Springer, PAC 71.36.+c, 78.20.-e, 78.20.Ls (2004).

### **Chapter 3.**

1 Yehuda B. Band, “*Light and matter*”, John Wiley & Sons, Ltd., ISBN-13: 978-0-471-89931-0 (PB) (2007).

2 X. W. Sun, H. S. Kwok, “*Optical properties of epitaxially grown zinc oxide films on sapphire by pulsed laser deposition*”, Journal of Applied Physics, Vol. 86, No.1, 408-411 (1999).

---

3 J. M. Martinez-Duart, R. J. Martin-Palma, F. Agullo-Rueda, “*Nanotechnology for Microelectronics & Optoelectronics*”, Elsevier, ISBN-13 978-0080-445533 (2006).

4 Mark Fox, “*Optical properties of Solids*”, Oxford University Press, ISBN 0-19-850613-9 (2001).

5 John Singleton, “*Band theory and electronic properties of solids*”, Oxford University Press, ISBN 0-19-850644-9 (2001).

6 R. J. Elliott, “*Intensity of optical absorption by excitons*”, Physical Review, Vol. 108, No. 6 (1957).

7 Nobuyuki Arai, Jun Takeda, Hang-Ju Ko, Takafumi Yao, “*Dynamics of high-density excitons and electron-hole plasma in ZnO epitaxial thin films*”, Journal of Luminescence, 119-120, 346-649 (2006).

8 Yin-Chieh Huang, Gia-Wei Chern, Kung-Hsuan Lin, Jiah-Chin Liang, Chi-Kuang Sun, Chia-Chen Hsu, Stacia Keller, Steven P. DenBaars, “*Femtosecond dynamics of exciton bleaching in bulk GaN at room temperature*”, Applied Physics Letters, Vol. 81, No. 1 (2002).

9 H. Frenzel, H. v. Wenckstern, A. Weber, H. Schmidt, G. Biehne, H. Hochmuth, M. Lorenz, M. Grundmann, “*Photocurrent spectroscopy of deep levels in ZnO thin films*”, Physical Review B 76, 035214 (2007).

10 Chennupati Jagadish, Stephen J. Pearton, “*Zinc Oxide Bulk, Thin Films and Nanostructures*”, Elsevier, ISBN 13: 978-0-08-044722-3 (2006).

11 Hisashi Yoshikawa, Sadao Adachi, “*Optical constants of ZnO*”, Jpn. J. Appl. Phys., Vol. 36, 6237-6243 (1997).

12 Claus Klingshirn, Marius Grundmann, Axel Haffmann, Bruno Meyer, Andreas Waag, “*Zinkoxid – ein alter, neuer Halbleiter*”, Physik Journal, Vol. 5, No.1, 33-39 (2006).

13 B. K. Meyer, H. Alves, D. M. Hofmann, W. Kriegseis, D. Forster, F. Bertram, J. Christen, A. Hoffmann, M. Starßburg, M. Dworzak, U. Haboek, A. V. Rodina, “*Bound exciton and donor-acceptor pair recombinations in ZnO*”, Phys. Stat. Sol. (b), Vol. 241, No. 2, 231-260 (2004).

14 T. Frank, G. Pensl, R. Tena-Zaera, J. Zuniga-Perez, C. Martinez Tomas, V. Munoz-Sanjose, T. Ohshima, H. Itoh, D. M. Hofmann, D. Pfisterer, J. Sann, B. K. Meyer, , “*Energetically deep defect centres in vapour phase grown zinc oxide*”, Applied Physics A, Vol. 88, 141-145 (2007).

15 A. F. Kohan, G. Ceder, D. Morgan, C. G. Van de Walle, “*First principles study of native point defects in ZnO*”, Physical Review B, Vol. 61, No. 22, 15019 (2000).

16 Anderson Janotti, Chris G. Van de Walle, “*New insights into the role of native*

- 
- point defects in ZnO*", Journal of Crystal Growth, Vol. 287, 58-65 (2006).
- 17 Anderson Janotti, Chris G. Van de Walle, "*Oxygen vacancies in ZnO*", Applied Physics Letters, Vol. 87, 122102 (2005).
- 18 C. G. Van de Walle, "*Hydrogen as a cause of doping in zinc oxide*", Physical Review Letters, Vol. 85, No. 5, 1012 (2000).
- 19 S. Christoulakis, M. Sucheck, M. Katharakis, N. Katsarakis, E. Koudoumas, G. Kiriakidis, "*ZnO nanostructured transparent thin films by PLD*" Rev. Adv. Mater. Sci, 10, 331-334 (2005).
- 20 M. Lorenz, G. Wagner, A. Rahm, H. Schmidt, H. Hochmuth, H. Schmid, W. Mader, M. Brandt, H. von Wenckstern, M. Grundmann, "*Homoepitaxial ZnO thin films by PLD: Structural properties*", Phys. Stat. sol. (c) 5, No.10, 3280-3287 (2008).
- 21 D. M. Hofmann, D. Pfisterer, J. Sann, B. K. Meyer, R. Tena-Zaera, V. Munoz-Sanjose, T. Frank, G. Pensl, "*Properties of the oxygen vacancy in ZnO*", Applied Physics A, Vol. 88, 147-151 (2007).
- 22 J. C. Simpson, J. F. Cordaro, "*Characterization of deep levels in zinc oxide*", Journal of Applied Physics, Vol. 63, 1781-1783 (1987).
- 23 Charles C. Kim, J. M. Garland, H. Abad, P. M. Raccach, "*Modelling the optical dielectric function of semiconductors: Extension of the critical-point parabolic-band approximation*", Physical Review B, Vol. 45, No. 20 (1992).
- 24 R. Schmidt-Grund, N. Ashkenov, M. M. Schubert, W. Czakai, D. Faltermeier, G. Benndorf, H. Hochmuth, M. Lorenz, M. Grundmann, "*Temperature dependence of the refractive index and the optical transitions at the fundamental band-gap of ZnO*", CP893, Physics of Semiconductors, 28<sup>th</sup> International conference, PACS 78.66.Hf; 77.22.Ch; 71.35; 72.10.Di (2007).
- 25 Wolfgang Demtroder, "*Laser spectroscopy Vol. 1: Basic principles*", Springer, ISBN 978-3-540-73415-4 (2008).
- 26 V. D. Lakhno, "*Continuum exciton in semiconductors*", Physical Review B, Vol. 46, No. 12 (1992).
- 27 H. Haug, S. W. Koch, "*Quantum theory of the optical and electronic properties of semiconductors*", World Scientific, ISBN 981-238-609-2 (2007).
- 28 F. Graham Smith, Terry A. King, "*Optics and photonics: An introduction*". John Wiley & Sons Ltd., ISBN 0-471-48924-7 (2000).
- 29 Max Born, "*Optik*", Springer-Verlag, ISBN 3-540-05954-7 (1985).
- 30 David N. Nikogosyan, "*Properties of optical and laser related materials*", John Wiley & Sons, ISBN 047197384X (1998).

---

31 Chengbin Li, Donghai Feng, Tianqing Jia, Haiyi Sun, Xiaoxi Li, Shizhen Xu, Xiaofeng Wang and Zhizhan Xu, “*Ultrafast dynamics in ZnO thin films irradiated by femtosecond lasers*”, Solid State Communications, Vol. 136, No. 7, 389-394 (2005).

## Chapter 4.

1 Wolfgang Demtroder, “*Laser spectroscopy Vol. 2: Experimental techniques*”, Springer, ISBN 978-3-540-74952-3 (2008).

2 O. Svelto, S. De Silvestri, G. Denardo, “*Ultrafast processes in spectroscopy*”, Plenum Press, ISBN 0-306-45481-5 (1996).

3 Jorge J. Morè, “*Lecture notes in mathematics*”, Springer, ISBN 978-3-540-08538-6 (2006).

## Chapter 5.

1 Jagdeep Shah, “*Ultrafast spectroscopy of semiconductors and semiconductor nanostructures*”, Springer, ISBN 3-540-64226-9 (1999).

2 Fanxin Wu, Jin Z. Zhang, “*Charge carrier dynamics of nanomaterials*”, Dekker encyclopaedia of nanoscience and nanotechnology, Marcel Dekker, DOI 10.1081/E-ENN 120021414, 667-682 (2004).

3 D. M. Hofmann, D. Pfisterer, J. Sann, B. K. Meyer, R. Tena-Zaera, V. Munoz-SanJose, T. Frank, G. Pensl, “*Properties of the oxygen vacancy in ZnO*”, Applied Physics A, Vol. 88, 147-151 (2007).

4 Chennupati Jagadish, Stephen J. Pearton, “*Zinc Oxide Bulk, Thin Films and Nanostructures*”, Elsevier, ISBN 13: 978-0-08-044722-3 (2006).

5 Christophe Bauer, Gerit Baschloo, Emad Mukhtar, Anders Hagfeldt, “*Ultrafast relaxation dynamics of charge carriers relaxation in ZnO nanocrystalline thin films*”, Chemical Physical Letters, Vol. 387, 176-181 (2004).

6 B. K. Meyer, H. Alves, D. M. Hofmann, W. Kriegseis, D. Forster, F. Bertram, J. Christen, A. Hoffmann, M. Starßburg, M. Dworzak, U. Haboeck, A. V. Rodina, “*Bound exciton and donor-acceptor pair recombinations in ZnO*”, Phys. Stat. Sol. (b), Vol. 241, No. 2, 231-260 (2004).

7 Claus Klingshirn, Robert Hauschild, Johannes Fallert, Heinz Kalt, “*Room temperature stimulated emission of ZnO: Alternatives to excitonic lasing*”, Physical Review B 75, 115203 (2007).

8 Yefan Chen, N. T. Tuan, Yusaburo Segawa, Hang-ju Ko, Soon-ku Hong, Takafumi Yao, “*Stimulated emission and optical gain in ZnO epilayers grown by plasma-assisted molecular-beam epitaxy with buffers*”, Applied Physics Letters, Vol. 78, No.11 (2001).

- 
- 9 Y. Toshine, J. Takeda, H. J. Ko, T. Yao, “*Conversion of an electron-hole plasma into a high density excitonic state in ZnO epitaxial thin films*”, Phys. Stat. Sol. (c), Vol. 1, No. 4, 839-842 (2004).
- 10 J. Takeda, H. Jinnouchi, S. Kurita, Y. F. Chen, T. Yao, “*Dynamics of photoexcited high density carriers in ZnO epitaxial thin films*”, Phys. Stat. Sol. (b), Vol. 229, No. 2, 877-880 (2002).
- 11 Jun Takeda, Susumu Kurita, Yefan Chen, Takafumi Yao, “*Ultrafast dynamics in ZnO epitaxial thin films studied by optical Kerr gate luminescence spectroscopy*”, International Journal of Modern Physics B, Vol.15, Nos. 28, 29, 30, 3669-3672 (2001).
- 12 J. Takeda, K. Takagi, T. Okabe, H. J. Ko and T. Yao, “*Relaxation and diffusion of photoexcited carriers in ZnO epitaxial thin films*”, Phys. Stat. Sol. (c) 1, No. 4, 678-681 (2004).
- 13 Jun Takeda, Nobuyuki Arai, Yuki Toshine, Hang-Ju Ko, Takafumi Yao, “*Ultrafast dynamics of exciton-exciton and exciton-longitudinal optical-phonon scattering processes in ZnO epitaxial thin films*”, Japanese Journal of Applied Physics, Vol. 45, No. 9A, 6961-6963 (2006).
- 14 Nobuyuki Arai, Jun Takeda, Hang-Ju Ko, Takafumi Yao, “*Dynamics of high-density excitons and electron-hole plasma in ZnO epitaxial thin films*”, Journal of Luminescence, 119-120, 346-649 (2006).
- 15 R. A. Taylor, S. Hess, K. Kyhm, J. Smith, J. F. Ryan, G. P. Yablonskii, E. V. Lutsenko, V. N. Pavlovskii, M. Heuken, “*Stimulated emission and excitonic bleaching in GaN epilayers under high-density excitation*”, Phys. Stat. Sol. (b), Vol. 216, No. 465 (1999).
- 16 H. Cao, Y. G. Zhao, H. C. Ong, S. T. Ho, J. Y. Dai, J. Y. Wu, R. P. H.Chang, “*Ultraviolet lasing in resonators formed by scattering in semiconductor polycrystalline films*”, Applied Physics Letters, Vol. 73, No. 25 (1998).
- 17 M. Kawasaki, A. Ohtomo, I. Ohkubo, H. Koinuma, Z. K. Tang, P. Yu, G. K. L. Wong, B. P. Zhang and Y. Segawa, “*Excitonic ultraviolet laser emission at room temperature from naturally made cavity in ZnO nanocrystal thin films*”, Material Science and Engineering, B56, 239-245 (1998).
- 18 P. Zu, Z. K. Tang, G. K. L. Wong, M. Kawasaki, A. Ohtomo, H. Koinuma, Y. Segawa, “*Ultraviolet spontaneous and stimulated emissions from ZnO microcrystallite thin films at room temperature*”, Solid State Communication, Vol. 103, 459-463 (1997).
- 19 A. Ohtomo, M. Kawasaki, Y. Sakurai, Y. Yoshida, H. Koinuma, P. Yu, Z. K. Tang, G. K. L. Wong, Y. Segawa, “*Room temperature ultraviolet laser emission from ZnO nanocrystal thin films grown by laser MBE*”, Material Science and Engineering, B54, 24-28 (1998).